

# 博 士 論 文

Study on dynamics of black aurora based on simultaneous  
optical and particle observations by REIMEI satellite

(れいめい衛星による光学・粒子同時観測に基づくブラックオーロラの研究)

小 淵 保 幸

平成 19 年



# Acknowledgements

I am deeply grateful to my supervisor, Professor Shoichi Okano, for introducing and suggesting this research subject, and for his ceaseless encouragement for me during my student life. I would like to express my deep gratitude to Dr. Takeshi Sakanoi for his careful advice and help in the study and his partnership on the development of MAC and Reimei observations of aurora. I would like to thank Profs. Takayuki Ono and Yasumasa Kasaba, and Drs. Hiroaki Misawa, Masahide Iizima, Isao Murata, and Yukihiro Takahashi for their helpful suggestions and encouragement at the joint seminar of Space Physics Group.

I am grateful to Prof. Masafumi Hirahara of University of Tokyo, Drs. Kazushi Asamura and Atsushi Yamazaki of JAXA/ISAS, and Dr. Masaki Okada of NIPR for their kind supports and help at the development of MAC, and their valuable suggestions and encouragement. I also express my sincere gratitude to Prof. Hirobumi Saito and Drs. Takahide Mizuno, Shin-ichiro Sakai, Seisuke Fukuda, Yosuke Fukushima of JAXA/ISAS and the other members of Reimei engineering team for their strong assistance in development and operation of Reimei satellite.

I express my deep appreciation to Drs. Yusuke Ebihara and Kanako Seki of Solar-Terrestrial Environment Laboratory, Nagoya University for their permission of using particle data analysis tools and helpful suggestions for this work. I wish to thank Dr. Yoshizumi Miyoshi of Solar-Terrestrial Environment Laboratory, Nagoya University for his helpful discussion on various aspects in physics and his encouragement for this work. I also wish to thank Dr. Yuto Kato for his helpful advice and discussion for this work.

I would like to thank Mr. Norihide Takeyama, Mr. Yoshikazu Kanai and the other members of Genesia Corporation for their great job in the development of optics of MAC and their helpful and important support and encouragement for my student life.

Special thanks are to all members in our laboratory, Planetary Plasma and Atmospheric Research Center of Tohoku University, for their support to my study and student life.

Finally, I would like to express my deep gratitude to my family for their continuous support and encouragement during my student life.

# Abstract

In 1970's, fine scale dark structures were found in diffuse aurora by ground-based optical observation, and named as black aurora [Royrvik, 1976; Davis, 1978]. Since then, various types of black aurora, such as black arc, black patch, and black vortex, have been reported [e.g. Kimball and Hallinan, 1998; Trondsen and Cogger, 1997]. However, their generation mechanism is still unknown in present days.

In order to investigate fine scale structures of aurora, a scientific satellite Reimei, which was launched into a ~640km altitude 0050-1250 LT polar orbit from Baikonur Space Center in Kazakhstan in August 2005, has been carrying out aurora observations. Multi-spectral Auroral Camera (MAC) on board the Reimei satellite has been developed in Tohoku University. MAC is a three-channel monochromatic CCD imager, and its specifications are summarized below; (i) the optical system consists of refracting optics; (ii) the three wavelengths of MAC was chosen so that it can observe  $N_2^+$  1NG (427.8 nm), O green line (557.7 nm), and  $N_2$  1PG (670 nm); (iii) field-of-view of MAC is 7.6 degrees; (iv) spatial and temporal resolutions are about 1.2 km, 120 msec, respectively, in typical observation mode pointing its field of view to a magnetic footprint. During the development stage of MAC, a variety of special measures were necessary to achieve satisfactory operation of MAC. Such special measures in MAC development are summarized below; (i) development of thermal paths for cooling CCD and some elements on the power control board of MAC; (ii) adjustment of lens focus; (iii) vibration and shock tests simulating the launch condition; (iv) radiation test for checking durability of CCD and the interference filters for radiation; (v) sensitivity calibration. As a result of these measures in the development stage, it was confirmed that MAC had enough performance for observation of aurora with high temporal and spatial resolutions.

Since its successful launch, Reimei has been carrying out aurora observation. Optical observations of black arc and black patch were successfully made with MAC for 23 events in a period from November 1st, 2005 through October 30th, 2006. Among them, simultaneous optical imaging and precipitation particle observations were made for 13 events, of which nine

events are black arc events, and other four events are black patch events. Nineteen events out of all 23 events were observed in the northern hemisphere, and the others were observed in the southern hemisphere. Based on the analysis of these black aurora events, characteristics and possible generation mechanism of black aurora are summarized as follows.

- 1) Emission intensities of black arc and black patch are rather faint in the order of 2 ~ 4 kR. The intensities are not different between the northern hemisphere and the southern hemisphere. The width of black arc is in a range of 3 ~ 10 km. The scale of black patch is about 3 ~ 5 km. The width is not different between the northern and the southern hemisphere, too.
- 2) Black arc and black patch appear favorably in the invariant latitude range of 66 - 68 degrees. On the other hand, black arc and black patch appear also in the invariant latitudes greater than 70 degrees. This fact has not been reported in past studies. This may be because coverage area of our observation is quite large compared to the past observations.
- 3) Regarding a relation between magnetic activity and the appearance of black arc and black patch, 11 events out of 19 events (the northern hemisphere events) were observed in magnetic quiet periods. Other events were observed in a variety of conditions.
- 4) Behaviors of precipitating electrons and ions that correspond to all black arc or black patch events obtained by Reimei showed that their characteristics are those coming from the central plasma sheet. Precipitating electron flux with energies greater than 2 ~ 7 keV is deficient at the time when a magnetic footprint of the satellite passed over a black arc or black patch.
- 5) An inverted-V structure with a peak energy of 2 ~ 5 keV associated with black aurora is often seen in the downward electron E-T diagram. Such inverted-V structures overlap electron precipitations contributing to diffuse aurora. Six events out of 13 black arc or black patch events are associated with such inverted-V structures. Because of their weak peak energy, precipitations accelerated by inverted-V structure do not seem to contribute strongly to aurora emissions in the image data obtained by MAC.

- 6) Pulsating aurora was often associated with black arc and black patch, and it appears in the equatorward of black aurora. In pulsating aurora, apparent energy-dispersions are seen in precipitating electron flux. On the other hand, electron flux for black arc does not show any energy-dispersion.
  
- 7) Precipitating electron flux with energies greater than 2 ~ 7 keV for black arc and black patch is deficient compared to that for surrounding diffuse aurora. On the other hand, the electron flux with energies less than that for black patch is almost same to that for surrounding diffuse aurora. This fact suggests that the deficiency of electron flux with energies greater than 2 ~ 7 keV is not caused by any electric field such as the divergent electric field. Based on our observation results, it is strongly suggested that the pitch angle diffusion by upper band whistler mode waves is suppressed in a source region of black aurora while diffuse aurora surrounding the black aurora is produced by precipitating electrons that was caused by pitch angle scattering due to upper band whistler mode waves and/or electrostatic Electron Cyclotron Harmonic waves in the plasma sheet. Accordingly, our results of Reimei observations for black aurora suggest that hot electron (few keV) density is low in the source region of black aurora.
  
- 8) Drifting speed for two events of drifting black patches were derived using 2D correlation analysis. The drift speed of a black patch on January 27, 2006 was about 5.7 km/sec, and that on October 1, 2006 was about 3.3 km/sec. Because of existence of concurrent inverted-V structure,  $E \times B$  force is expected for drifting electrons in a source region where these black patches were produced. Electric fields, which cause such  $E \times B$  drift, were estimated from drift speeds derived by using 2D correlation analysis of image data. Estimated electric field is in close agreement with an electric field calculated from inverted-V structure for the event on January 27, 2006. For the case of the event on October 1, 2006, electric field estimated from drift velocity of black patch does not agree so well with an electric field calculated from inverted-V structure as the event on January 27, 2006. However, the order of the electric field calculated from drift velocity agrees with the order of an electric field calculated from Reimei particle data.





# Contents

## Acknowledgements

## Abstract

<b>1. Introduction</b>	<b>1</b>
1.1 Aurora phenomena	1
1.2 Auroral fine-scale structures	7
1.3 Black aurora	10
1.4 Purpose of this thesis	16
<b>2. Instrumentation</b>	<b>19</b>
2.1 Reimei satellite	19
2.2 Scientific instruments	23
2.2.1 Multi-spectral Auroral Camera (MAC)	23
2.2.2 Electron and Ion energy Spectrum Analyzer (ESA/ISA)	30
<b>3. Development of Multi-spectral Auroral Camera</b>	<b>33</b>
3.1 Thermal path for cooling CCD and components on the circuit board	33
3.2 Adjustment of lens focus	37
3.3 Environment tests	42
3.3.1 Vibration test	42
3.3.2 Shock test	43
3.3.3 Radiation test	44
3.4 Sensitivity calibration	46
<b>4. Observation and data analysis</b>	<b>49</b>
4.1 Methods of observation	49
4.1.1 Simultaneous image and particle observation	49
4.1.2 Arbitrary pointing observation	52
4.1.3 Tracking observation	54
4.2 Satellite Operation	56

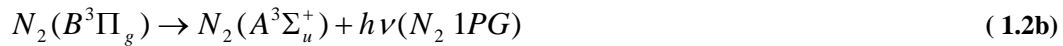
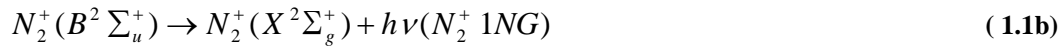
4.2.1	Observation planning	56
4.2.2	Operation method	58
4.3	Methods of data analysis	61
4.3.1	Image data process	61
4.3.2	2D correlation analysis	63
<b>5.</b>	<b>Results</b>	<b>67</b>
5.1	Event selection	67
5.2	Black arc and black patch events	70
5.2.1	Image and particle data; an example of black arc event	70
5.2.2	Statistical characteristics of black arc and black patch obtained by Reimei	79
5.3	Drifting black patch event	85
5.3.1	Image and particle data	85
5.3.2	2D correlation analysis	94
<b>6.</b>	<b>Discussion</b>	<b>97</b>
6.1	Possible mechanism for producing black arc and black patch	97
6.2	Possible mechanism for the origin of drifting black patch	101
<b>7.</b>	<b>Conclusions</b>	<b>107</b>
	<b>References</b>	<b>113</b>

# Chapter 1

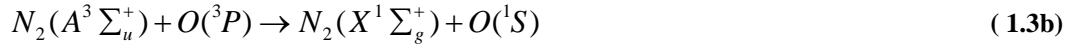
## Introduction

### 1.1 Aurora phenomena

It is well known that auroral dynamics are strongly coupled with magnetospheric and ionospheric phenomena. Therefore, aurora is a manifestation of complex sun-earth relationship that changes both ionosphere and magnetosphere. Neutral gases and ions in the earth's upper atmosphere, whose altitude distributions are shown in **Figure 1.1**, are excited by collisions with high-energy electrons and ions that precipitate along magnetic field lines from the magnetosphere, which is controlled by the sun. Besides collisions of high-energy electrons and ions with neutral particles, chemical processes such as dissociative recombination or energy exchange between excited ions and neutral atoms are also able to excite neutral particles. However, it is known that the primary excitation processes in aurora for producing prominent aurora emissions such as  $N_2^+ 1NG$  and  $N_2 1PG$  are thought to be collisions of precipitating electrons with neutral, and they are;



Here, (1.1a) is an excitation process of  $N_2^+$  1NG, and (1.2a) is an excitation process of  $N_2$  1PG. Both are prominent permitted lines in visible aurora. On the other hand, Oxygen green line (OI 557.7 nm), which is one of the most bright emission in aurora, is thought to be excited by following two processes;



Here, (1.3a) is a direct excitation process of Oxygen atoms by collision with high-energy electron, and (1.3b) is an excitation process by energy exchange with excited  $N_2$ . This energy exchange process is thought to be one of dominant processes for producing O green line aurora as well as the excitation process by direct collision with high-energy electrons [Gerdjikova and Shepherd, 1987]. The energy level of  $N_2$  in the left-hand side of (1.3b) is same to the energy level of  $N_2$  after emitting of  $N_2$  1PG (see **Figure 1.2**), and it is suggested that O green line emission is related to  $N_2$  1PG emission. However, the relationship between O green line and  $N_2$  1PG emissions in aurora and the dominant process for exciting auroral O green line is not clear yet.

Intensity and peak emission altitude of each auroral emission are affected by characteristics of precipitating particles and density distribution of atoms and molecules in the upper atmosphere. For example, as given in **Figure 1.3**, ionization rate and the peak altitudes of ionization are dependent on energy of precipitating electrons. Intensity distribution and its peak altitude of auroral emission are also dependent on energy of precipitating electrons because excitation cross section is a function of energy of precipitating electrons, and the lifetime of excited species has also to be taken into account for deactivation (quenching).

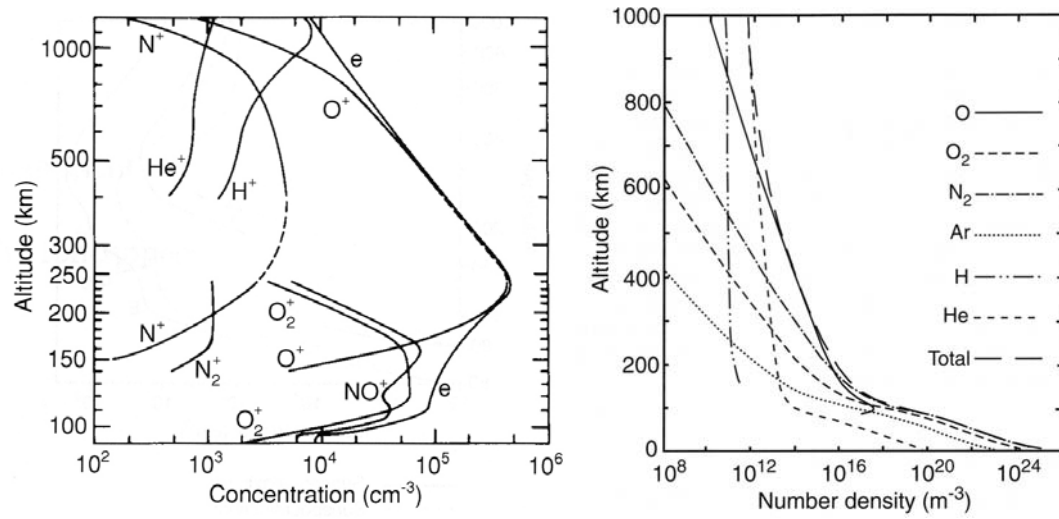


Figure 1.1 Altitude distribution of the ionospheric ions (left) and neutral gases (right) [Richmond, 1983; Johnson, 1966].

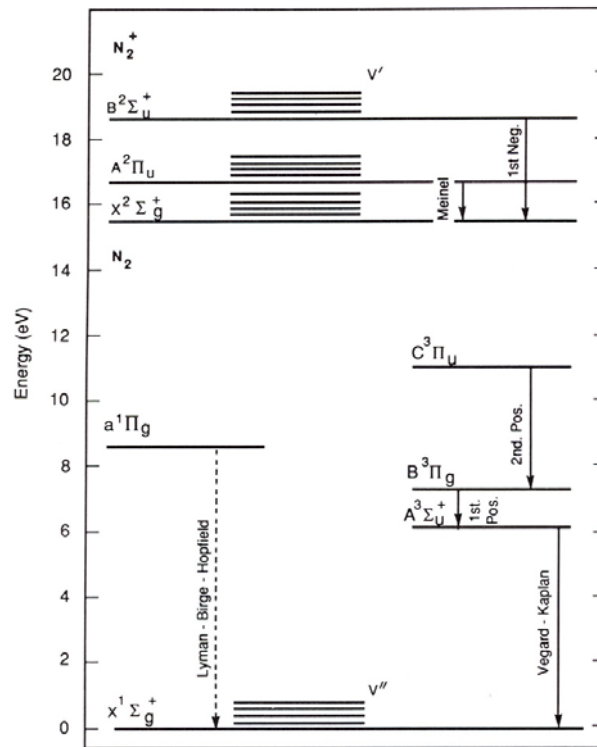
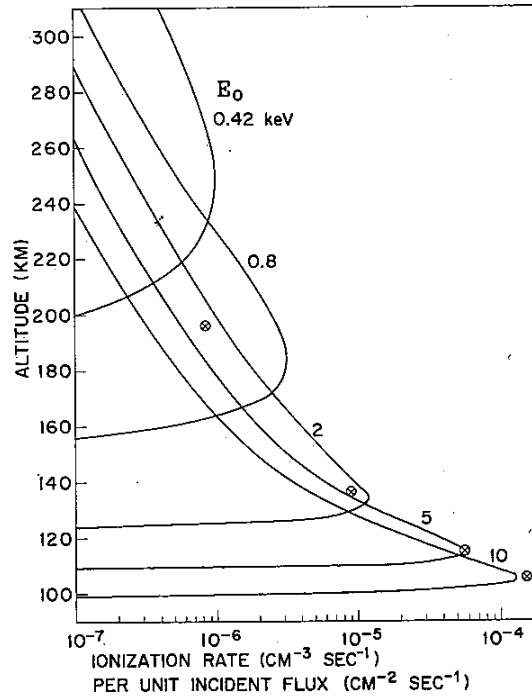


Figure 1.2 Energy level and transitions of N<sub>2</sub><sup>+</sup> and N<sub>2</sub> [Torr et al., 1992].



**Figure 1.3 Ionization rates per unit incident flux for Gaussian fluxes in the range 0.42 – 10 keV [Banks *et al.*, 1974].**

As mentioned above, aurora is affected by conditions in the ionosphere and magnetosphere, and changes its form and brightness dynamically with time and in space. It is well known that there are various kinds of auroral forms such as discrete arc, auroral curl, diffuse aurora, black aurora, pulsating aurora, and flickering aurora [e.g., *Beach et al.*, 1968; *Davis*, 1978; *Akasofu and Kan*, 1980; *Johnstone*, 1983]. Diffuse aurora appears equatorward of discrete arcs [*Kamide and Akasofu*, 1976]. Auroral curls are characterized by periodic structures in discrete arcs and they have spatial scales of 1-5 km [e.g., *Hallinan and Davis*, 1970; *Oguti*, 1978; *Vogt et al.*, 1999]. Auroral curls are sometimes called as auroral rays because of their vertical shape. Pulsating aurora is observed during the recovery phase of substorms. This auroral phenomenon exhibits typical period of a few seconds to a few tens of seconds, and  $\sim 3$  Hz modulations are often observed in the pulsation structures [e.g., *Royrvic and Davis*, 1977; *Sandahl et al.*, 1980]. Flickering aurora is characterized by vibrating column structures with periodic intensity variations in discrete arcs. The spatial scale of the width of flickering aurora is in the range of 1-12 km, and frequencies of the modulation are usually 3-15 Hz [e.g., *Beach et al.*, 1968; *Kunitake and Oguti*, 1984; *McFadden et al.*, 1987; *Sakanoi and Fukunishi*, 2004]. In terms of

precipitation for these aurora emissions, their production mechanisms have been investigated with immense interest by using ground-based and satellites/rocket observation data. In particular, the field-aligned acceleration processes and magnetosphere-ionospheric coupling have been examined with particle, magnetic and electric fields and plasma wave data obtained by various satellites, such as DE, S3-3, Akebono, Freja, and FAST [Hoffman and Schmerling, 1981; Cattell, 1982; Oya and Tsuruda, 1990; Lundin *et al.*, 1994; Sakanoi *et al.*, 1995; Carlson *et al.*, 1998]. The auroral electrons precipitating from the magnetosphere are accelerated by field-aligned quasi-electrostatic electric field (convergent electric field), called as inverted-V potential structure, and also by kinetic Alfvén waves (KAW) and inertial Alfvén waves (IAW) at altitudes of several thousands kilo-meters [e.g., Stasiewicz *et al.*, 2000; Schriver *et al.*, 2003]. Inverted-V potential structure is a typical field-aligned potential structure for the auroral particle acceleration, and the name is originated from inverted-V shape in energy-time diagram observed by various space aircrafts. Inverted-V potential structure is located at an altitude range of about 1000-10000 km, and its latitudinal width is in the range of several tens kilometers to several hundreds kilometers, usually 100 km [e.g., Lundin and Haerendel, 1995; Temerin, 1997]. Magnetospheric electrons with the energy of a few hundreds eV to 1 keV are accelerated by the inverted-V potential structure, and precipitate to the earth's upper-atmosphere. As reported by Frey *et al.* [1998], it is suggested that discrete aurora appears as a result of electron precipitation accelerated by the quasi-electrostatic field-aligned potential drop. However, much smaller filaments within an arc have been observed by ground-based observations, and their width is order of 100 m [e.g., Maggs and Davis, 1968; Borovsky and Suszcynsky, 1993]. Therefore, the relationship between the spatial scale of inverted-V potential structure and discrete arcs or filaments remains a question. Its detail will be described in Section 1.2. On the other hand, it has been reported that KAW and IAW are very important for auroral physics since they have the parallel electric field component, which can accelerate electrons aligned to the magnetic field [Stasiewicz *et al.*, 2000]. In recent study about relationship between these waves and aurora, it is suggested that these waves associate with the generation of fine-scale aurora, which includes flickering aurora [Sakanoi *et al.*, 2005].

Above mechanisms such as inverted-V potential structure and/or KAW and IAW are consistent with discrete arcs, auroral curls, and flickering auroras. The mechanism of precipitation for diffuse aurora and pulsating aurora, which appear in the equatorward boundary of auroral oval, is thought as pitch angle diffusion between hot electrons and waves in the magnetosphere [e.g., Kennel *et al.*, 1970; Davidson, 1990; Johnstone *et al.*, 1993; Demekhov

and Trakhtengerts, 1994; Horne *et al.*, 2003]. Diffuse aurora is a low-level light emission, and this fact shows that diffuse aurora is the result of  $\sim$ keV electron precipitation. Therefore, the mechanism of precipitation for above auroras is thought as pitch angle diffusion. Waves that cause precipitation of hot electrons have been identified as electrostatic electron cyclotron harmonic (ECH) waves and whistler mode waves. ECH waves are tightly confined to the magnetic equator [Gough *et al.*, 1979], and are associated with highly anisotropic pitch angle distributions [Wrenn *et al.*, 1979; Horne *et al.*, 1987]. ECH waves generally resonate with electrons of a few hundreds eV to a few keV causing pitch angle scattering and it has been shown that ECH waves can scatter electrons into the loss cone with strong diffusion rate [Lyons, 1974; Horne *et al.*, 2003]. On the other hand, it has been also suggested that ECH waves lack sufficient power to cause strong pitch angle diffusion from wave observations [Belmont *et al.*, 1983]. However, recent modeling work and event study have suggested that the distribution of waves mapped on the magnetosphere depends on MLT and the magnetic condition of magnetosphere [Chen and Schulz, 2001; Horne *et al.*, 2003]. Whistler mode waves are thought to resonate with relatively high-energy electrons, more than few keV, and these waves can resonate with electrons with the order of keV if the density of electrons is sufficiently high and wave frequency is sufficiently high below the electron gyrofrequency  $f_{ce}$  [Johnstone *et al.*, 1993]. The effect of pitch angle diffusion by propagating upper band (UB) and lower band (LB) whistler mode chorus waves are modeled by Inan *et al.* [1992]. The result of this model suggests that the high-energy electrons,  $\sim$ 10-50 keV, often related to pulsating aurora are diffused by the LB chorus waves, and low-energy electrons,  $\sim$ 1-10 keV, related to diffuse aurora, are diffused by UB chorus waves. On the other hand, Sato *et al.* [2004] suggested that the source region of pulsating aurora was located earthward and far from the equatorial plane, and that pulsating aurora appeared to be closely related to the inverted-V potential structure by using data obtained by FAST satellite. As mentioned above, the generation mechanism of pulsating aurora has not been identified clearly yet. In addition, remaining problems for pitch angle diffusion by these whistler mode waves are that relatively high temperature anisotropy is required to generate whistler mode waves and the calculations for pitch angle diffusion by whistler mode waves have not been performed to determine the efficiency of electron precipitations. Recently, it has also been shown that both of these waves are important for pitch angle diffusion during periods of auroral activity [Meredith *et al.*, 2000; Horne and Thorne, 2000]. As described above, the mechanism of precipitation for diffuse aurora and pulsating aurora is very complicated and has not yet understood perfectly. One of the reasons for this



problem is that these waves are very difficult to observe and no further work has been done, therefore, further observations and simulations are needed.

## 1.2 Auroral fine-scale structures

As described in the preceding section, aurora has various types of spatial and temporal scale. One of the most interesting phenomena is the auroral fine-scale structures. In this section, the details of auroral fine-scale structures are described. Ground-based measurement data in the past have shown that optical aurora has fine scale filaments down to a spatial scale of 100 m [Maggs and Davis, 1968; Hallinan and Davis, 1970; Borovsky, 1993]. Narrow discrete arcs and multiple arcs with the width of hundreds meters to several kilometers are often observed by ground-based optics, and are summarized in previous studies [e.g., McFadden *et al.*, 1990; Trondsen *et al.*, 1997; Hallinan *et al.*, 2001]. **Figure 1.4** shows an example of fine-scale arcs. On the other hand, satellite particle data have shown that the typical width of inverted-V structure is  $\sim 100$  km [Sakanoi *et al.*, 1995], while FAST data shows the existence of small-scale inverted-V with width of a few km [McFadden *et al.*, 1999]. These arcs have been investigated by simultaneous observation data between satellite data and ground-based optics, and a correspondence was found with small-scale inverted-V potential structure with a width of a few km [Stenbaek-Nielsen *et al.*, 1998; Hallinan *et al.*, 2001]. **Figure 1.5** shows an example of the result of the magnetic conjugate observation between FAST satellite and an aircraft [Stenbaek-Nielsen *et al.*, 1998]. Trondsen *et al.* [1997] suggested that multiple fine-scale arcs were generated by precipitations caused by IAW. So far, various observations of such fine-scale arcs have been carried out, however, the mechanism for the generation of fine-scale arcs has not been identified clearly, and spatial and temporal discrepancies between optical aurora arcs obtained from ground-based observation and precipitating electrons obtained from satellite and rocket observations have always hampered clarification of the production mechanism.

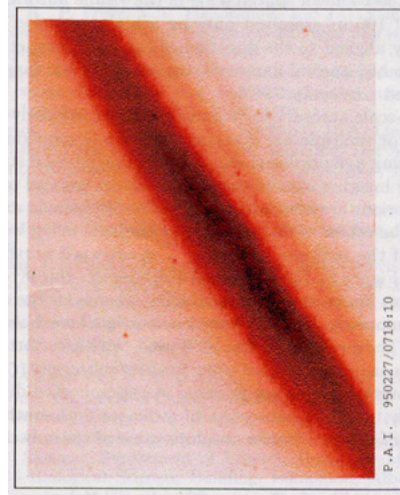


**Figure 1.4** An example of fine-scale multiple arcs [Trondsen *et al.*, 1997]. Three fine-scale arcs can be seen. The width of the most fine arc is about 370 m in this picture.

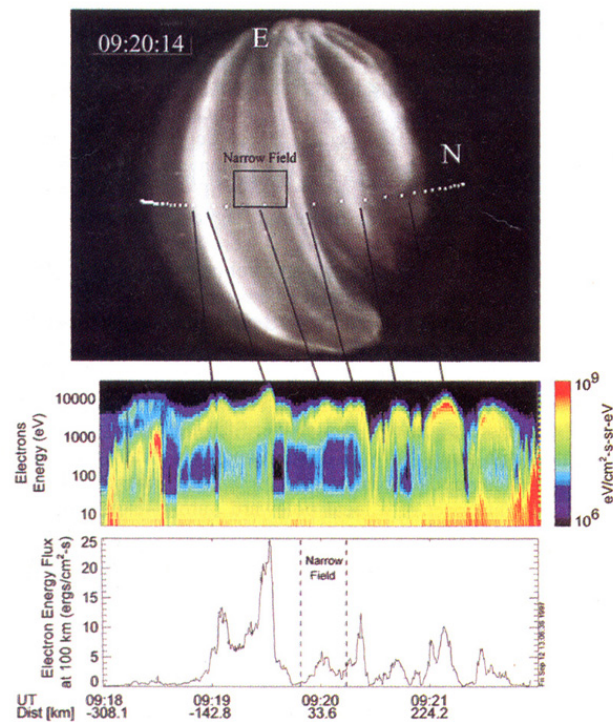


**Figure 1.5** An example of magnetic conjugate observation between FAST satellite and an aircraft [Stenbaek-Nielsen *et al.*, 1998]. The image (top panel) was obtained by an imager on board an aircraft, and an energy-time diagram was obtained by FAST. A white dotted line in the top panel denotes the orbital footprint of FAST.

There are various forms of fine-scale auroral structures, which include auroral curls and black aurora and flickering aurora, other than the fine-scale arcs and filaments. **Figure 1.6** shows examples of auroral curls [Trondsen and Cogger, 1998]. The auroral curls were first studied in depth by Hallinan and Davis [1970]. By intensive observations [e.g., Hallinan and Davis, 1970; Oguti, 1978; Trondsen and Cogger, 1998; Vogt *et al.*, 1999], parameters of auroral curls have been obtained as follows; the speed of curl system motion is 1-30 km/sec, the lifetime of curl system is 0.5-2 sec, the scale length of a curl is 300 m ~ 3 km. Past studies suggested that Alfvén waves may play a role for generation of the auroral curls [Wagner *et al.*, 1983; Vogt *et al.*, 1999; Hallinan *et al.*, 2001]. Flickering aurora was first well defined by Beach *et al.* [1968]. The periodic intensity variations with a frequency of about 10 Hz were observed by them. The parameters of flickering aurora have been obtained as follows; the spatial scale of flickering spot is a diameter of about 1-10 km, the length of flickering columns is about 40 km, their lifetime is 1-2 sec [Oguti, 1978; Kunitake and Oguti, 1984]. Flickering aurora is suggested to be produced by periodic modulations of precipitating electron flux, which include periodic field-aligned electron burst or modulated inverted-V electron precipitation [e.g., Spiger and Anderson, 1985; McFadden *et al.*, 1987]. Recently, based on ground-based optical observations and theoretical studies of dispersive Alfvén waves, flickering aurora is suggested to be produced by the modulations of electron flux by electromagnetic ion cyclotron wave or IAW in the auroral acceleration region [Sakanoi and Fukunishi, 2005]. Black auroras are fine-scale dark regions with a scale of less than 10 km in diffuse aurora. The details of black aurora will be described in the next section.

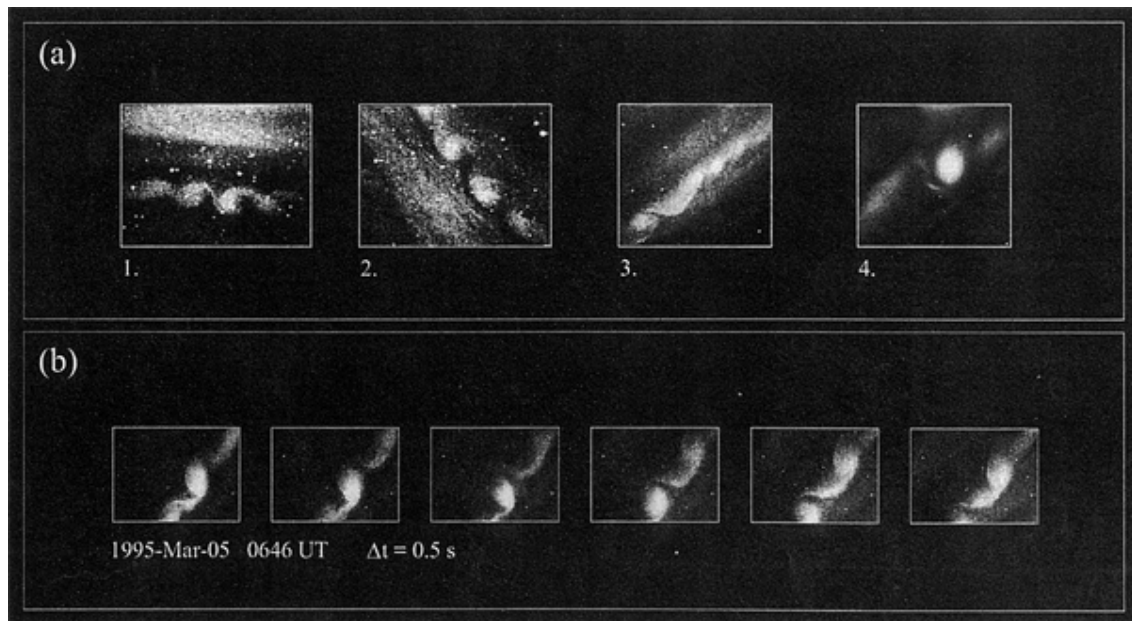


**Figure 1.6** Examples of auroral curls [Trondsen and Cogger, 1998]. Panel (a) shows four examples of curl system events, and panel (b) is the time evolution of a curl system.

### 1.3 Black aurora

Black aurora is defined as the dark regions within a uniform background emission, which is usually diffuse aurora [Royrvik, 1976; Davis, 1978]. Oguni [1975] observed and reported the formation of “dark holes” in midnight sector after auroral expansion by using an intensified TV camera. Royrvik [1976] observed eastward drifting “black spots”, “black arc segments”, and “black vortex structures” in the midnight sector by using a 20 degrees field of view intensified TV camera. Since these works, some results of black aurora observation have been reported [Trondsen and Cogger, 1997; Kimball and Hallinan, 1998a; Kimball and Hallinan, 1998b; Peticolas et al., 2002; Blixt and Kosch, 2004], and several kinds of black aurora were found; black vortex street (black curls), black arc, black patch (black ring). **Figure 1.7**, **Figure 1.8**, and **Figure 1.9** show examples of these black auroras. Black vortex streets (black curl) have a wavelength of 1-4 km, and the spatial scale of a black curl is in a range of 0.5-5.7 km [Trondsen and Cogger, 1997; Kimball and Hallinan, 1998b]. In addition, black vortex streets drift eastward or westward with a speed of 0.2-5 km/sec [Kimball and Hallinan, 1998b]. Each black curl has a clockwise rotational sense (opposite to that of auroral curls), and this is attributed to a

Kelvin-Helmholtz instability in a divergent electric field [Trondsen and Cogger, 1997; Kimball and Hallinan, 1998b]. The width of black arc is in a range of few hundreds meters to 10 kilometers [Trondsen and Cogger, 1997; Blixt and Kosch, 2004]. East-west aligned black arcs are often multiple arcs, and frequently found within the midnight sector diffuse aurora. It has also been reported that black arcs typically drift equatorward with a few hundreds m/sec [Trondsen and Cogger, 1997; Blixt and Kosch, 2004]. Black patches (black arc segments) are observed within the midnight sector [Trondsen and Cogger, 1997; Kimball and Hallinan, 1998a], too. They also reported that the spatial scale of black patches is in a range of few hundreds meters to 14 kilometers and black patches drift only eastward with a speed in a range of 0.2-3.4 km/sec. Westward drifting black patches have not observed and reported. Black rings have been reported only by Kimball and Hallinan [1998a]. This phenomenon was observed by using a narrow-field camera at the Ester Dome, and was reported to appear before local magnetic midnight drifting eastward. They also reported that the width of these black rings was about 2 km with average major and minor axes of  $9.6 \pm 0.8$  km and  $3.4 \pm 0.3$  km, respectively. As described above, black auroras have various forms and dynamics. However, mechanisms for their generation and motion have not been identified clearly. It is because that observation of black aurora is very difficult due to their small spatial scale and appearance characteristics (often appears within diffuse aurora), and observation reports of black aurora are limited.

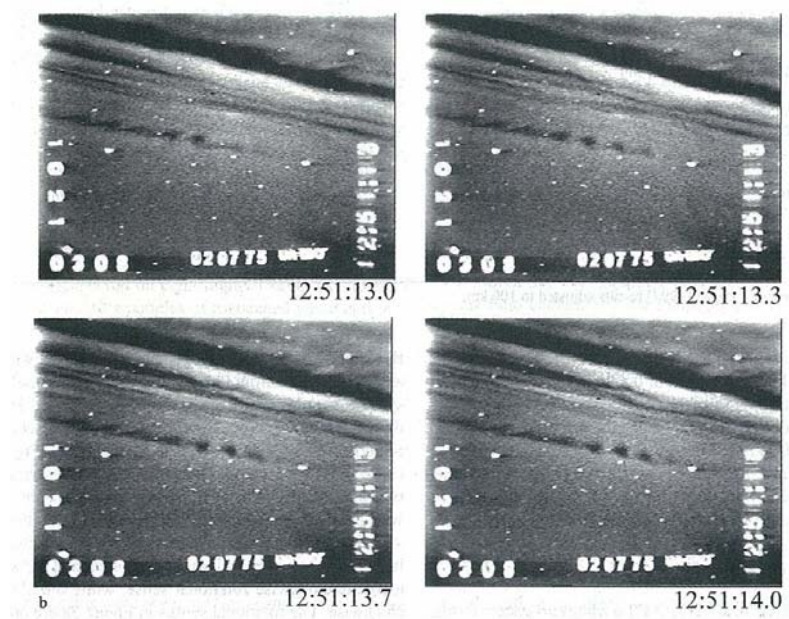


Figure 1.7 Examples of black vortex streets [Kimball and Hallinan, 1998b].

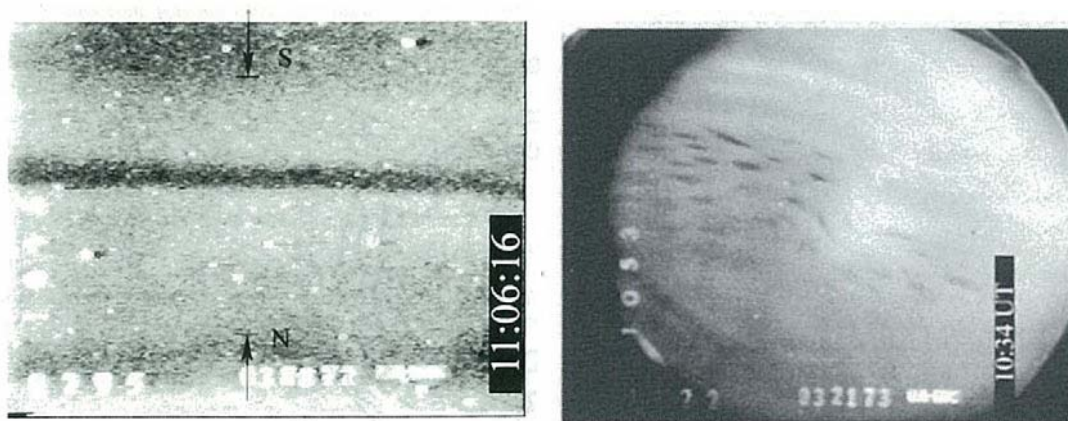


Figure 1.8 An example of black arc (left panel) and black patches (right panel) [Kimball and Hallinan, 1998a].



**Figure 1.9** An example of black rings [Kimball and Hallinan, 1998a].

As stated above, the mechanism for generation of black aurora has not been clearly identified. However, some ideas for generation mechanism of black aurora that take into account characteristics of black aurora using data obtained by satellites have been reported. A major idea among them is the divergent electric field. *Marklund et al.* [1994] have observed intense divergent electric field (1-2 V/m) with small scale, about 1 km, at lower altitudes (around 800 km) and suggested that the electric field would contribute for generation of black vortex streets. As mentioned earlier, black vortex streets have a clockwise rotational sense and the divergent electric field (positive space charge) is consistent with a Kelvin-Helmholtz vortex to produce black vortex streets. **Figure 1.10** shows schematic drawings of the vortex street and of the curl development due to charge sheet instability, and electric field data obtained by Freja. *Marklund et al.* [1994] suggested that the low-altitude divergent electric field is associated with a downward current region coupled with upward current regions which cause electron precipitation. **Figure 1.11** shows a schematic drawing for such configuration. However, observational supports for such relation between divergent electric fields and black auroras have never been reported so far, and it has not been clearly identified whether the divergent electric field associates with black aurora.



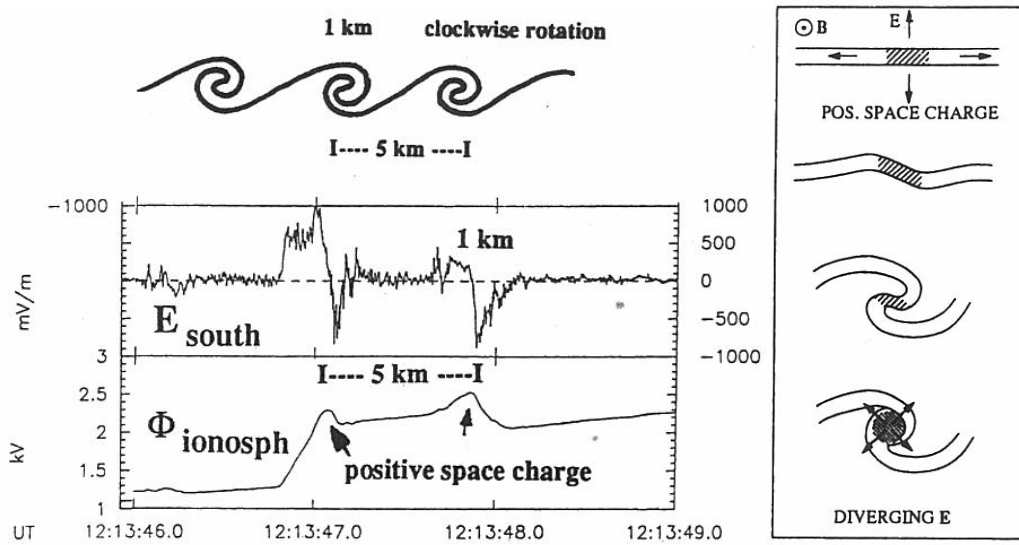


Figure 1.10 Schematic drawings of the vortex street and of the curl development due to charge sheet instability (top left and right panel), and electric field data obtained by Freja (bottom left panel) [Marklund *et al.*, 1997].

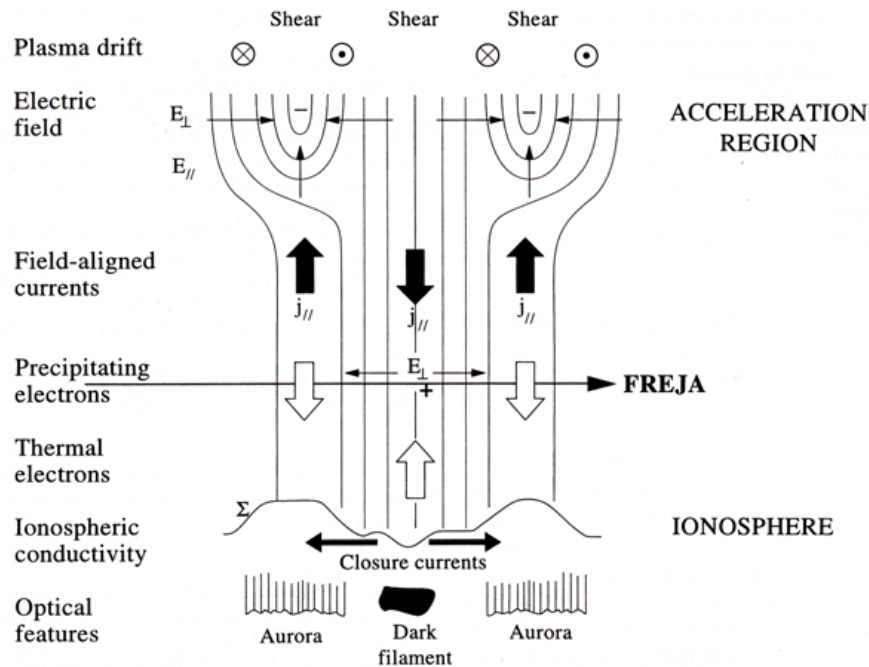
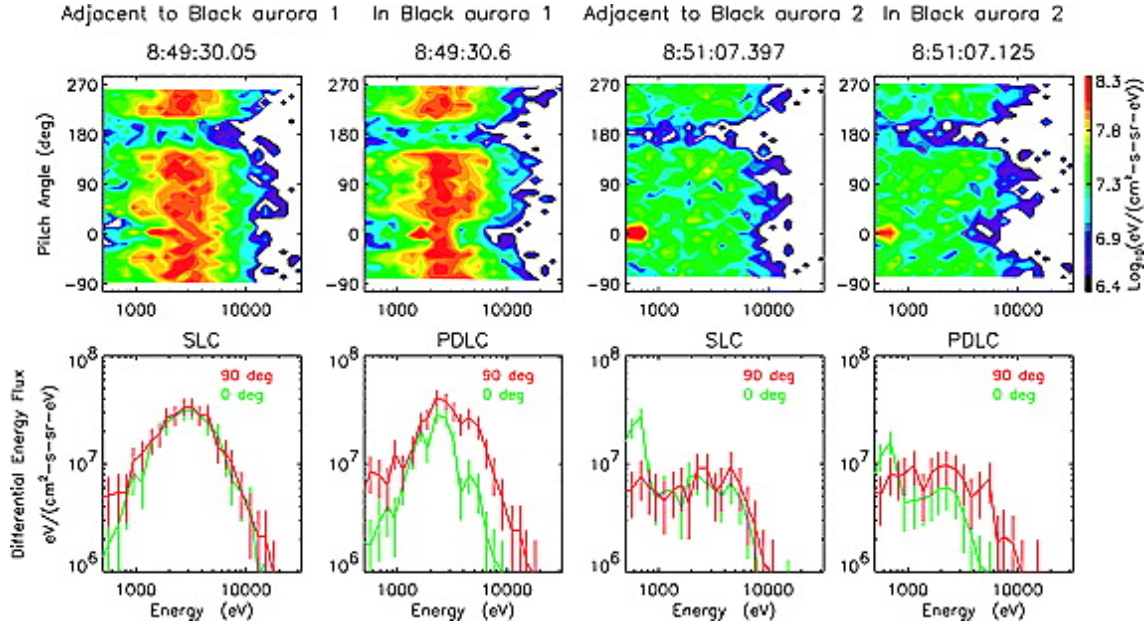


Figure 1.11 A schematic drawing of a possible potential configuration for the convergent electric fields associated with auroral arcs and the divergent electric field associated with black aurora (dark filament) [Marklund *et al.*, 1997].



On the other hand, recently, another generation mechanism for black aurora was proposed by using quasi-simultaneous observation between optical imaging and FAST satellite [Peticolas *et al.*, 2002]. They observed black aurora 40 seconds before and 1 minute after the magnetic footprint of FAST satellite passed the magnetic zenith of a narrow-field camera on board an aircraft. By analyzing the electron spectrum data obtained by FAST, they suggested that the dropouts of electron energy flux associated with black aurora were associated with regions in which pitch angle diffusion causing surrounding diffuse aurora was suppressed at energies greater than 2 keV. As shown in **Figure 1.12**, downward differential energy fluxes for the region adjacent to black auroras are isotropic for energy range greater than 800 eV, showing a single loss cone distribution. On the other hand, those for the regions of inferred black auroras show double loss cone for high-energy electrons. Because precipitations for the region adjacent to black auroras seemed to be caused by pitch angle diffusion, not inverted-V potential structure, they suggested that black auroras obtained by their observations were generated by partial suppression of pitch angle diffusion. Same as previous studies (see Section 1.1), they proposed that surrounding diffuse aurora is due to UB whistler mode waves. These ideas suggest that black aurora region associates with the region where the distributions of hot plasma and cold plasma are different from surrounding region.

As described above, mechanisms for generation of black aurora have already been proposed. However, observational supports based on exact simultaneous observations between optical imaging and in-situ measurement of precipitating electrons have not yet been reported so far because such observations of fine-scale auroral structures including black aurora are extremely difficult. Therefore, the generation mechanism of black aurora has not been identified clearly, and strict simultaneous observations for black aurora are needed to identify the generation mechanism.



**Figure 1.12** Electron energy fluxes as a function of pitch angle and energy (top), and electron differential energy fluxes as a function of energy plotted for two pitch angles [*Peticolas et al.*, 2002]. SLC and PDLC mean single loss cone, and partial-double loss cone, respectively.

## 1.4 Purpose of this thesis

As described in previous sections, there seems to exist discrepancy between optical aurora arcs obtained from ground-based observation and precipitating electrons obtained from satellite and rocket observations, and mechanisms for fine-scale auroral structures including black aurora are not identified yet. The most essential problem is that it is extremely difficult to make completely simultaneous measurements between optical aurora and precipitating electrons with high-temporal and high-spatial resolutions. For example, spatial resolutions of auroral image data obtained by satellites in the past are not sufficient mainly due to their high-altitude orbit ( $\sim 10,000$  km). In addition, spatial resolutions of auroral image with ground-based measurements are degraded due to overlapping of structures in the line-of-sight direction. It is also difficult to have an opportunity of conjugate measurement between optical aurora and precipitating electrons along a magnetic field line between satellite and ground-based instrument.

One of the solutions for these problems is the completely simultaneous measurement between optical imaging and particle with high-temporal and high-spatial resolutions by a single satellite.

Optical imaging and particle instruments on board a satellite will provide us with the simultaneous observation data between auroral emissions and precipitating electrons with high temporal and spatial resolutions by pointing the field-of-view (FOV) of camera toward the magnetic footprint using a three-axis attitude control system. In the present thesis, in order to investigate the fine-scale auroral structures including black auroras, Multi-spectral Auroral Camera (MAC) on board the Reimei satellite has been developed, and analysis of imaging data and particle data for black auroras has been carried out aiming to clarify the precise relationship between optical black aurora and precipitating particles using the Reimei data. Detailed description of Reimei satellite and science instruments are given in **Chapter 2**, special measures for MAC development are given in **Chapter 3**, the methods of observations, satellite operation, and data analysis are given in **Chapter 4**, the results of analysis for black aurora data obtained by Reimei, which include black arc and black patch events and drifting black patch events, are given in **Chapter 5**, possible mechanism for black arc and black patch, and for the drift of black patch proposed by Reimei observation is discussed in **Chapter 6**, and finally the thesis is concluded in **Chapter 7**.



# Chapter 2

## Instrumentation

In the present study, Multi-spectral Auroral Camera (MAC) on board Reimei satellite has been developed in order to investigate the dynamics of fine scale aurora that includes black aurora phenomena. In Section 2.1, detailed description of Reimei satellite is given. The scientific instruments on board Reimei, MAC and Electron and Ion energy Spectrum Analyzer (ESA/ISA), are described in detail in Section 2.2.

### 2.1 Reimei satellite

Reimei is the first of a series of Japanese scientific small satellite project of JAXA/ISAS, and its size and weight are  $724 \text{ mm} \times 626 \text{ mm} \times 609 \text{ mm}$  and about 70 kg, respectively. As mentioned in Chapter 1, science mission of Reimei is the investigation of fine-scale aurora. The Reimei satellite was launched from Baikonur Space Center in Kazakhstan as a piggyback satellite into the sun-synchronous polar orbit with an inclination of 98.6 degree at an altitude of approximately 630 km on August 23, 2005. The orbital meridian is at 0050 – 1250 local time [Saito *et al.*, 2005], and the orbital period is about 98 minutes. Three-channel monochromatic auroral camera (MAC) [Sakanoi *et al.*, 2003] and a top-hat type electron and ion energy spectrum analyzer (ESA/ISA) [Asamura *et al.*, 2003] are on board the Reimei satellite. Combination of these two instruments makes us to observe aurora phenomena by simultaneous imaging and aurora particles measurements with high-temporal and spatial resolutions. In addition, three Langmuir probes, which is called as the plasma current monitor (CRM) and a magnetic field sensor (GAS) are also on board Reimei. GAS is used for deriving attitude vector of the satellite and satellite attitude control. **Figure 2.1** shows the external view of Reimei, and placement of MAC and ESA/ISA on Reimei. **Figure 2.2** shows a 3D CAD drawing of Reimei by opening panels and placement of scientific instruments and control units. A center vector of FOV of MAC is 45 degrees slant in the Z-X plane of the satellite. A schematic drawing of the

orbit of Reimei is given in **Figure 2.3**. All scientific instruments are controlled by Science-Handling-Unit (SHU), which supplies the power and sends the control signal to all scientific instruments. Data obtained by each scientific instrument and the status data of each scientific instrument are also sent to SHU. SHU is controlled by Integrated Control Unit (ICU) on Reimei, and the observation data that are sent to SHU are transferred to ICU. Finally, data are sent to the ground by using telemetry. The diagram of control and data flows is shown in **Figure 2.4**. The memory size of SHU for storing the observation data is 64 M bytes, which limits the amount of simultaneous observation data obtained by both MAC and ESA/ISA for about 7 minutes. Therefore, observation data must be downlinked efficiently. When the science data is sent from the memory of SHU to the memory mounted on ICU, the size of science data is compressed before sending to the ground by telemetry. In this way, efficient data transfer to the ground can be accomplished.

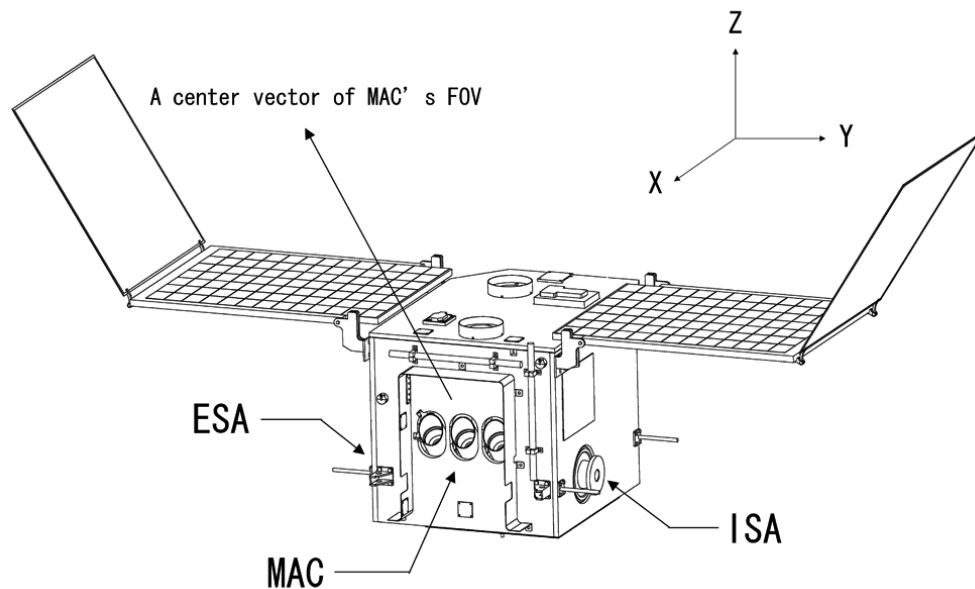


**Figure 2.1** An external view of Reimei satellite and placement of the scientific instruments, MAC and ESA/ISA. A center vector of FOV of MAC is 45 degrees slant in the Z-X plane of the satellite.

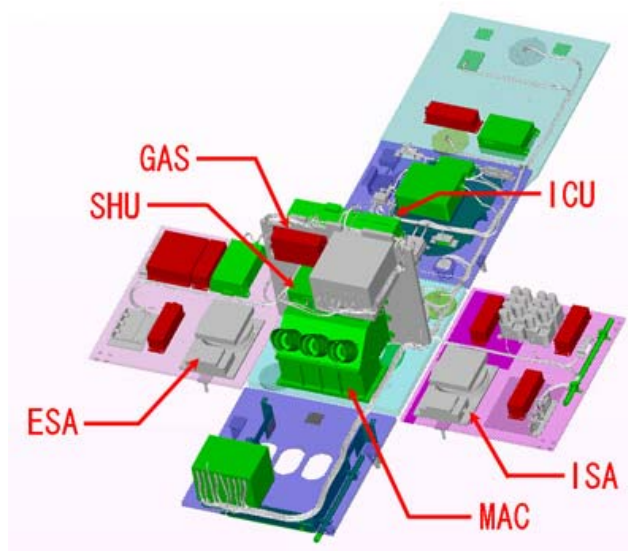


**Figure 2.2 3D CAD drawing of Reimei with panels opened and placement of scientific instruments and control units.**

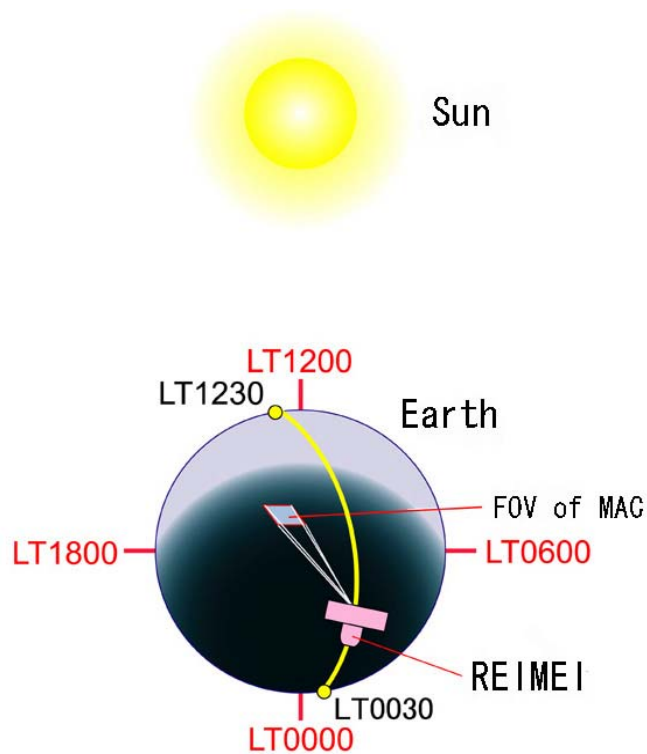


**Figure 2.3 A schematic drawing of Reimei orbit.**

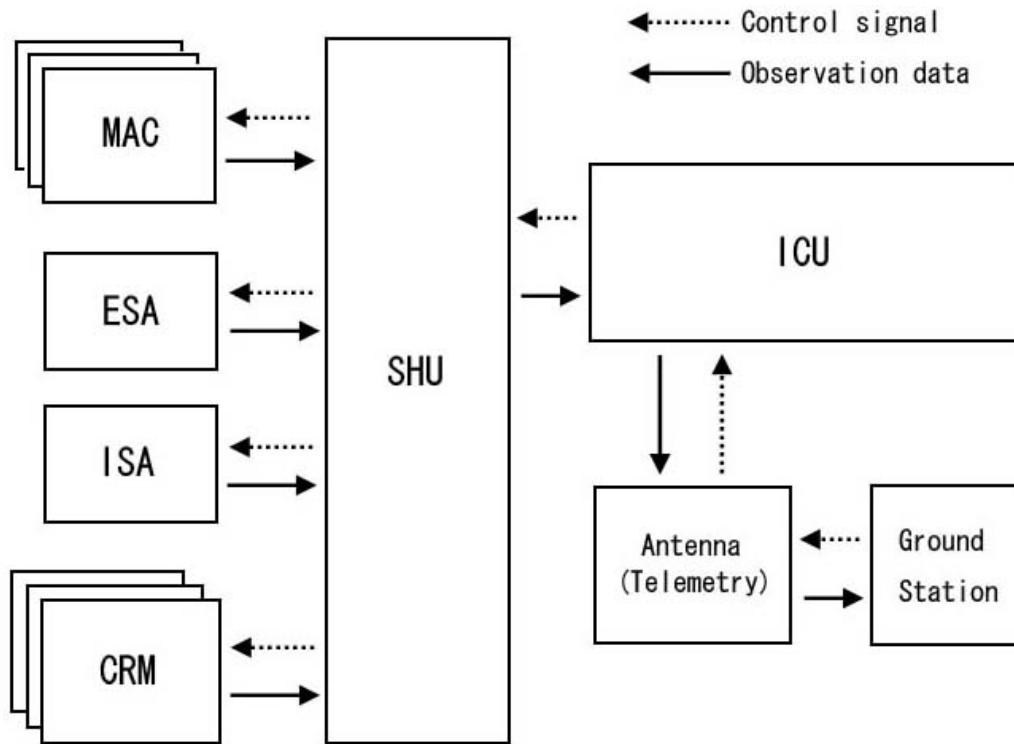


**Figure 2.4** A schematic drawing of flows of control signal and data. The solid arrows denote the flows of control signal, and the dotted arrows are for the flows of observation data.

Attitude control of the satellite is made by the 3-axis bias momentum control using three magnetic torquers and a reaction wheel, and this makes it possible to point any of Reimei's three axes to a desired orientation with high accuracy. Attitude of Reimei is only limited in a way such that the solar cell is facing to the sun within  $\pm 25$  degrees in order to get sufficient power generation. For attitude determination, a star tracker, a spin sun sensor, a non-spin sun sensor, an optical fiber gyro, and a magnetic field sensor are on board Reimei as well. Combination of these attitude measurement equipments can achieve high attitude determination accuracy better than  $\sim 0.05$  degrees. Therefore, simultaneous imaging and particle observations of fine scale aurora can be achieved by pointing field-of-view (FOV) of MAC to a footprint of a magnetic field line threading the satellite, and MAC can also observe altitude distribution of aurora emission by pointing its FOV to the limb of the earth.



## 2.2 Scientific instruments

### 2.2.1 Multi-spectral Auroral Camera (MAC)

**Table 2.1** summarizes the specification of MAC. Because Reimei is a small satellite, MAC had to be made small with light weight. Therefore, its body (consisted of six panels) and the other parts were almost made from aluminum, and we used thin plates with rib structures so that the camera body can tolerate launch environment. As a result, the mass is 4585 g. Additionally, these aluminum plates are coated with black chemglaze in order to reduce scattered stray light. Peak power requirement for MAC is 20.4 W when 3 channels of MAC operate simultaneously. The focal length of the objective lens is 50 mm, and F number is 1.5. Field of view of each channel of MAC is made as small as 7.6 degrees to observe fine scale structure of aurora. When MAC observes aurora emissions pointing its FOV to the magnetic footprint, area of its field of view is about  $\sim 70$  km square when aurora height is 110km. CCD is the interline transfer and front illuminated type with full pixel of  $1024 \times 1024$  (the pixel size is  $6.4\mu\text{m} \times 6.4\mu\text{m}$ ), but three kinds of pixel binning can be applied to the observation for each observation mode (see **Table 2.1**). The detail of observation modes will be described later. The quantum efficiency is about 0.53 at 427.8nm, 0.62 at 557.7 nm, and 0.56 at 670.0 nm. The sensitivity curve of MAC's CCD is shown in **Figure 2.5**. The exposure time can be selected after launch by sending commands from the ground, and the step of exposure time is logarithmic between 130  $\mu\text{sec}$  and 3 sec. In typical observation mode looking to the magnetic footprint, the exposure time is 60 msec. MAC has four observation modes, and temporal and spatial resolutions are different for each mode (see **Table 2.1**).

**Table 2.1 Specification of MAC**

Item	Specification	
Type	3-channel refracting monochromatic imager	
Channel	3 (3 optics, 3 interference filters, 3 CCDs)	
Wavelength	$N_2^+ 1N$ (427.8nm), OI (557.7nm), $N_2 1P$ (670nm)	
Optics	$f = 50\text{mm}$ , $F = 1.5$	
FOV	$7.6^\circ$	
Observation mode	4 (Mode-0, Mode-1, Mode-2, Mode-3)	
CCD	Interline transfer and front illuminated type	
	$1024 \times 1024$ pix	
	binning	$16 \times 16$ pix (Mode-0, Mode-1)
		$8 \times 8$ pix (Mode-2)
		$2 \times 2$ pix (Mode-3)
	$\eta = \sim 0.6$ @ 558nm	
Spatial resolution	$1.2 \times 1.2$ km (Mode-0)	
	$2.4 \times 2.4$ km (Mode-1)	
	$1.2 \times 1.2$ km (Mode-3)	
Temporal resolution	120 msec (Mode-0)	
	1 sec (Mode-1)	
	4.04 sec (Mode-2)	
	480 msec (Mode-3)	
Mass	4585 g	
Power	20.4 W (max.)	

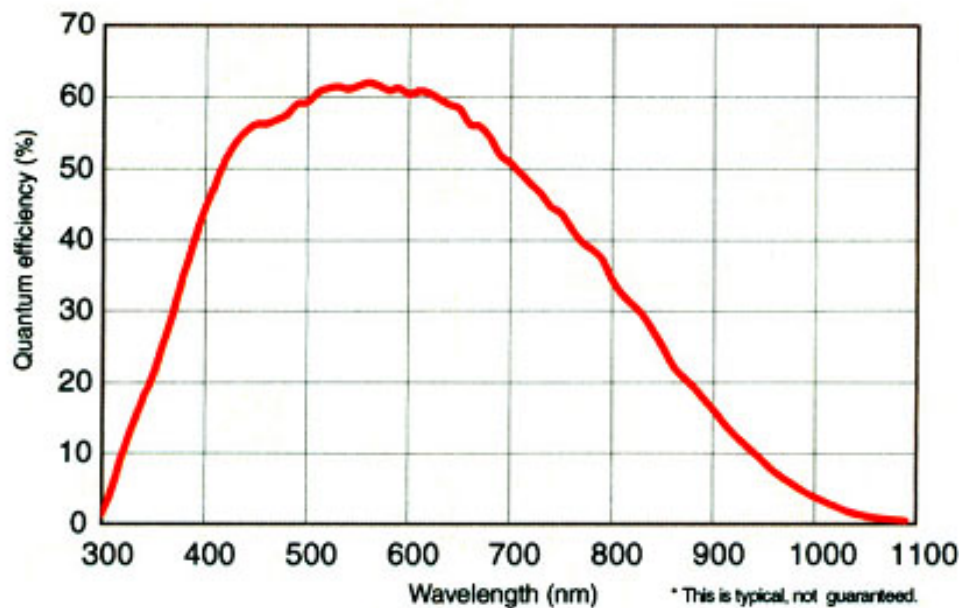


**Figure 2.5** The sensitivity curve of MAC's CCD. The quantum efficiency is about 0.53 at 427.8nm, 0.62 at 557.7 nm, and 0.56 at 670.0 nm.

**Figure 2.6** shows a picture of the flight model of MAC. The optical system consists of refracting optics. The three wavelengths of MAC was chosen so that it can observe  $N_2^+$  1NG (427.8 nm), O green line (557.7 nm), and  $N_2$  1PG (670 nm). For simultaneous observation with particle energy spectrum with high-temporal and spatial resolutions, the 427.8 nm and 670 nm emissions, whose lifetime are very short (the permitted lines), were selected. The forbidden OI 557.7 nm emission was chosen as one of the MAC channel because its excitation process in aurora is thought to relate with  $N_2$  1PG emission. Because MAC has three independent optical systems, it can observe these three emissions completely simultaneously.

In order to make such fast optics with aberration as little as possible, each optics of MAC consists of six synthetic silica lenses, one interference filter and a silica plate that is placed at the foremost of the optics for radiation shield. The radiation shield was made of high quality synthetic silica. These optics has been designed and made by Genesia corporation, and could achieve about 0.8 of total transmission without an interference filter. The interference filters were made by Andover corporation. In each optics, a filter was mounted between the radiation shield and the lense. The FWHM of each filter is; 2.5 nm for 427.8 nm emission, 1.57 nm for

557.7 nm emission, and 38.23 nm for 670 nm emission. The FWHM of filter for 670nm emission is wide compared to other two filters in order to observe  $N_2$  1<sup>st</sup> positive band emission efficiently. Transmission at the center of each filter bandwidth is 0.46 for 427.8nm emission, 0.55 for 557.7nm emission, and 0.90 for 670nm emission, respectively. Each optics is mounted on a cylindrical framework, which is made of aluminum, and these frameworks are coated by black alumite in order to reduce scattered stray light. Furthermore, an aluminum hood coated with black Chemglaze is put on each optics framework. **Figure 2.7** shows the configuration of a unit of the optics and a picture of the cylindrical framework with the lense.



**Figure 2.6 Flight Model (FM) of MAC.**

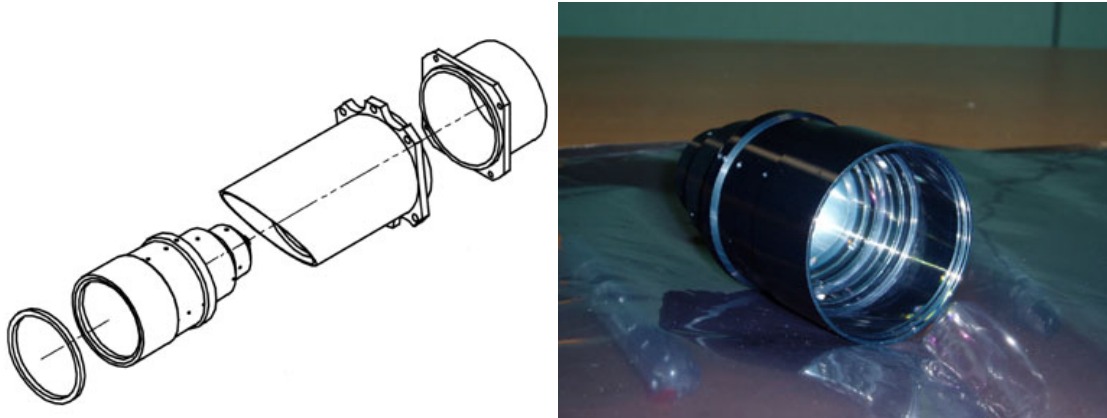


**Figure 2.7** The configuration of a unit of the optics (left figure) and a picture of the cylindrical framework with the lense (right figure). From left to right in the left figure, a attachment ring, a cylindrical framework with the lense, a hood, and a part for connecting with a CCD board.

**Figure 2.8** is a schematic drawing of a cross-section of MAC and its surrounding. Camera electronics of MAC were made by using off-the-shelf commercially available parts. Camera electronics is composed of three CCD boards and two control boards. The two control boards are for power control and for digital data control. The power control board supplies the power, which is fed from the SHU on Reimei, to each CCD boards and digital data control board. The latter control board receives CCD control signal, exposure time and clock and status data of MAC and the timing of data transfer to a dynamic RAM for storing the observation data from SHU, and sends those signals to each CCD boards. This board transfers observation data from CCD boards to SHU as well. These five boards (including CCD boards) are connected with flexible lines. MAC has seven temperature sensors, which are attached on each lens barrel, each CCD boards, and power control board so that the temperature of CCDs and interference filters can be monitored from the ground. Because temperatures on these points affect the performance of CCDs and filters, observation data of auroral emission are also affected. Therefore, monitoring of these temperatures are necessary for accurate observation. These temperature sensors are controlled by above two boards, and these temperature data are sent to SHU as the status data of MAC. They are contained in the observation data every 30 seconds by SHU, and sent to the ground.

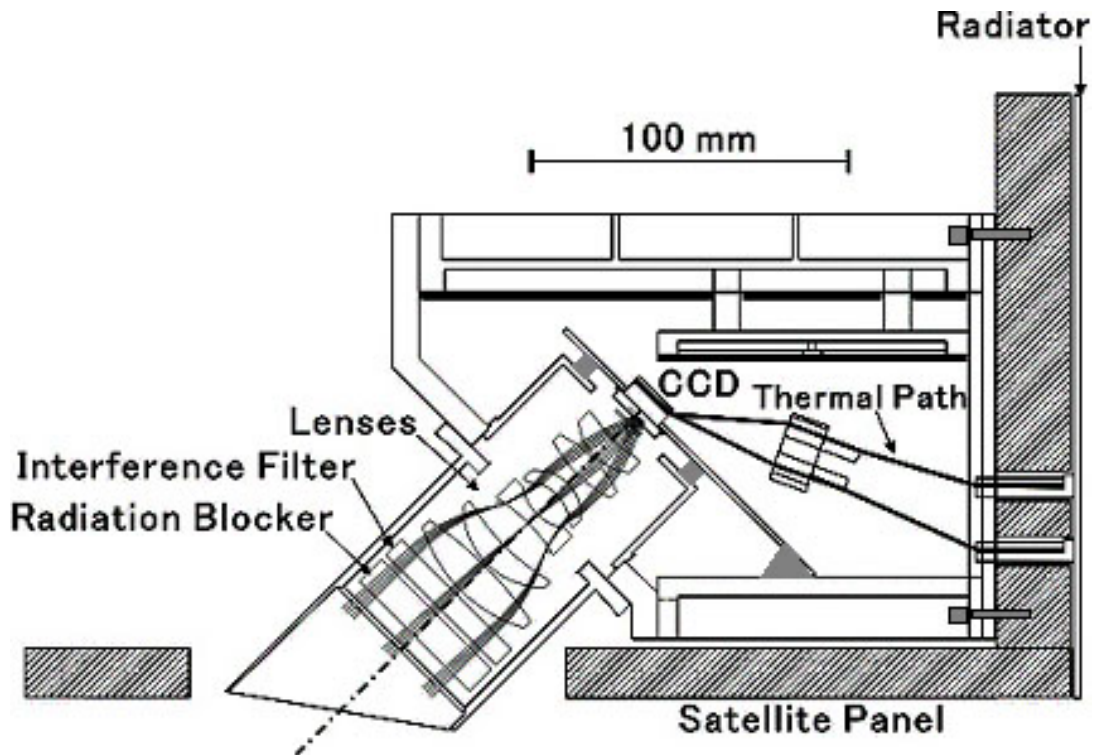


**Figure 2.8** A schematic drawing image of cross section of MAC [Sakanoi *et al.*, 2003].

MAC has four observation modes. The each mode is called as “Mode-0”, “Mode-1”, “Mode-2”, and “Mode-3”. **Table 2.1** summarizes the specification of each observation mode.

“Mode-0” is an observation mode for simultaneous observations between imaging and particle observations with pointing the FOV of MAC to a footprint of magnetic field line threading the satellite. In this mode, a pixel binning, which changes  $1024 \times 1024$  full pixels to  $64 \times 64$  bins (1 bin is formed by  $16 \times 16$  pixels) is made for CCDs of MAC. The spatial resolution of this observation mode is about 1.2 km when MAC observes emissions of 110 km altitude. Because Reimei moves along an orbit at 630 km altitude with about 8 km/s velocity, exposure time of this observation mode must be short. Therefore, the time resolution of this mode is selected to 120 msec by considering that SHU can control all scientific instruments every 40 msec. On this mode, exposure time can be selected between 130  $\mu$ sec and 106 msec, and nominal exposure time on orbit is selected to be 60 msec.

“Mode-1” is an observation mode with which MAC observes altitude distribution of aurora emission with pointing its FOV to the limb of the earth. By observing aurora phenomena with

this observation mode together with ground-based instruments, which are e.g. ALIS, EISCAT/ESR and SuperDARN radars, simultaneously, we can investigate the altitude distribution of aurora emission and the phenomena taking place in the ionosphere. On this observation mode, pixel binning is made making  $1024 \times 1024$  full pixels to  $64 \times 64$  bins, similar to “Mode-0”. Therefore, if MAC observes the altitude distribution of emission structure with this mode, assuming that the distance to aurora is 2000 km away from Reimei, the spatial resolution is about 4 km. The temporal resolution is 1 sec, and nominal exposure time is selected to be 480 msec since the auroral intensity is expected to be weaker than the emission that MAC observes with Mode-0.

“Mode-2” is a calibration mode with which MAC observes stars, ground structures and coastlines in order to determine the absolute direction of its FOV. By observing stars and the earth’s surface, we can calculate angles of MAC’s FOV relative the three axis of the satellite and calibrate its FOV. After the launch, we have corrected the direction of MAC’s FOV using the image data of stars and land features obtained by MAC using this observation mode. The pixel binning on this mode is  $512 \times 512$  bins (1 bin is formed by  $2 \times 2$  pixels), and the spatial resolution is about 150 m when FOV points to a sub-satellite point. The temporal resolution is 4 sec, because a data size obtained in this observation mode is larger than Mode-0 and Mode-1 and the transfer time of an image data is rather long. The exposure time is about 1.9 sec for the observation of stars brighter than 5 magnitudes.

“Mode-3” is an observation mode for auroral observation with higher spatial resolution than Mode-0 and Mode-1. Therefore, minimum detectable sensitivity on this mode is lower than Mode-0 and Mode-1. The pixel binning on this mode is  $128 \times 128$  bins (1 bin is formed by  $8 \times 8$  pixels), and the spatial resolutions are about 600 m when MAC observes the magnetic footprint direction, and about 2 km when MAC observes the limb region that is 2000km away from Reimei. The temporal resolution is 480 msec, same as Mode-2, and this is longer than Mode-0 and Mode-1. If appearance of strong aurora emission is forecasted from some geomagnetic indices, e.g., Auroral Electrojet (AE) index, Kp index, we can make a plan of aurora observation using this observation mode.

### 2.2.2 Electron and Ion energy Spectrum Analyzer (ESA/ISA)

Electron and Ion energy Spectrum Analyzer (ESA/ISA) were developed in JAXA/ISAS [Asamura *et al.*, 2003]. **Figure 2.9** shows a cross section drawing of ESA/ISA. **Table 2.2** shows the specification of ESA/ISA. These sensors are top-hat type electrostatic analyzers. Observable energy range is from 10 to 12000 eV/q and number of step of observation energy is logarithmic 32. FOV is 4 x 300 degree, and if a vector perpendicular to its FOV is pointed to the direction perpendicular to a magnetic field line threading the satellite, these instruments are possible to observe energies of electron and ion covering almost all pitch angles. Temporal resolution is 1.25 msec for a unit energy step, therefore, temporal resolution for obtaining all energy range is 40 msec.

**Table 2.2 Specification of ESA/ISA**

Item	Specification
Type	Top-hat type electrostatic analyzer
Energy range	10 – 12000 eV/q
Energy step	32 (logarithmic)
FOV	4 × 300 deg.
Angular resolution	30 bins in polar angle direction
Temporal resolution	1.25 msec / energy step
Mass	1.4 kg for each sensor
Power	2.5 W for each sensor
G-factor	ESA: $2.8 \times 10^{-4}$ , ISA: $4.9 \times 10^{-4}$ [cm <sup>2</sup> sr eV/eV/10 deg]



### Sectional view of ESA/ISA

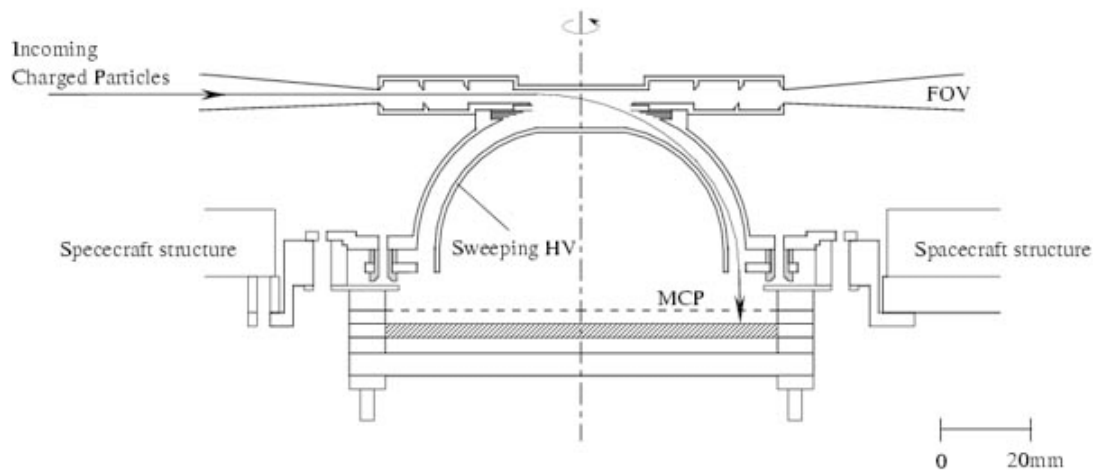


**Figure 2.9** A drawing of cross section of ESA/ISA.



## Chapter 3

# Development of Multi-spectral Auroral Camera

In the preceding Chapter, description of Multi-spectral Auroral Camera (MAC) on board Reimei satellite has been given. During the development stage of MAC, a variety of special measures were needed to achieve satisfactory operation of MAC. In this chapter, such special measures for MAC development, which include thermal paths for cooling CCD and components of the circuit board, adjustment of focus, space environment tests, and sensitivity calibration, are described.

### 3.1 Thermal path for cooling CCD and components on the circuit board

Because the camera electronics is made of off-the-shelf commercial products, the performance in space environment is not guaranteed and it was necessary to check their performance in simulated space environment and to make improvements when a problem is found. One of the important improvements is development of the thermal path for cooling CCD. In order to observe fine scale aurora structures with high temporal resolution, CCD noise has to be reduced as low as possible. For reduction of CCD noise, it is usual to cool the CCD by reducing thermal noise. However, because we used off-the-shelf commercial products, CCD system used for MAC does not have a thermoelectric cooling elements such as the peltie device to reduce the noise, and there was no way to cool actively the CCD. Therefore, a thermal path for each CCD which was composed of a bundle of 20 stacked graphite sheets (0.1mm thickness for each sheet), an oxygen-free copper block and aluminum parts were fabricated. **Figure 3.1** shows a bundle of the stacked graphite sheets covered with a kapton tape. One end of the graphite sheets bundle passes through a hole on the back-panel of MAC from inside (**Figure 2.8**, **Figure 3.2**), and is attached to a radiation-plate, which is made of aluminum coated with silver

evaporated teflon tape to improve the emissivity. **Figure 3.3** is a picture of the radiation-plate. As described above, these thermal paths connect between CCDs and a radiation-plate. The radiation-plate is placed facing to the space right behind the satellite panel, and the heat produced on CCD is dissipated from the radiation-plate by radiation cooling. The thermal paths are attached to the backside of CCD and the radiation-plate by putting an Indium foil between two elements to increase the heat conductivity. A thermal vacuum test was conducted to check if each CCD was sufficiently cooled and if dark noise on CCD image can be reduced satisfactory for observation of weak auroral emission. As a test result, the thermal path worked quite satisfactory; CCD could be cooled down to lower than 0 degrees Celsius, and MAC could perform in simulated space environment. The noise on dark image data at 0 degrees Celsius was about 3 counts (standard deviation). In this test, by changing the temperature inside a thermostatic vacuum chamber by 1 degree C between -10 and 20 degrees Celsius, and operating MAC with all observation-mode, we could get dark noise data at every temperature and observation mode. By using these data as a reference, observation image data obtained by MAC have been processed. After launching Reimei, it was confirmed that this CCD cooling system showed good performance and the CCD was always cooled down to below -7 degrees Celsius in orbit.



**Figure 3.1** Picture of bundles of 20 stacked graphite sheets used as a thermal path for cooling of CCD. It is covered with kapton tape. One side of the graphite sheets bundle is attached to the backside of CCD with an oxygen-free copper block, and the other end is attached to the radiation plate (Figure 3.3), which is placed facing to the space right behind the satellite panel, with aluminum block (Figure 3.2).

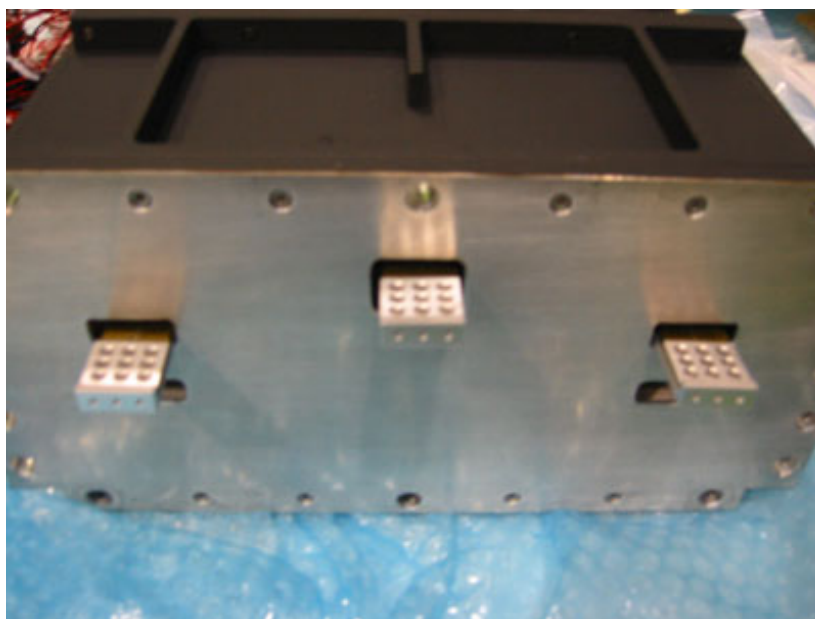


**Figure 3.2** A picture of the bottom side of MAC. Three parts sticking out of the bottom plate are the thermal paths with aluminum block for attaching to the radiation-plate, which is placed facing to the space (see Figure 2.8).

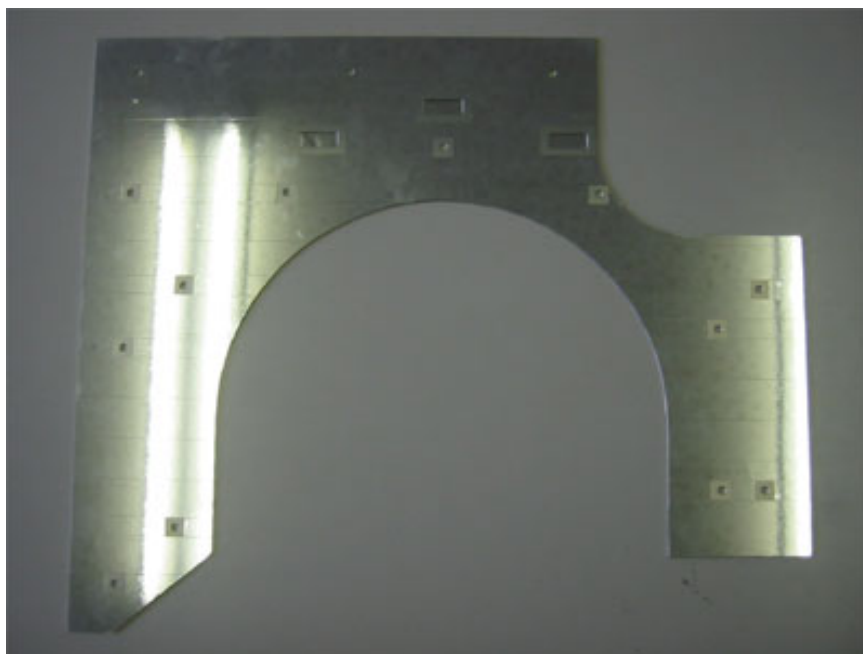


**Figure 3.3** A radiation-plate made of aluminum. It was coated with silver evaporated teflon tape to improve its emissivity.

By taking infrared images of the electronics boards in operation, it was found that some elements on CCD boards and power control board had reached the temperature exceeding 60 degrees Celsius (**Figure 3.4**). It was expected that these elements would reach to a temperature higher than guaranteed temperature of each component in space environment because the test was carried out in the atmosphere. Therefore, we developed thermal paths that transfer heat from heated components to the camera body. **Figure 3.5** shows the thermal path for cooling heated components on the power control board of MAC. These thermal paths are made of aluminum blocks directly protruding from a MAC body panel facing its inside to the power control board, and copper mesh sheets, and they connect between heated components and the camera body using Indium foils in between for increasing heat conductivity between the two elements. It was confirmed that the temperature of these elements was maintained lower than the guaranteed temperature at least for 11 minutes in the thermal vacuum test.

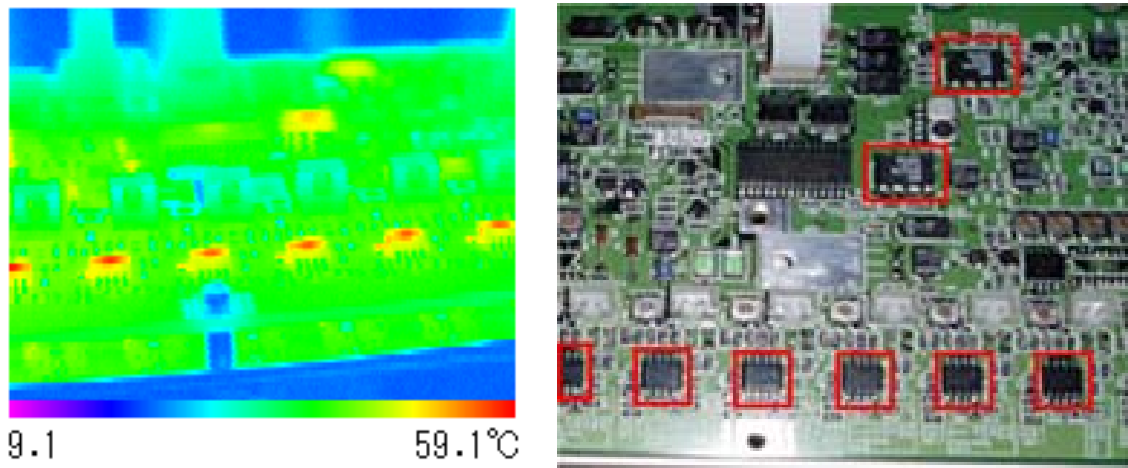


**Figure 3.4** An infrared image of the electronics board while it is in operation (left), and a picture of the same board taken by a digital camera (right). In the right figure, components denoted by red squares correspond to high-temperature components that are shown by yellow to red color in the left picture.

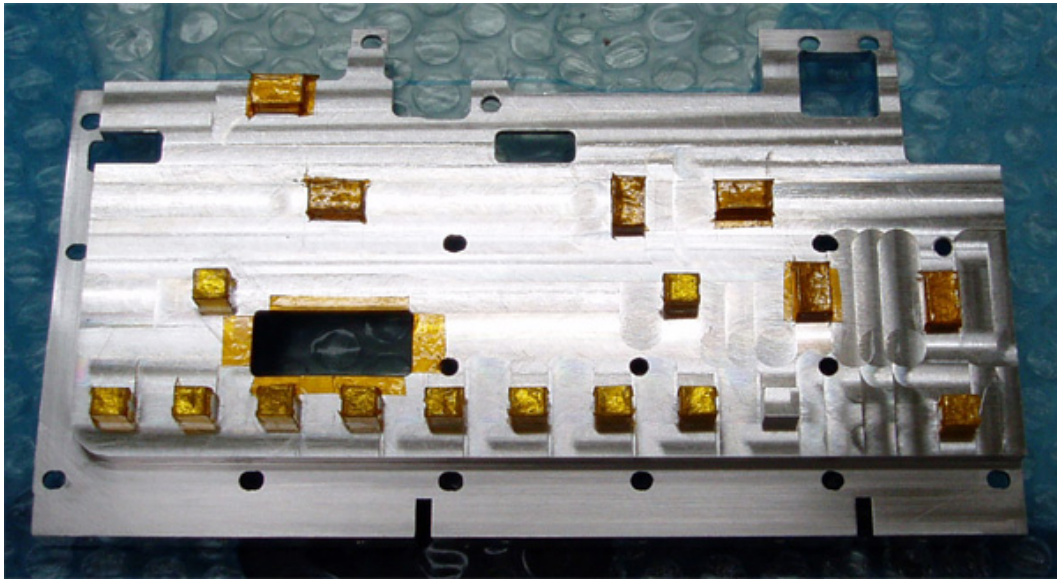


**Figure 3.5** The thermal path for cooling heated components on the power control board of MAC. The brown colored convex elements are pressed against the heated components inserting an Indium foil between them.

### 3.2 Adjustment of lens focus

As a result of analysis of spot diagrams of optics, it was found that the lens focus had to be adjusted with an accuracy better than  $10\mu\text{m}$ . For this adjustment, we have developed a system with a collimator using a refracting telescope. A schematic drawing of this system is shown in **Figure 3.6**.

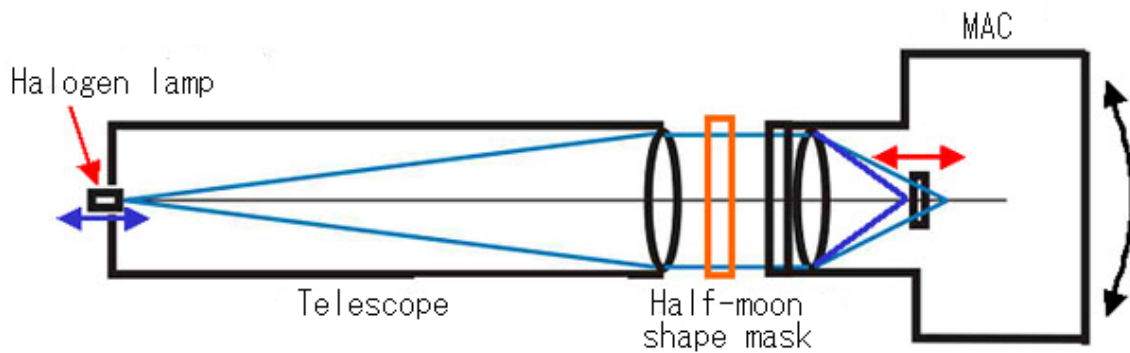


**Figure 3.6** A schematic drawing of focus adjustment.

As seen in **Figure 3.6**, this system is consisted of a halogen lamp, a telescope, and a half-moon shape mask. The light from a halogen lamp passes through a pinhole which is placed at a focal point of the telescope for infinity, and it is converted to a parallel beam by a telescope (collimator). In the parallel beam, a half-moon shape mask is placed. The mask blocks half of the parallel beam (**Figure 3.7**), and the remaining half beam focuses on CCD. Here, the experimental set up was made it possible to rotate MAC around the lens center. A half-moon shape mask can be half turned, and when CCD surface is not at the lens focus, an image of half-moon shape will be focused on CCD as shown in **Figure 3.7**. A straight line crossing the CCD area from top-left to bottom-right is a locus of the lens focal point on CCD when MAC is rotated. **Figure 3.7** shows an example when image is taken with MAC being rotated so that image is formed at top-left corner of the CCD area. The centroid position of the image on CCD is not right on the locus line. In other words, as the position of CCD goes away from the focal position, the distance between the centroid position of the image on CCD at the angle of half-moon mask of 0 degrees and the one at the angle of half-moon mask of 180 degrees will increase. The amount of adjustment of focus can be estimated by shifting the position of light source (pinhole) back and forth and measuring the distance between the both centroid positions of the image on CCD.

If the focal length of MAC is A (nominal value 50 mm), the focal length of collimator (telescope) is B, the moving distance of the light source (pinhole) is C, and the moving distance of the image plane is D, the relation among them can be approximated as below when  $A \gg D$  and  $B \gg C$ .

$$C \doteq \left( \frac{B}{A} \right)^2 D \quad (3.1)$$

For instance, if the position of the light source (pinhole) is put 1 mm closer to CCD, the position of the imaging plane will be away from the lens by  $(A/B)^2$  mm. Because the focus has to be adjusted with an accuracy better than 10  $\mu$ m, a telescope with a focal length of 500 mm was selected and the position of the light source (pinhole) was shifted back and forth with an accuracy of 1 mm.

CCD board of MAC is attached to the optical unit with four screws (see **Figure 2.8**, **Figure 3.8**). Therefore, for adjusting inclination of the normal to CCD surface against the optical axis,



the light from halogen lamp was focused at four corners of CCD area.

After carrying out above mentioned measurements, a relation between the distance of the light source (pinhole) from the designed nominal value and the distance between the centroid position of the image at the angle of half-moon mask of 0 degrees and the one at the angle of half-moon mask of 180 degrees is obtained as shown in **Figure 3.9**. In this figure, a black line shows a result of fitting. From the intercept point of this fitting line at the value of image centroid shift of zero, the amount of adjustment of focus can be estimated from equation (3.1). From such estimation, the focus was successfully adjusted with an accuracy better than 10  $\mu\text{m}$  by using shims with various thicknesses (**Figure 3.10**). After inserting shims, above measurements were carried out again for checking validity of the adjustment.

Measurements and adjustments described above were applied to each channel of MAC in the atmosphere. The refraction index of the atmosphere has to be taken into account because MAC will operate in vacuum. Therefore, the focus of each channel was adjusted for a space environment by using following formula.

$$(n_s - 1) \times 10^8 = 6432.8 + 2949810 / \left( 146 - \frac{1}{\lambda^2} \right) + 25540 / \left( 41 - \frac{1}{\lambda^2} \right) \quad (3.2)$$

Here,  $n_s$  is the refraction index in the atmosphere,  $\lambda$  is the wavelength in  $\mu\text{m}$ . This formula can be applied for the wavelength range from 0.2  $\mu\text{m}$  to 1.35  $\mu\text{m}$ . Using this formula, the refraction index for each channel of MAC is calculated to be 1.00028141 at 427.8 nm, 1.00027767 at 557.7 nm, and 1.00027608 at 670 nm. The focal length in vacuum can be calculated by multiplying these refraction indices to the focal length of MAC in the atmosphere (50 mm), and each focal length in vacuum becomes to 50.01407 mm at 427.8 nm, 50.01388 mm at 557.7 nm, and 50.01380 mm at 670 nm. Accordingly, each amount of adjustment for the focal position in vacuum is 14.07  $\mu\text{m}$  at 427.8 nm, 13.88  $\mu\text{m}$  at 557.7 nm, and 13.80  $\mu\text{m}$  at 670 nm. By using these values, the focus of MAC was finally readjusted for space environment.

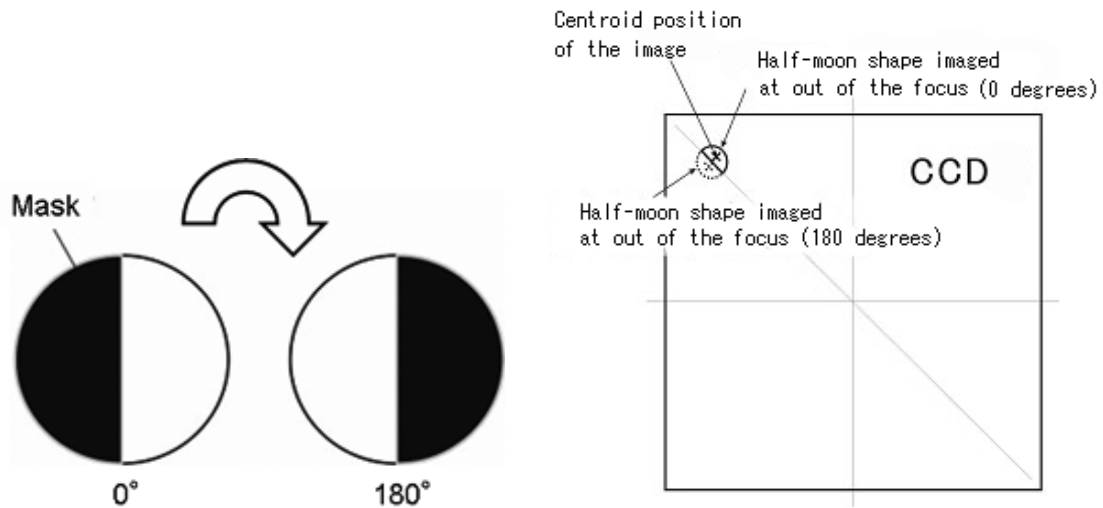


**Figure 3.7** Schematic drawing of half-moon shape mask (left figure) and half-moon shape image on CCD when out of focus (right figure). A half-moon shape mask can be half turned, and the image of half-moon shape is focused as seen in the right figure.



**Figure 3.8** A picture of CCD board of MAC. Four red circles denote the point of screw cramp that connects each CCD board to the optical unit.

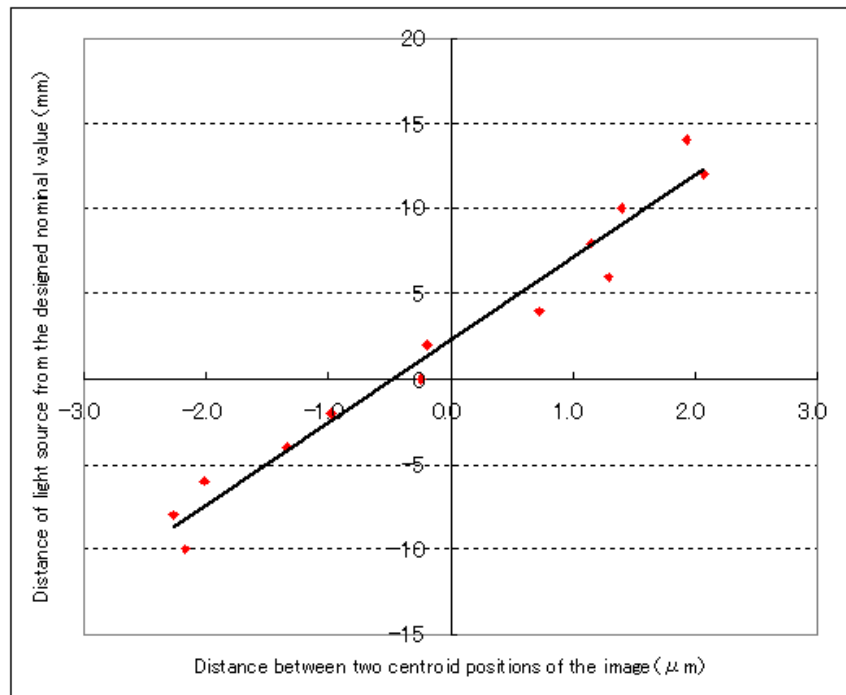


**Figure 3.9** Distance between the centroid position of the image with the angle of half-moon mask of 0 degrees and the one with the angle of half-moon mask of 180 degrees versus the distance of light source from the designed nominal value. A straight black line is a fitting to the measurements. From the intercept point of this fitting line at the value of image centroid shift of zero, the amount of adjustment of focus can be estimated.



**Figure 3.10** Picture of a shim that was used for adjustment of the focus. Shim such as shown in this figure was inserted between the optical units and CCD board (see Figure 2.8 and Figure 3.8).

### 3.3 Environment tests

At the launch of a satellite, instruments on board the satellite have to survive severe vibration and shock environment. In addition, radiation damage to CCD and other devices within MAC is expected in space environment after the launch. Therefore, every instrument on board a satellite has to show its durability against these environments. In this section, results of the vibration and shock tests that simulate at the launch environment, and the radiation test that simulates the space environment for MAC are described.

#### 3.3.1 Vibration test

At the launch of a satellite, characteristic vibration of a launch vehicle is given to a satellite. Therefore, effect of such vibration for an instrument has to be checked. In the case of MAC, not only durability for vibration but also optical misalignment arising from launch environment had to be evaluated. For this test, the components on each circuit board, thermal paths, and screws fixing body panels and every component were locked by using space-qualified adhesive. The vibration test for MAC was carried out at JAXA's Tsukuba Space Center. In this vibration test, random vibration with a level of about 16 Grms and frequency from 20 to 2000 Hz was applied to MAC. As a result of this test, it was confirmed that MAC is durable enough for the vibration that will be expected at the launch. In addition, by using the system that has been described in the preceding section, it was checked whether there was any change in the optical system of MAC. As a result of this check, a small amount of CCD displacement relative to the lens due to vibration test was measured. The result was within 10  $\mu\text{m}$  for all three channels as given in **Table 3.1**.

**Table 3.1 Amount of CCD displacement relative to the lens after vibration test**

Channel	Amount of misalignment from focal point ( $\mu\text{m}$ )
Channel1 (427.8 nm)	10
Channel2 (557.7 nm)	3
Channel3 (670 nm)	1

### 3.3.2 Shock test

When a satellite is separated from a launch vehicle, a mechanical shock is expected for each instrument on board the satellite. Accordingly, every instrument on board a satellite has to be durable enough for such shock. Because the shock with a level of about 1000 G at a frequency range of a few thousand Hz was expected for MAC as shown in **Figure 3.11**, there is possibility that precise mechanical components, interference filters, and lenses are damaged. In the case of MAC, there was possibility that interference filters and lenses would be damaged and CCD would become out of alignment and focus by the shock. Because of Reimei's structure, the shock would be given from the bottom side of MAC. Therefore, a shock that simulates the launch environment was given by striking by a human on the bottom side of MAC as shown in **Figure 3.12**. For this test, MAC was attached on a hanging thick aluminum plate. After the shock test, MAC operated normally and image data with same quality as before the test were obtained. This test confirmed that MAC is durable enough for the shock that will be expected at the launch. In addition, by using the system that was described in the preceding section, it was checked whether there had been any change in the optical system of MAC. The check showed a small amount of CCD displacement relative to the lens due to the shock test. Amount of displacement was within 10  $\mu\text{m}$  for all three channels as given in **Table 3.2**.

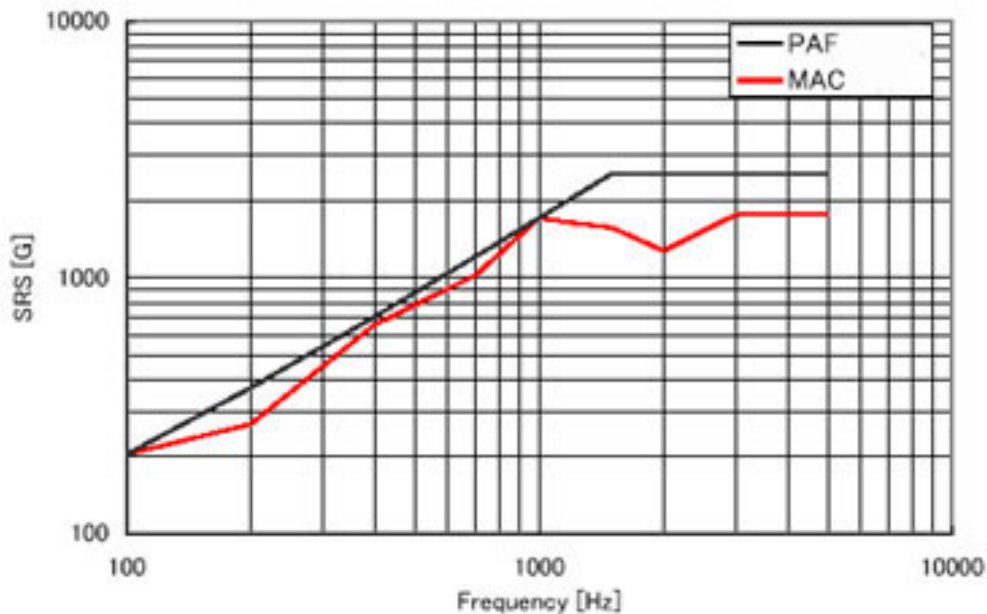


**Figure 3.11** Required level of shock for MAC (red line).

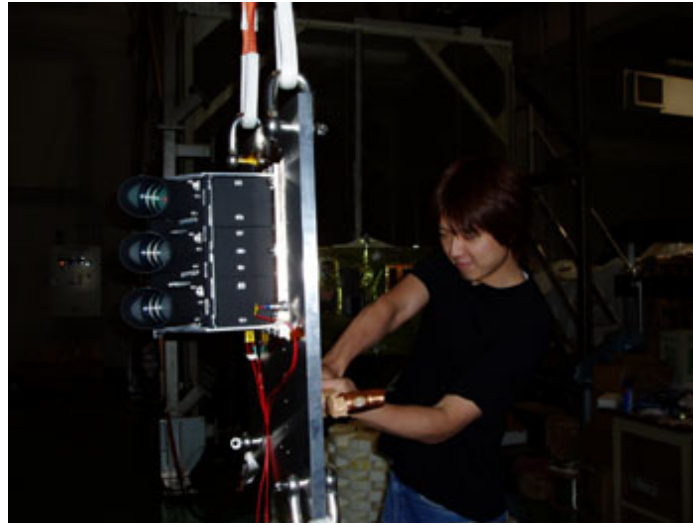


**Figure 3.12** A picture of the shock test. MAC was attached on a hanging thick aluminum plate. The shock was given by striking on the bottom side of MAC.

**Table 3.2** Amount of misalignment from focal point for each channel of MAC after shock test

Channel	Amount of misalignment from focal point ( $\mu\text{m}$ )
Channel1 (427.8 nm)	3
Channel2 (557.7 nm)	5
Channel3 (670 nm)	1

### 3.3.3 Radiation test

In space environment in which a satellite orbits, the satellite is expected to be illuminated by high intensity radiation. Therefore, instruments on board a satellite can be fatally damaged by the radiation in orbit. Each optical component of MAC is made of synthetic silica and a radiation shield which is made of high quality synthetic silica with a thickness of 10 mm is put in front of the optics. Nevertheless, it was expected that CCDs could be damaged by radiation

which would come from directions such as shown in **Figure 3.13**. Therefore, we have checked radiation effect on CCDs and interference filters of MAC using an engineering model of MAC by applying proton beam of 100 MeV. As for interference filters, the radiation was applied to them with radiation shields in order to simulate the space environment. **Table 3.3** gives the total dose amount of radiation that applied to CCD and each interference filter. The test result showed that MAC is sufficiently tolerate for radiation expected for Reimei's nominal lifetime of three months. Specifically, transmittance of interference filters decreased by only 1 % by applying 9 Krad total doses and such small transmittance change does not affect aurora observation by MAC. The 9 Krad total dose corresponds to the amount of three years total dose at an orbit of Reimei.

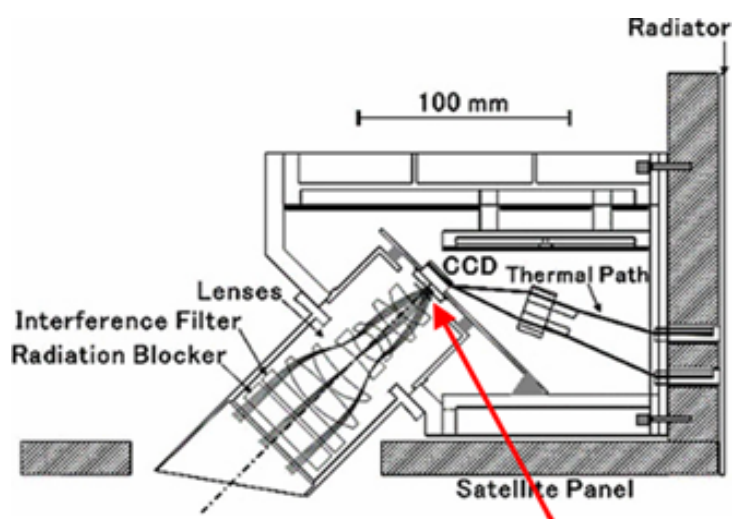


**Figure 3.13** A schematic drawing of MAC and the direction which the radiation would illuminate MAC (a red arrow).

**Table 3.3** Total dose of radiation applied CCD and interference filters.

Target	Amount of total doze
CCD	9krad
Interference filter (427.8 nm)	1krad
Interference filter (557.7 nm)	10krad
Interference filter (670 nm)	3krad

### 3.4 Sensitivity calibration

After assembly of MAC and its environment tests were finished, we have carried out the sensitivity calibration of MAC using an integrating sphere at National Institute of Polar Research. **Table 3.4** summarizes the result of calibration. The formula and factors used for this calibration are as below,

$$N = I(10^6/4\pi)A\Omega T\eta tE \quad (3.3),$$

where N is the count in image obtained by MAC [cts/sec], I is emission intensity [Rayleigh], A [cm<sup>2</sup>] is the effective area of MAC's optics (8.72 cm<sup>2</sup>),  $\Omega$  [str] is the solid angle of one bin extended from the lens center, T is the transmission of optics,  $\eta$  is the quantum efficiency of CCD, t [sec] is the exposure time, and E [electron/count] is the A/D conversion unit of CCD, (3.74). In this calibration, sensitivity for each observation mode for each channel is determined by using values of solid angle, transmission, and quantum efficiency. The solid angle is different for each observation mode because a size of one bin is different for each mode (see the section 2.2). The transmission of optics and the quantum efficiency of CCD are different for each channel (wavelength). In this calibration, image data with three different exposure times and three different emission intensities for each channel of MAC were obtained. Accordingly, a total of nine data for each channel were obtained and they are summarized in **Table 3.4**. Sensitivity calibration showed that MAC has sufficient sensitivity and noise equivalent intensity of aurora is estimated to be about 200 R.



**Table 3.4 Sensitivity and dynamic range of MAC**

Observation Mode	Wavelength	Sensitivity [ R / count / ms ]	Dynamic range [ R ]
Mode-0	427.8nm	$8.14 \times 10^3$	$0 - 321 \times 10^3$
	557.7nm	$5.99 \times 10^3$	$0 - 219 \times 10^3$
	670nm	$5.63 \times 10^3$	$0 - 210 \times 10^3$
Mode-1	427.8nm	$8.14 \times 10^3$	$0 - 63.2 \times 10^3$
	557.7nm	$5.99 \times 10^3$	$0 - 42.8 \times 10^3$
	670nm	$5.63 \times 10^3$	$0 - 41.2 \times 10^3$
Mode-2	427.8nm	$525 \times 10^3$	$0 - 1.94 \times 10^9$
	557.7nm	$394 \times 10^3$	$0 - 1.33 \times 10^9$
	670nm	$363 \times 10^3$	$0 - 1.25 \times 10^9$
Mode-3	427.8nm	$32.8 \times 10^3$	$0 - 172 \times 10^3$
	557.7nm	$24.3 \times 10^3$	$0 - 117 \times 10^3$
	670nm	$22.9 \times 10^3$	$0 - 116 \times 10^3$



# Chapter 4

## Observation and data analysis

Aurora observation by Reimei is the primary target of the present study and it was successfully carried out. Methods of observation by Reimei, operation of Reimei, and methods of data analysis are described in this chapter.

### 4.1 Methods of observation

As described in Chapter 2, attitude control of Reimei is made by 3-axis bias momentum control. Therefore, FOV of MAC can be pointed to a desired orientation if the solar cell is facing to the sun within  $\pm 25$  degrees in order to get sufficient power generation. Reimei can not be controlled at a time of aurora observation by using telemetry from Japan because the aurora oval is located in quite high latitudes and Reimei is not visible from Japan. Therefore, the commands for carrying out aurora observation and for attitude control of the satellite need to be stored in advance and they have to be executed automatically at the time of aurora observation. Such commands are called as Stored Commands (SC). In this section, the methods of simultaneous image and particle observation, arbitrary pointing observation, magnetic field tracking observation will be described and methods of generating SC for each observation are given.

#### 4.1.1 Simultaneous image and particle observation

In order to achieve simultaneous observations by imaging and aurora particle measurements, it is needed to point the FOV of MAC to a footprint of a magnetic field line threading the satellite and point the FOV of ESA/ISA, which is  $4 \times 300$  degree, to a direction perpendicular to a magnetic field line threading the satellite so that these particle analyzers can observe particle

energies for full pitch angle. A schematic drawing of this observation is shown in **Figure 4.1**.

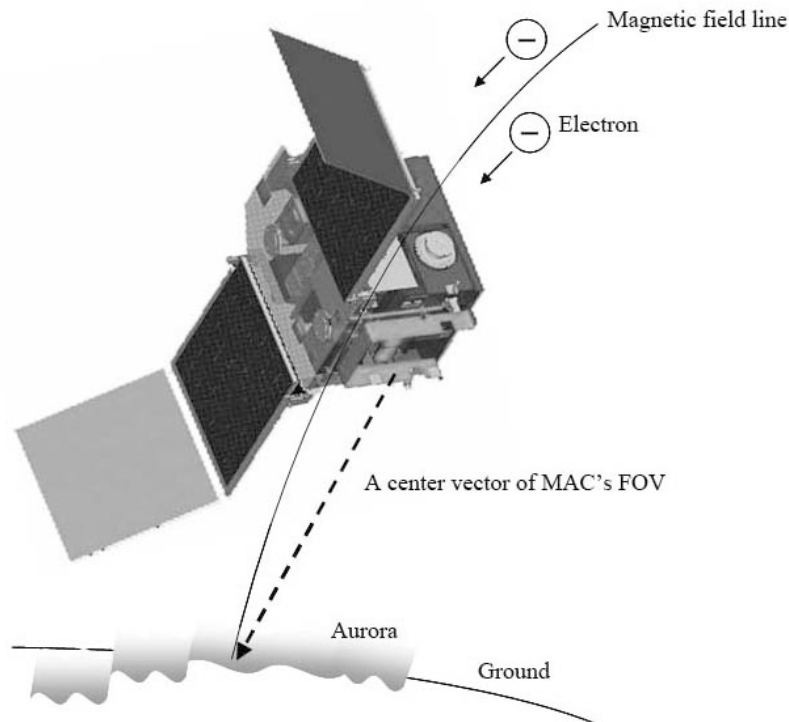


**Figure 4.1** A schematic drawing of simultaneous image and particle observation. In this observation, the FOV of MAC is pointed to a footprint of a magnetic field line threading the satellite.

Configuration between the satellite and a footprint of a magnetic field line threading the satellite is different for a time of observation and a location of the satellite. Therefore, the attitude of the satellite for simultaneous image and particle observation has to be computed for each date, time, and location of the satellite when observation will be carried out. For attitude determination of the satellite, a tool utilizing computing code has been developed in this study. This tool uses prediction orbit files, which is produced at Tsukuba space center, and the earth's magnetic field data calculated by the IGRF model is employed as input data. The prediction

orbit files include the location of the satellite and footprint of a magnetic field line threading the satellite every 1 minute. The locations are given as three components in geodetic coordinate system. By reading prediction orbit files, a vector of MAC's FOV can be computed. In addition, by referring a direction of the magnetic field line at a location of the satellite, a vector of ESA/ISA's FOV is computed. Accordingly, this tool can compute feasible attitude of the satellite every one minute. At the same time, an angle between a normal line to the solar cell of the satellite and the sun is computed after three vectors of Reimei's attitude are converted to three vectors in Geocentric Solar Ecliptic coordinate system (GSE coordinate system). If the angle is within a certain limit, which is 25 degrees, the time and three vectors of Reimei's attitude at that time is output. Then, three vectors of the attitude of the satellite are converted to three vectors in Geocentric Equatorial Inertial coordinate system (GEI coordinate system), in which equinox is selected to J2000. In addition, the tool checks whether the locations of a footprint of a magnetic field line threading the satellite and the satellite itself are in the aurora oval and not sunlit. The 3-axis vectors of the satellite are finally converted to a vector constructed by 4 elements, called as "q-value". The q-value is used to simulate the sequence of attitude control of the satellite, and the detail for this simulation is described in the following section, Section 4.2. This tool also outputs the observation commands including the execution time. In the simultaneous observation, Mode-0 is selected for MAC as default. In case when high aurora activity is forecasted, Mode-3 is selected for MAC. A flowchart of procedures given above is shown in **Figure 4.2**. The observation commands and commands of attitude control of the satellite that are made by using the q-value are uplinked for operation of Reimei (see Section 4.2). Owing to automatic generation of commands by using this tool (see Section 4.2), we have been successful to get a lot of simultaneous observation data with a rate of more than 80 % in all Reimei passes.

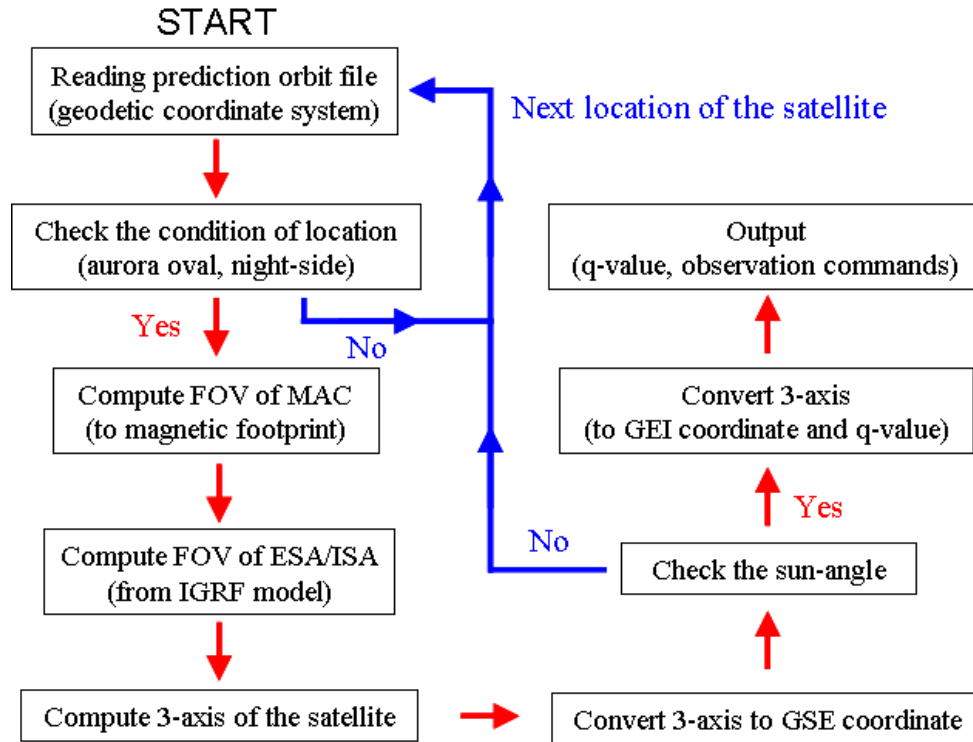


**Figure 4.2** A flowchart of computation of attitude and timing for simultaneous image and particle observation.

#### 4.1.2 Arbitrary pointing observation

The tool for other observations, with which FOV of MAC is directed to a location above any ground-based instruments for aurora observation or to stars in any position in the sky or any target on the ground for calibrating a vector of MAC's FOV, has also been developed. In this case, the tool computes 3-axis vectors of the satellite attitude for every one minute by using prediction orbit files and the pointing direction of FOV of MAC, and check if attitude of the satellite is within a certain limit. Again, the limit is determined if the sun is within 25 degrees from the normal of the solar cell, and FOV of a star tracker (STT), which is an important instrument on board Reimei for determination of the satellite attitude for aurora observation, is maintained for looking sufficient number of stars. Additionally, in case where FOV of MAC is oriented to above a ground-based instrument, this tool checks whether the distance between the

satellite and the ground-based instrument is appropriate. If a tangential line to the earth connects the satellite at 650 km altitude and a point at 110 km above the ground-based instrument, the length of the tangential line becomes about 4100 km. Therefore, if the distance between the satellite at a certain location and a location at 110 km above the ground-based instrument is greater than 4100 km, the target location is invisible from the satellite and the tool aborts computation of attitude of the satellite at such location and restarts to compute attitude of the satellite at next location. When the distance is longer than 1000 km, Mode-1 of MAC is selected. In other cases, in which the distance is shorter than 1000 km, Mode-0 of MAC is selected so that MAC observes aurora with high-temporal resolution. **Figure 4.3** shows a flowchart of this computation procedure. As like in case described in Section 4.1.1, after making observation plan by using this tool, a computer simulation for a sequence of the satellite attitude to check if the plan is safe for satellite is made. When simultaneous observation between Reimei and other instrument(s) (either ground-based one or instrument(s) on board other satellite, or both) is requested, an observation plan can be produced by using these tools and Reimei is possible to carry out such observation with flexibility responding to various requests. So far from launch of Reimei, we have succeeded in carrying out various simultaneous observations between Reimei and other instruments, for example, ALIS, EISCAT/ESR radar, SuperDARN radars, all sky cameras at Syowa and the THEMIS ground-based observatories including Athabasca, Formosat-2, and Akebono satellite.

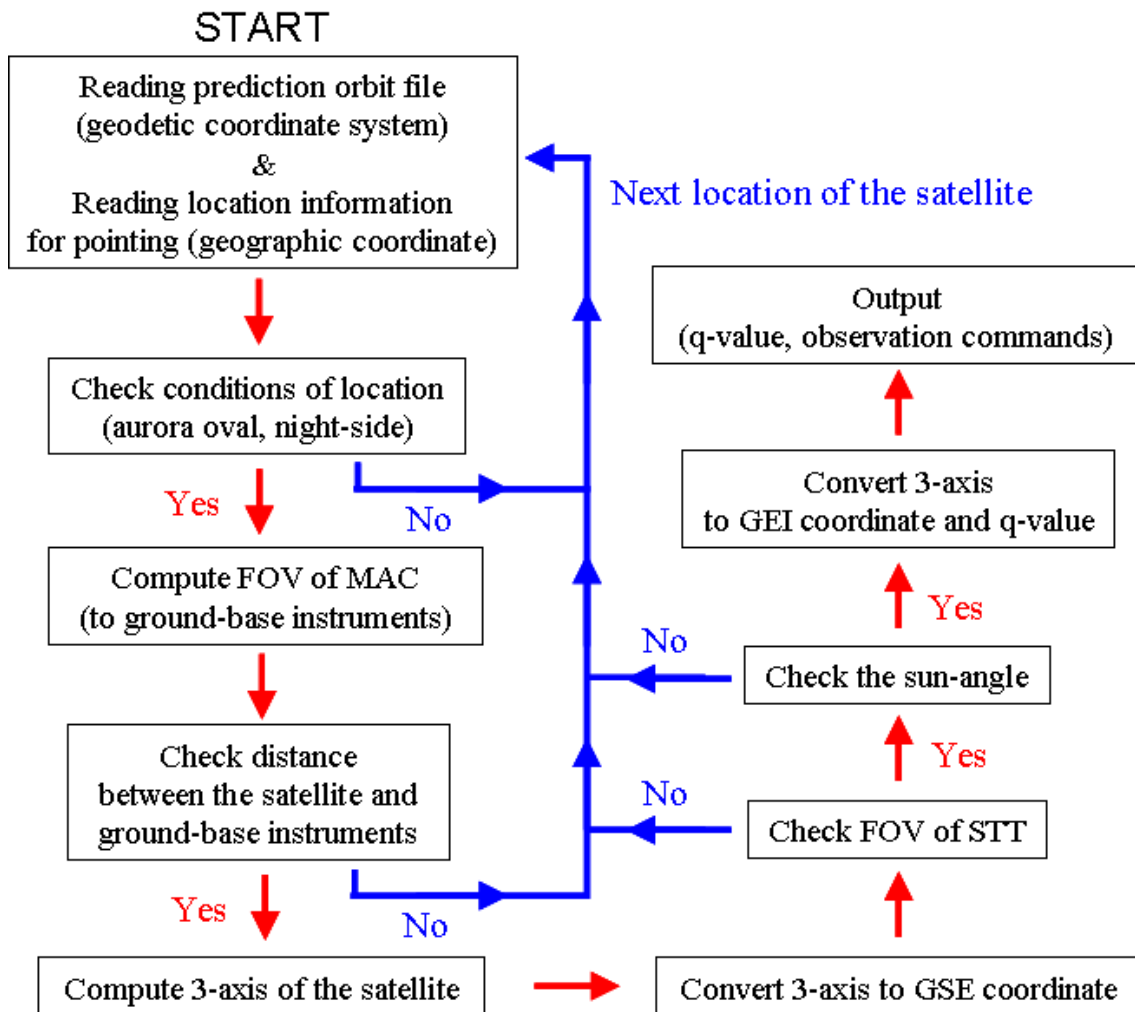


Figure 4.3 A flowchart of computation of attitude and timing for arbitrary pointing observation.

#### 4.1.3 Tracking observation

In addition to two observations described in previous subsections, Reimei is able to track its vectors to be aligned with a magnetic field line for ESA/ISA's observation for covering full pitch angles by using magnetic field sensor data with a feed back control using a reaction wheel on board Reimei for controlling attitude of the satellite. Three magnetic torquers are not used for this attitude control, because the magnetic field caused by magnetic torquers affects ESA/ISA's observations. For preparation of this observation, a tool that selects appropriate time intervals



for this observation and makes the commands of attitude control has been developed. This tool uses the prediction orbit files as input data, and it checks whether the location of a footprint of a magnetic field line threading the satellite and the satellite are in the aurora oval and not sunlit. A flow chart of this computation is shown in **Figure 4.4**. On this observation, there is a possibility that a footprint of a magnetic field line is in FOV of MAC. Tracking observation can be carried out relatively easier than simultaneous observations which is described in Section 4.1.1, because the attitude control of the satellite for this observation is relatively easier than simultaneous observations which is described in Section 4.1.1. Therefore, when the simultaneous observation that is described in Section 4.1.1 is impossible to be carried out because of unreasonable attitude control, this observation is often selected and carried out. The results of this observation have been included in the data of black aurora obtained by Reimei, which will be described in Chapter 5 and Chapter 6.

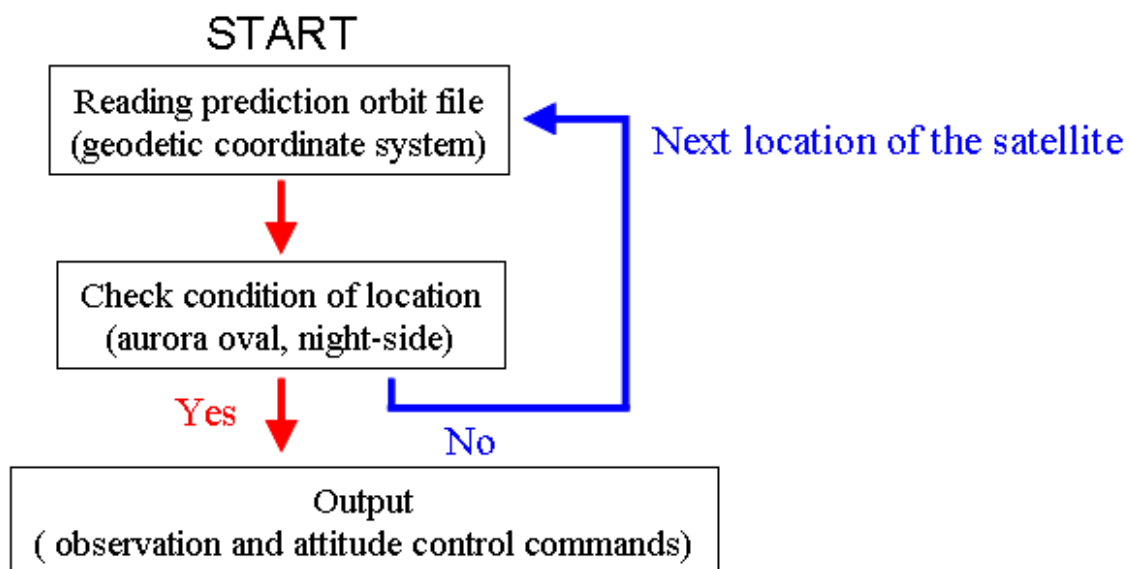


**Figure 4.4** A flowchart of computation which is used for checking time interval at which tracking observation is possible.

## 4.2 Satellite operation

In order to carry out aurora observation, commands for operation of science instruments and for attitude control of the satellite should be sent to the satellite by using telemetry in advance. In this section, methods of observation planning and the flow of operation are described.

### 4.2.1 Observation planning

Owing to 3-axis bias momentum attitude control capability, Reimei can carry out a variety of aurora observations. As stated in preceding subsections, there are three primary methods of observation. The most important observation is the simultaneous image and particle observation pointing FOV of MAC to a footprint of a magnetic field line threading the satellite, which is described in Section 4.1.1. However, if other group operating instruments (not only ground-based ones, but also those on board other satellite) requests simultaneous observation with Reimei, such simultaneous observation should have priority. In addition, if Reimei observation is carried out in the southern hemisphere, operating channels of MAC have to be limited to two channels. This is because Reimei goes into the earth shadow when it moves southward from the north polar region, and remaining usable battery power becomes low when Reimei is in the south polar region. Other important aspect of Reimei observation is that the amount of data is limited by the size of onboard memory. Therefore, we have to take into account an amount of observation data. Observation data is downlinked to the Svalbard Satellite station (Svalsat) in Norway, Syowa station in Antarctica, and JAXA/ISAS Sagami-hara campus in Japan. However, an amount of downlink data that can be received at one station is smaller than an amount of observation data obtained in observation carried out over one polar region, and the Svalsat can not necessary receive the data for all passes though Reimei is visible from there on all passes. An amount of stored commands which Reimei can store is equivalent for observations covering 2 or 3 days. Therefore, stored commands, including observation commands, have to be uplinked every 2 or 3 days. As stated above, observation planning should be flexible. Additionally, a sequence of attitude control of the satellite must be confirmed so that carrying out such attitude control sequence does never bring the satellite into a critical condition. For example, if the sun angle of solar cell becomes greater than 25 degrees, power supply will be insufficient and the satellite becomes to be impossible to be controlled. Therefore, a flow of

observation planning and checking a sequence of attitude control as shown in **Figure 4.5** was established for Reimei observation.

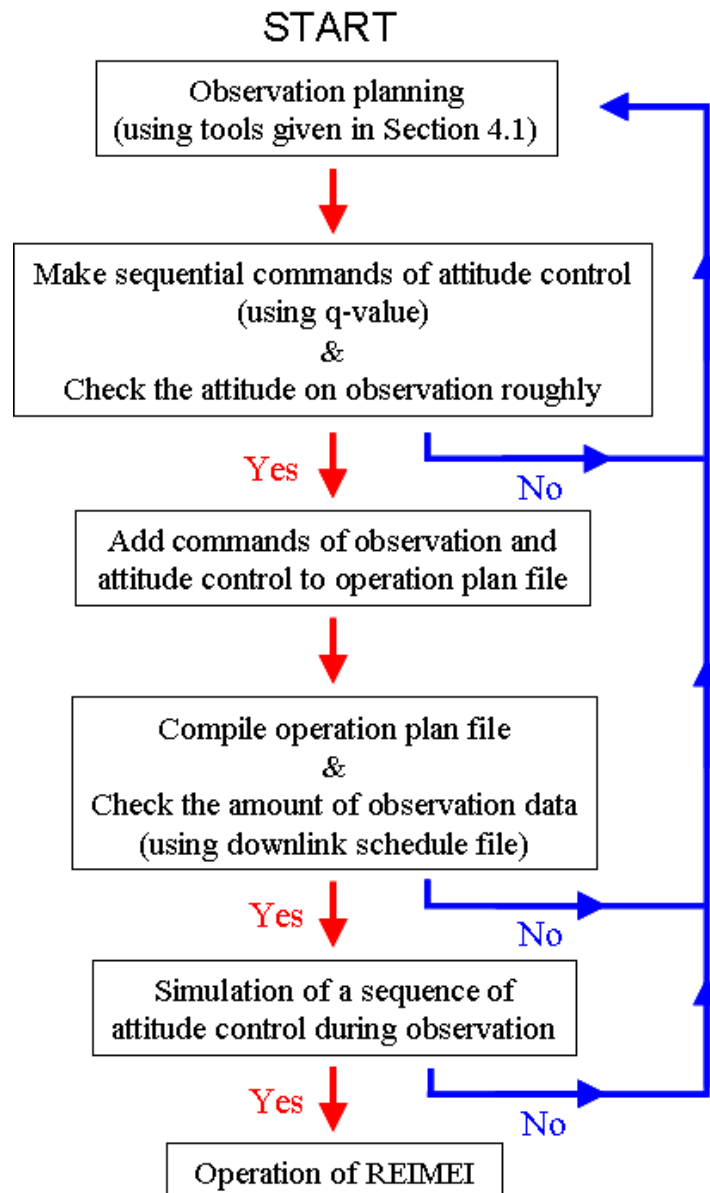


Figure 4.5 A flowchart of observation planning.

When sequential commands of attitude control are made from q-value, some parameters for attitude control are also made. These parameters are sent to Reimei separately from stored commands in operation. Simulation tools for checking a sequence of attitude control have been developed by members of engineering staffs of Reimei at ISAS. After all checks shown in **Figure 4.5** are completed, stored commands including the commands of attitude control are uplinked to Reimei in its operation at Sagamihara.

### 4.2.2 Operation method

Reimei has been being operated using a 3 m antenna at the JAXA/ISAS Sagamihara campus. **Figure 4.6** shows a picture of operation room of Reimei at Sagamihara. The uplink speed is 1 K bps, and the downlink speed is up to 131 K bps with S-band system. House keeping data and answer back of uplinked stored commands can be downlinked with a speed of 8 Kbps, being separated from observation data downlink with a speed of 131 Kbps. The operation system for Reimei, including sending commands and Quick Look (QL), has been developed by young engineers, staffs and students at ISAS and a venture company. **Figure 4.7** shows a block diagram of a ground-based station at Sagamihara. TLM-PC spools the downlink data from the satellite according to downlink bit-rate, and supplies the data to SERVER-PC. SERVER-PC supplies the data to QL-PC and CMD-PC. QL-PC displays the downlinked data, which includes status of each instrument, and is used for monitoring the condition of the satellite. CMD-PC is a unit with which an operator sends various commands to the satellite. At the same time of sending commands, CMD-PC checks out whether the commands have been sent and stored in the satellite correctly.



Figure 4.6 A picture of operation room of Reimei at Sagami-hara.

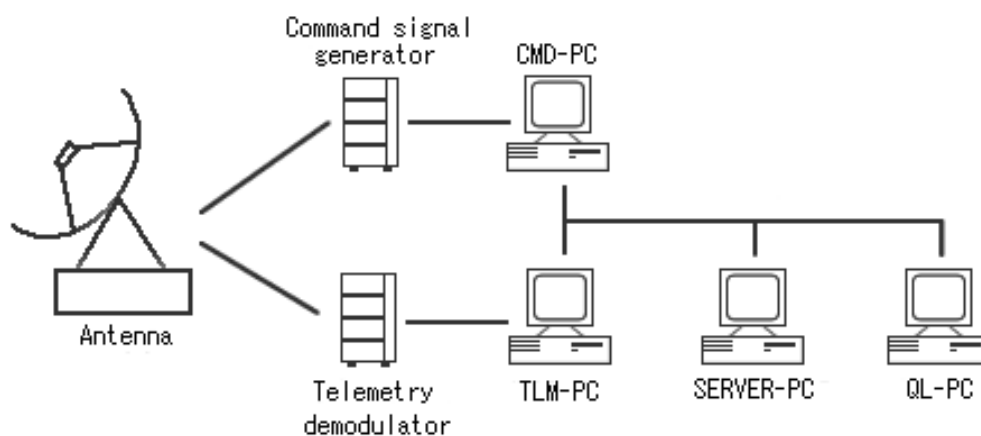


Figure 4.7 A block diagram of a ground-based station of Reimei at Sagami-hara.

As described in preceding subsections, the commands for carrying out observations and for controlling attitude of the satellite need to be uplinked to Reimei when it is visible from Sagamihara. There are four kinds of commands in order to carry out aurora observation and to downlink observation data to other stations. They are; observation stored commands for operating science instruments (described in Section 4.1 and 4.2.1), attitude control stored commands (described in Section 4.2.1), stored commands for data downlink, and stored commands for parameters of attitude control (described in Section 4.2.1). These are prepared by using a system which is described in Section 4.2.1 and above three kinds of stored commands are integrated, and finally uplinked. All commands are sent only from the Sagamihara operation room. Usually, these commands are sent to the satellite every 2 or 3 days because of the memory size for stored commands mounted on Reimei. Because of its orbit altitude of about 650 km (see Chapter 2), a visible time of Reimei at one station is short, about up to 12 minutes, and Reimei passes over Sagamihara 4 or 5 times a day. Sending commands described above for aurora observation can be uplinked on two visible passes of Reimei at Sagamihara.

Reimei can observe aurora both in the north and the south polar regions. In order to observe aurora with accurate attitude control of the satellite and to get accurate attitude data, stars which can be used for attitude determination should be in FOV of STT. Because STT refers a star map of only one hemisphere, the base attitude of the satellite needs to be reversed and a star map for reference needs to be changed from one hemisphere to the other. When the main region at which Reimei observes aurora is changed (other hemisphere is mostly sunlit), above operation for STT must be carried out.

## 4.3 Methods of data analysis

### 4.3.1 Image data process

MAC obtains image data originally with a 12bit depth, and SHU compresses the data to 8bit depth logarithmically after observation data is transferred from MAC to SHU. Accordingly, we get 8 bit data of MAC from telemetry as below;

$$SHU_{count} = \frac{\log_{10} MAC_{count} - \log_{10} OFFSET}{\log_{10} 4096 - \log_{10} OFFSET} \times 256$$

$SHU_{count}$  : data counts stored in SHU (8bit) (4.1)

$MAC_{count}$  : data counts obtained by MAC (12bit)

$OFFSET$  : offset counts for each observation mode

As described in Chapter 2, above observation data is compressed in ICU in order to downlink the data efficiently. The data is uncompressed at the ground after downlink. A flowchart of imaging data process is given in **Figure 4.8**.

After uncompressed, geographic location data to each pixel of image is added to an imaging data by using data of attitude of the satellite at a time of observation. The attitude data, which are given as q-values, are downlinked simultaneously with observation data and are converted to 3-axis elements in GEI coordinate system. Combining the attitude data, the location data of the satellite, and FOV of MAC relative to the satellite, we can compute a geographic location of each pixel of an image obtained by MAC assuming aurora emission altitude (to be 110 km). The most important aspect in this process is FOV of MAC relative to the satellite. There is a possibility that the FOV relative to the satellite may have been misaligned at the launch, therefore, the calibration of FOV of MAC was carried out after the launch by observing stars with Mode-2 of MAC. By considering FOV of STT and contamination due to scattered sunlight, '33  $\alpha$  Per' and '23  $\gamma$  Per' were selected as calibration targets of FOV (shown in **Table 4.1**). In addition, land features of the ground obtained by MAC were also used for FOV calibration. As a result, accurate FOV of MAC relative to the satellite has been performed and is utilized for calculation of a geographic location that corresponds to each pixel of an image.

By using above described data of a geographic location of each pixel and IGRF model, a

location of a magnetic footprint threading the satellite can be computed. If the footprint is in FOV of MAC, location data of the footprint is added to the data. Next, the count rate data of an image are converted into intensity data with a unit of kR by using dark image data obtained during the thermal vacuum test at various temperatures (see Section 3.1) and sensitivity calibration data as stated in Section 3.4.

After completing above process, image data obtained by MAC is plotted as an animation and/or snap shots by using a tool that has been developed at Tohoku University. Animations and snap shots of Reimei data are open for public through Internet.

(URL: <http://www.darts.isas.jaxa.jp/stp/reimei/>)

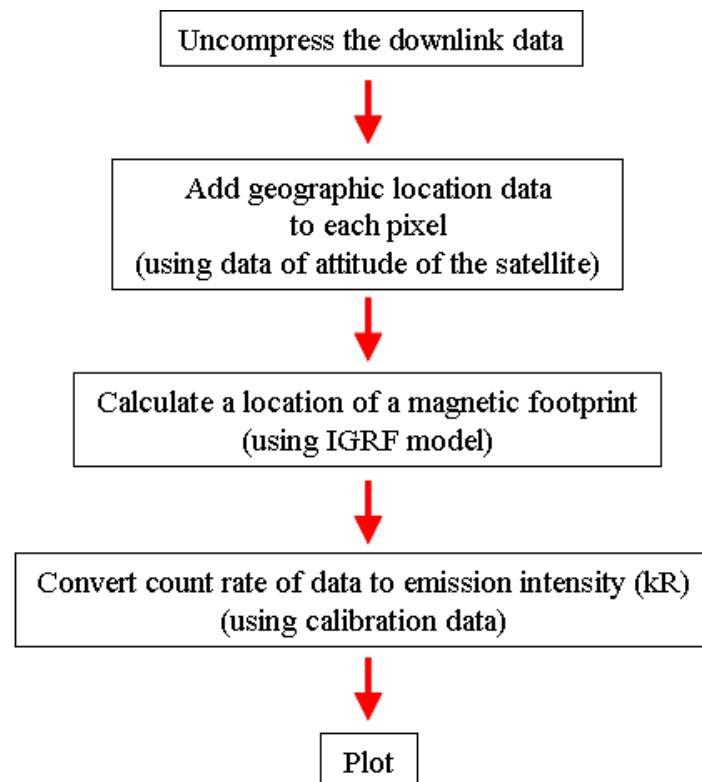


Figure 4.8 A flowchart of image data process.



**Table 4.1 Stars for calibration of FOV of MAC**

STAR ID	Magnitude	Right ascension	Celestial declination
33 $\alpha$ Per	1.79	03h24m19.38s	+49° 51'40.1"
23 $\gamma$ Per	2.91	03h04m47.79s	+53° 30'23.1"

#### 4.3.2 2D correlation analysis

In the present study, in order to determine drift speed and direction of fine scale aurora, a tool which can compute the speed and direction in observed images has been developed. Calibration data described in Section 4.3.1 is used as references for this tool. A flowchart of this computation is shown in **Figure 4.9**. Firstly, two images (image1, image2) needs to be selected from a set of image data that have been calibrated. These calibrated data include location data of each pixel, and hence, it is possible to compute velocity and moving direction of FOV of MAC that is caused by movement of the satellite. With this tool, velocity and direction are computed from positional relationship between the geographic locations (latitude and longitude) at four corners and center pixel of image1 and those of image2, and from time interval between observation time of image1 and that of image2. Next, a size of a region of interest and its position in image1 are defined as shown in the left of **Figure 4.10**. This region of interest (ROI) is named as “base-ROI”. When a ROI size is defined a little larger than an emission structure which we want to analyze, this analysis seems to give better result. In image2, “search area” needs to be defined as shown in the right of **Figure 4.10**. After doing this, standard deviation (SD) of base-ROI is computed for image1, and SDs of ROI which sits in the search area having same size as the base-ROI, is computed for image2. In case of **Figure 4.10**, the size of base-ROI is 2 x 2 pixels, and the number of ROIs that are included in the search area, having same size as base-ROI, becomes nine. Next step is to search where the emission structure included in the base-ROI drifted in image2. With this tool, by computing standard deviations (SD) of the base-ROI in image1 and SDs of ROIs included in the search area in image2, and by finding a

ROI that produced the closest SD to a SD of the base-ROI in the search area, the ROI that includes a drifted emission structure can be defined. From positional relationship between the selected ROI in image2 and the base-ROI in image1, drift velocity and moving direction of the emission structure in base-ROI can be computed. Finally, velocity of MAC's FOV due to movement of the satellite, which was determined beforehand, is subtracted from thus defined drift velocity of the emission structure. An example of this analysis is shown in **Figure 4.11**.

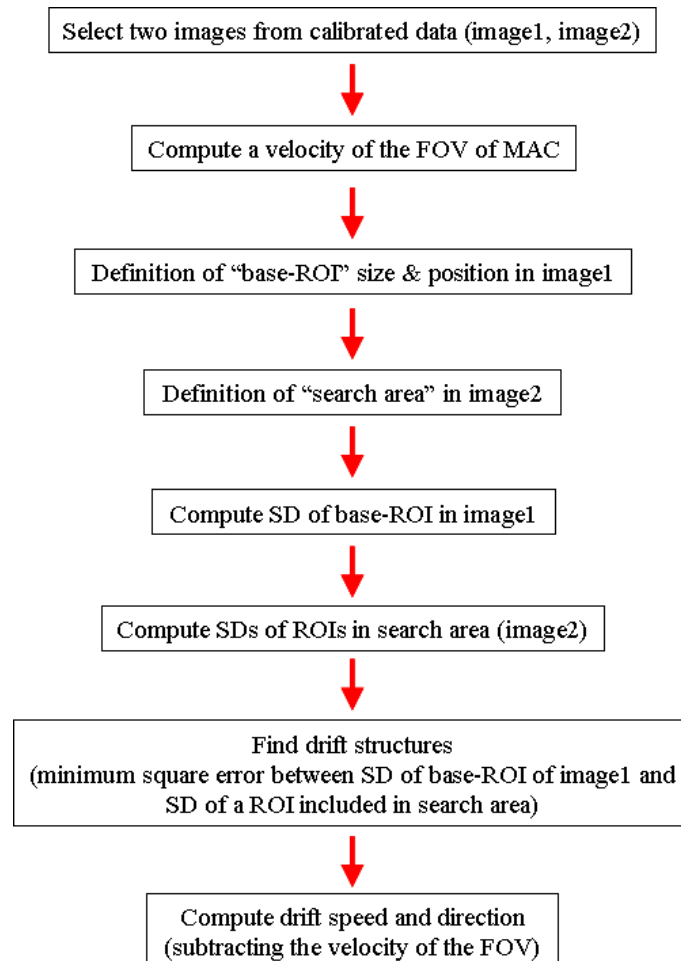


**Figure 4.9** A flowchart for computing the velocity and direction of drifting emission structures.

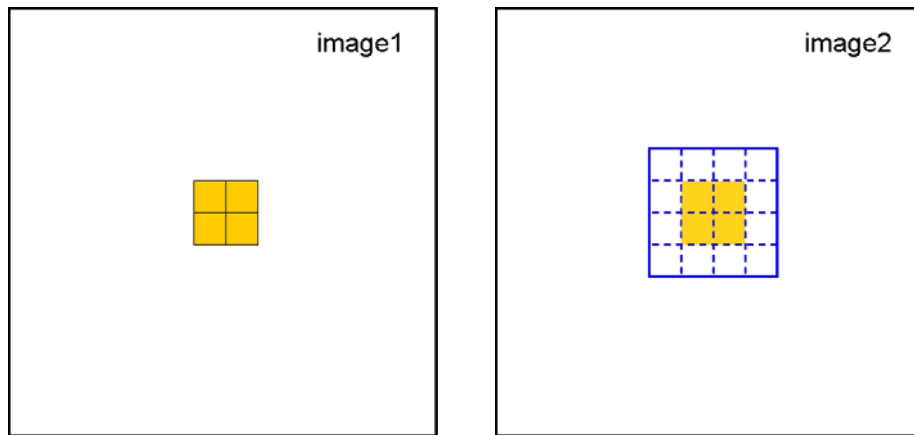


**Figure 4.10** Schematic drawing for definition of region of interest (ROI) and search area. Size and position of ROI (orange square) are defined in image1 so that it includes an emission structure of interest, as in the left figure. As an example, the size of ROI is defined as 2 x 2 pixels in this figure. Search area (blue square with solid lines) is defined in image2, as shown in the right figure, so that a size of ROI is included in it.

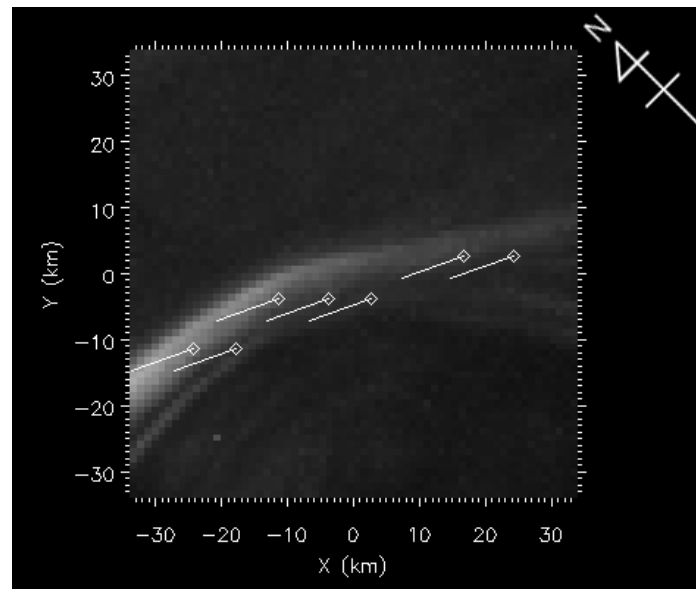


**Figure 4.11** An example of 2D correlation analysis. White lines show moving direction of the emission structure in the area denoted by white diamonds. Length of the white lines gives the velocity of drift. This is a result of analysis of the data obtained on December 22, 2005, 09:32:08 UT. In this case, all emission structures denoted by white diamonds drifted with same velocities, about 5.5 km/sec. Directions of drift are almost uniform to west-north-westward.



# Chapter 5

## Results

Since its successful launch, Reimei has been continuing simultaneous observation of the fine scale aurora by using MAC and ESA/ISA both in the north and the south-polar regions. In these simultaneous observations, black auroras have been observed number of times. This kind of satellite borne observation of black aurora, using simultaneous imaging and particle measurement with high temporal resolution, has never been realized before. In this chapter, results of these observations are presented.

### 5.1 Event selection

In order to investigate correspondence between black aurora and precipitating particles, black aurora events were selected from a large amount of Reimei observation data by defining certain criteria. Firstly, it should be a darker structure compared with surrounding auroral emission, and its spatial scale should be order of less than about 10 km in image data obtained by MAC. When the structure is arc-like with its width of order of less than about 10 km, it is defined as a black arc. When the dark structure shows a patch shape with a similar spatial scale, it is defined as a black patch. **Figure 5.1** shows an example of image that was defined as a black arc. Image shown in **Figure 5.1** was obtained when Reimei was located at geographic latitude of 60.3 degrees, geographic longitude of 260.5 degrees east in the northern hemisphere, by MAC channel-2 (557.7 nm) at 08:15:21 UT on Octo.26, 2006. Spatial extent of the image is 70 km by 70 km when auroral height is assumed to be 110km. A white square in the image denotes the location of a magnetic footprint of the satellite at the time when the image was taken. The magnetic footprint location was calculated by using attitude information of the satellite and IGRF model. Exposure time for this image is 60 msec. Green color represents OI 557.7 nm auroral emission, and the aurora appearing in this image is diffuse aurora and its intensity is about 5 ~ 6 kR. A dark structure that appears like an arc between two red arrows in the upper

part of the image was identified as a black arc. The width of the black arc is about 3 km.

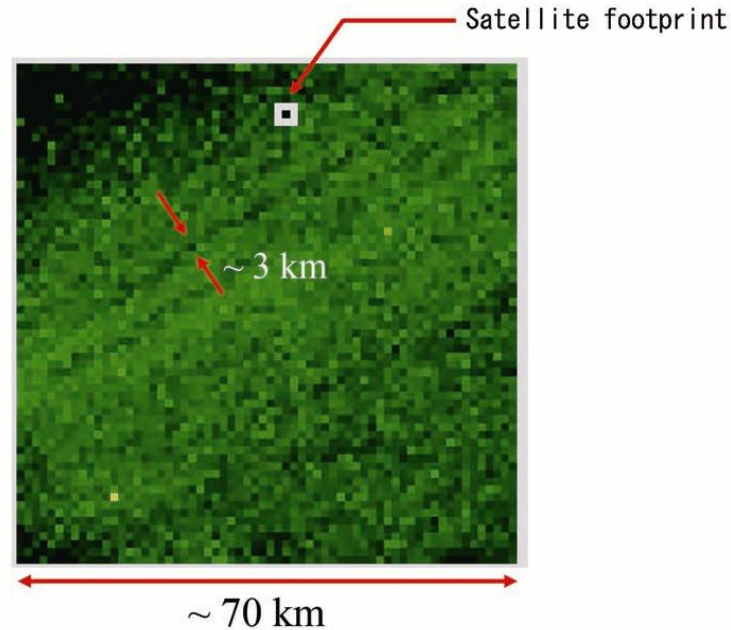


**Figure 5.1** An example image defined as black arc. It was obtained when Reimei was located at geographic latitude of 60.3 degrees, geographic longitude of 260.5 degrees east in the northern hemisphere, by MAC channel-2 (557.7 nm) at 08:15:21 UT on Octo.26, 2006. A white square in the image denotes the location of a magnetic footprint of the satellite at the time when the image was taken. The magnetic footprint location was calculated by using attitude information of the satellite and IGRF model.

Secondly, a dark structure should pass over a magnetic footprint of the satellite. If this condition is satisfied, it is possible to check image data against precipitation particle data. Energy distribution of precipitating particles associated with black aurora can be studied by checking particle data of ESA/ISA at the time when the black aurora passed over a magnetic footprint of the satellite.

**Table 5.1** shows a list of black aurora events that satisfy defined conditions in a period from

November 1, 2005 through October 31, 2006. Total number of black aurora events is 13, of which nine events are black arc events, and other four events are black patch events. On the other hand, there are black aurora events satisfying only optical condition, and their number of events is 10 within the same period. **Table 5.2** shows a list of those black aurora events defined only by optical data. Black arc was seen on all events, and black patch was seen only in one event.

**Table 5.1 A list of black aurora events for which simultaneous imaging and particle data were obtained.**

Date	Form of black aurora
2005/11/13 01:56:17 UT	Arc
2005/11/30 21:56:04 UT	Arc
2006/01/27 01:30:32 UT	Patch
2006/02/02 01:47:55 UT	Patch
2006/02/16 04:39:27 UT	Arc
2006/02/22 11:23:18 UT	Arc
2006/02/24 05:35:42-49 UT	Arc
2006/02/27 04:55:52 UT	Arc
2006/04/23 13:12:10 UT	Arc
2006/08/10 13:39:29-32 UT	Patch
2006/10/01 13:51:37 UT	Patch
2006/10/18 04:05:39-46 UT	Arc
2006/10/26 08:15:21-23 UT	Arc
Total: 13	Arc: 9, Patch: 4

**Table 5.2 A list of black aurora events defined only by optical data.**

Date	Form of black aurora
2005/11/13 22:59:53-23:00:08 UT	Arc
2005/11/22 06:29:26-34 UT	Arc
2005/12/03 00:12:27-40 UT	Arc
2005/12/03 01:49:58-01:50:23 UT	Arc
2005/12/04 11:52:35-43 UT	Arc
2005/12/09 03:45:28-53 UT	Arc and Patch
2005/12/10 21:54:03-18 UT	Arc
2005/12/21 01:05:10 UT	Arc
2005/12/25 02:21:33-45 UT	Arc
2006/08/01 12:26:55-12:27:01 UT	Arc
Total: 10	Arc: 10 Patch: 1

## 5.2 Black arc and black patch events

As mentioned in the preceding section, 13 events of black aurora obtained by simultaneous imaging and particle observation were identified. Nine events among them are black arc events. In this section, some examples of black arc data are shown.

### 5.2.1 Image and particle data; an example of black arc event

An example of successive image data of black arc event obtained by MAC on October 26, 2006 is shown in **Figure 5.2**. In the figure, the upper column shows successive images obtained by channel 1 (427.8 nm emission) and the middle column shows those obtained by channel 2 (557.7 nm emission), and lower column shows those obtained by channel 3 (670.0 nm emission). In the image data, north is up and west is left. Image data of each channel are arranged in temporal order from left to right. Though MAC obtained these image data every 120 ms for this



event, images every 360 ms are shown in this figure. Because Reimei passed over the night-side of the northern hemisphere from north to south, FOV of MAC moved from north to south. Therefore, structures in the image move from bottom to top. FOV of each image is approximately 70 km square. The color density in each channel is logarithmically proportional to emission intensity observed by MAC. Color bars are given at top right of the figure. A white square in each image shows a location of a magnetic footprint of the satellite which was derived from attitude data of the satellite at the time of observation and IGRF model. Because the direction of FOV for each channel differs slightly each other, a pixel position of the footprint is not the same in each channel. FOV of each channel was calibrated by using image data of stars obtained on Mode-2 of MAC and attitude data of the satellite after launch [Ino, 2006].

This event was observed in the northern hemisphere at approximate invariant latitude of 69.9 ~ 70.1 degrees north and longitude of 260.4 ~ 260.5 degrees east at 08:15:21 ~ 08:15:25 UT. AE index at this time is approximately 100 nT indicating that magnetic activity is quiet. **Figure 5.2** shows only image data obtained from 08:15:21 to 08:15:25 UT. In images of channel 2 and the channel 3, diffuse aurora whose intensity is about 5 kR is seen. Some dark structures of arc form in diffuse aurora are seen in the slightly upper side from the center of an image and lie from top right to bottom left. These dark structures are identified as black arcs, which have a width of approximately 3 to 5 km. In channel 1 images, intensity of diffuse aurora is weak, about 2 kR, and dark structures are not seen clearly. Between 08:15:22.5 and 08:15:23.7 UT, a magnetic footprint of the satellite passed over five black arcs in channel 2 images. **Figure 5.3** shows an intensity profile along a magnetic footprint path for the channel 2 images. It is seen in **Figure 5.3** that intensity of OI 557.7 nm in black arcs, about 3 kR, is relatively weak compared to surrounding diffuse aurora.

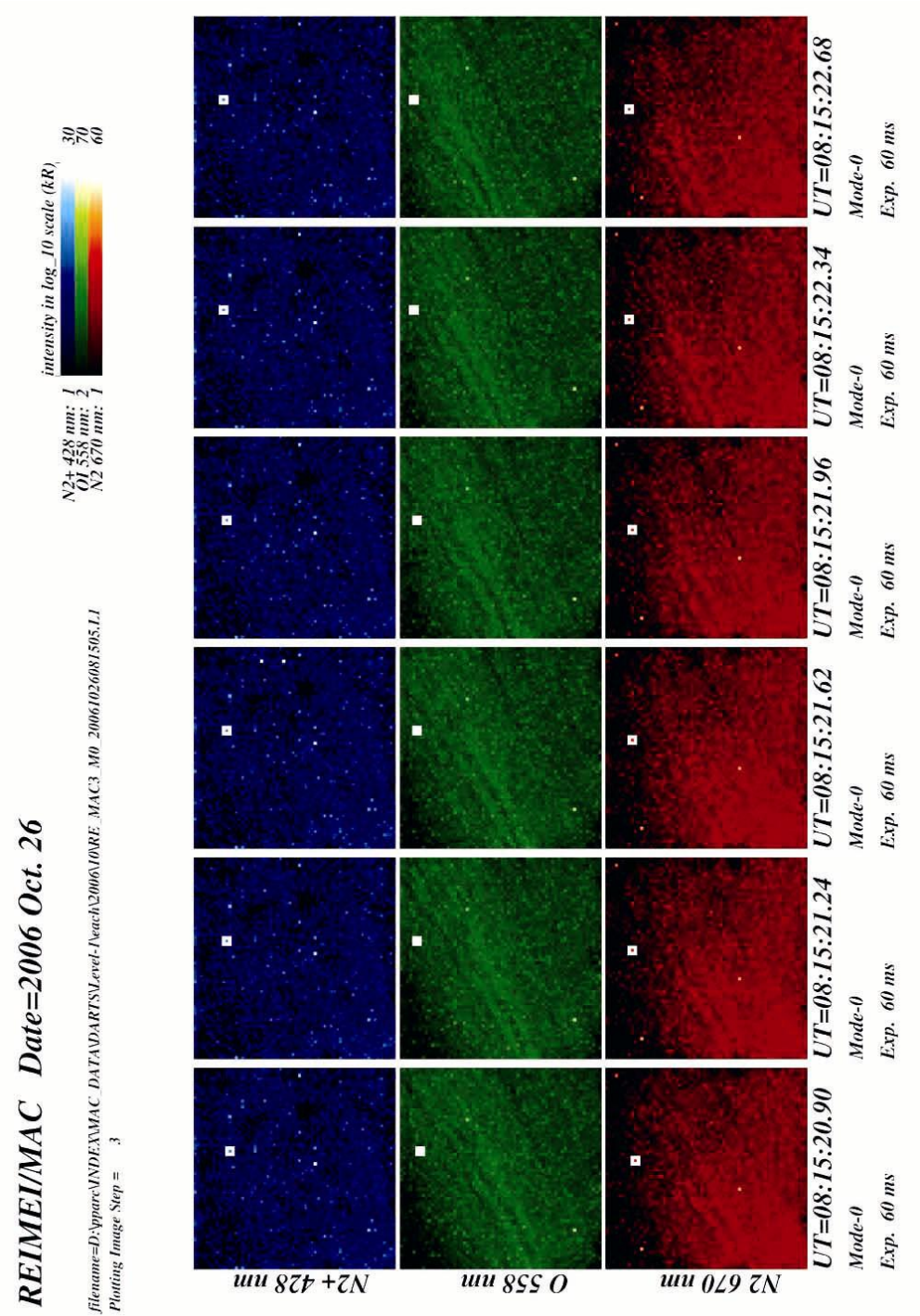
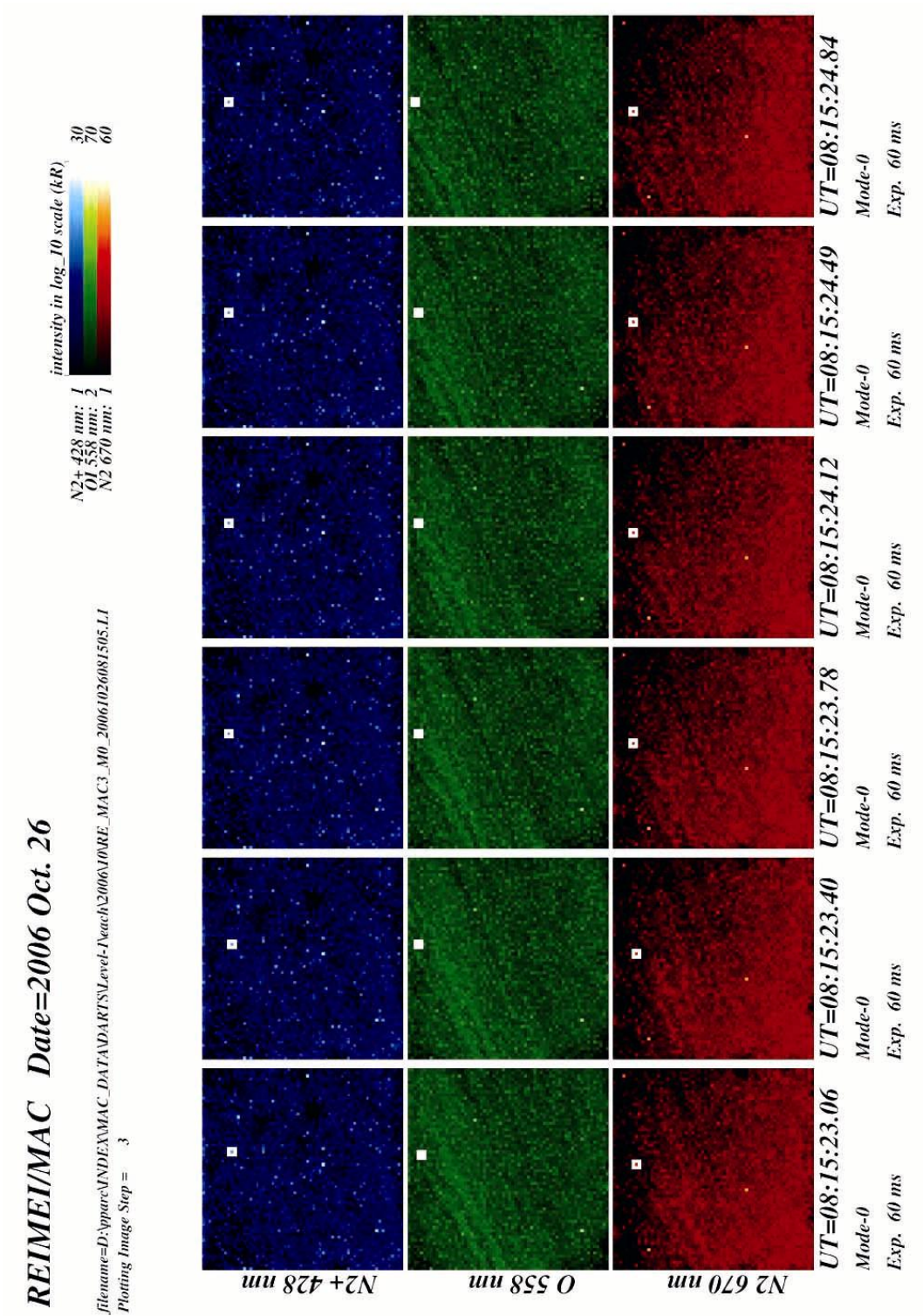
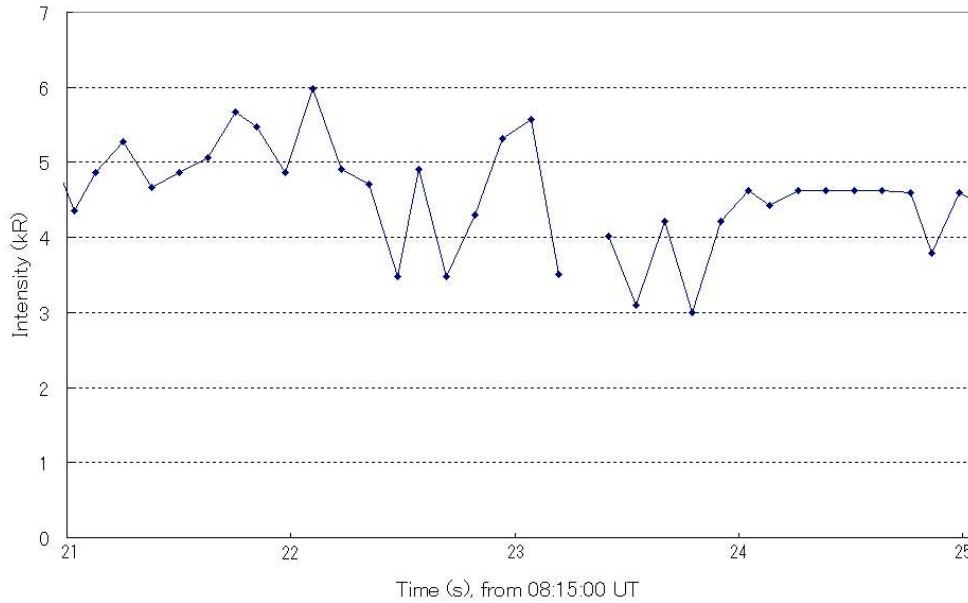


Figure 5.2 Image data of black arc event obtained by MAC. This event was on October 26, 2006. A white square in each image shows a location of magnetic footprint of the satellite. The magnetic footprint passed over five black arcs between 08:15:22.5 and 08:15:23.7 UT (to be continued in next page).





**Figure 5.3** Intensity profile along a magnetic footprint path for channel 2 images in Figure 5.2. At 08:15:22.5, 08:15:22.8, 08:15:23.2, 08:15:23.5, and 08:15:23.7 UT, magnetic footprint of the satellite passed over a black arc. Emission intensity of black arcs is about 3 kR. It is suggested that black arc is a darker structure compared to surrounding diffuse aurora.

As for characteristics of precipitating electrons associated with the black arcs, **Figure 5.4** shows an Energy versus Time diagram (E-T diagram) of particle observation data which were obtained by ESA/ISA covering the same time period. Time coverage of this data is from 08:15:12 UT to 08:15:42 UT on October 26, 2006. In the figure, vertical axis of each panel indicates energy (eV) logarithmically from 10 eV to 12 keV. Color scale in each panel shows differential energy flux observed by ESA/ISA. Upper three panels show E-T diagram of electrons for three different pitch angle ranges, and bottom three panels show those for ions. A top one of each three panels is an E-T diagram of downward particles, middle one is that of particles perpendicular to a magnetic field line, and bottom one is that for upgoing particles. It is seen in the topmost panel, which is downward electron E-T diagram, that electrons with energies greater than 1 keV are continuously precipitating starting at around 08:15:18 UT until the end of observation. The precipitation does not have a shape of inverted-V structure, and it



seems to be precipitating by pitch angle scattering [e.g. *Johnstone et al.*, 1993; *Villalón and Burke*, 1995]. In addition to this continuous precipitation, an inverted-V structure having a peak energy of 2 keV is seen between 08:15:17 UT and 08:15:29 UT overlapping with the precipitations that seem to be caused by pitch angle scattering. However, this inverted-V structure does not seem to contribute to auroral emission in this time period because its energy is not so high. In the downward ion E-T diagram, characteristics of ion originated in the central plasma sheet [e.g. *Hirahara et al.*, 1997], which has energy dispersion, is seen starting at 08:15:35 UT. Both behaviors of electron and ion shown in **Figure 5.4** suggest that the particles, except for electrons with an inverted-V structure, were coming from the central plasma sheet.

**Figure 5.5** shows E-T diagrams focused on a period when black arcs appeared. Each panel in **Figure 5.5** has same meaning as in **Figure 5.4**. In the topmost panel, which shows downward electrons flux, it is seen that there is local deficiencies in the electron flux with energies greater than 3 keV, clearly corresponding at times when a magnetic footprint of the satellite passed over black arcs (08:15:22.5, 08:15:22.8, 08:15:23.2, 08:15:23.5, and 08:15:23.7 UT). On the other hand, electron flux with energies less than 3 keV does not show such deficiencies. This fact suggests that black arcs in this event are due to the lack of downward electron flux for energies greater than 3 keV. On the other hand, ion flux does not show any particular change during this time period.

In order to investigate the behavior of electron precipitation associated with black arc, differential number fluxes of electrons for the times when a magnetic footprint of the satellite passed over black arcs were computed. They are shown in **Figure 5.6**. Calculated number flux is an average of the values for three pitch angles, 0 deg, +10 deg, and -10 deg, and it was defined as the downward electrons. Panel (a) to panel (e) in this figure is arranged in order of time. Furthermore, differential number flux of precipitating electrons for surrounding diffuse aurora is also shown in each panel to compare with that for black arc. Blue dots and lines show the values for black arcs, and pink ones are for surrounding diffuse aurora. A peak flux seen at around 2 keV is caused by an inverted-V structure, which is seen in **Figure 5.4** and **Figure 5.5**. As seen in common in these panels, differential number flux for black arcs with energies greater than 3 keV decreases quite rapidly compared to that for surrounding diffuse aurora. On the other hand, differential number flux for black arcs in the energy range less than 3 keV shows no change to that for surrounding diffuse aurora. This fact suggests that the local loss of electron flux corresponding to black arcs is not caused by potential structure such as a divergent electric field.

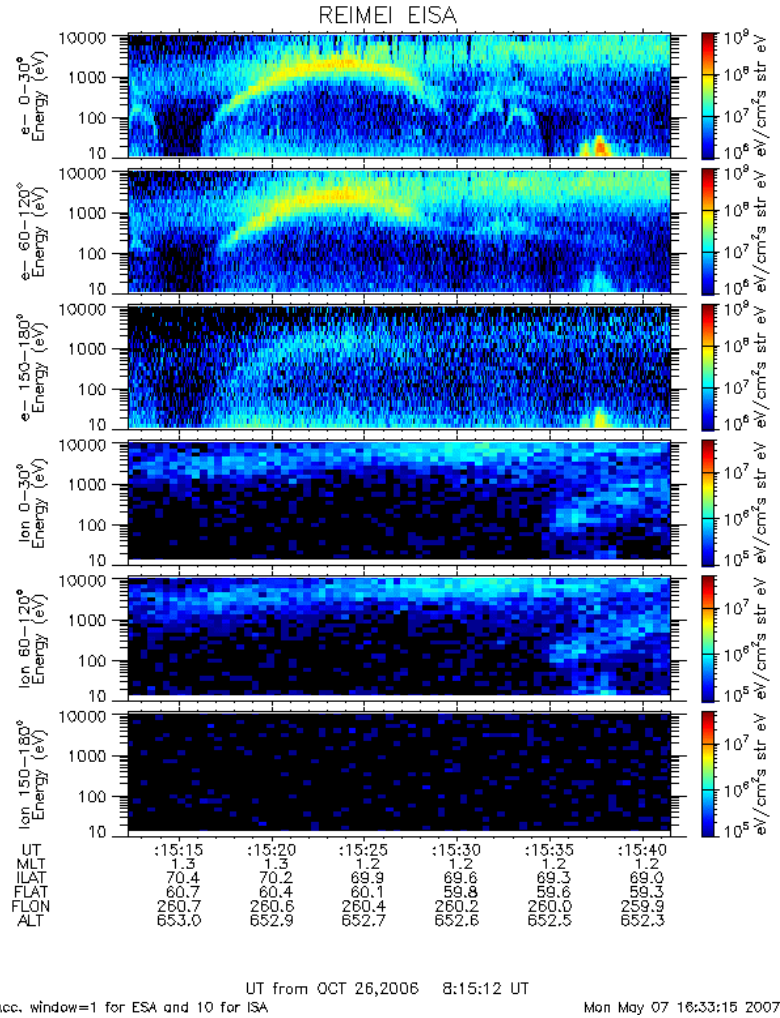
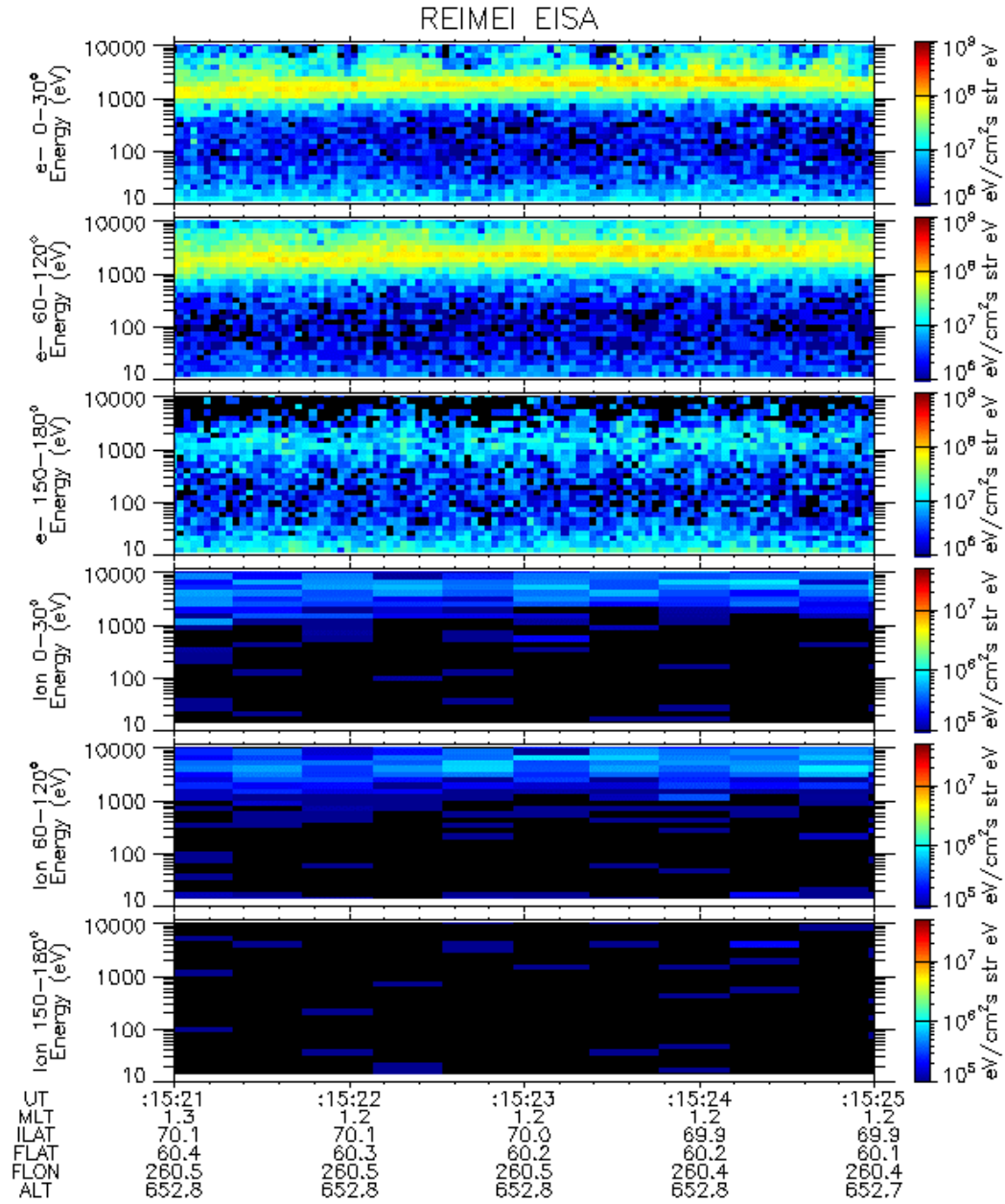


**Figure 5.4** Energy versus Time diagrams (E-T diagrams) based on particle observation data, which was obtained by ESA/ISA for a period of 08:15:12 UT to 08:15:42 UT on October 26, 2006. Vertical axis of each panel indicates energy (eV) logarithmically from 10 eV to 12 keV. Color scale in each panel shows differential energy flux observed by ESA/ISA. Upper three panels show E-T diagram of electrons for three different pitch angle ranges, and bottom three panels show those for ions. A top one of each three panels is an E-T diagram of downward particles, middle one is that of particles perpendicular to a magnetic field line, and bottom is that for upward particles. In the downward electron E-T diagram, continuous precipitation with energies greater than 1 keV, starting at around 08:15:18 UT until the end of observation, seems to be caused by pitch angle scattering. In addition to this continuous precipitation, an inverted-V structure, which has a peak energy of 2 keV, appears between 08:15:17 UT and 08:15:29 UT, and is partially-overlapping with the precipitations caused by pitch angle scattering.



UT from OCT 26,2006 8:15:21 UT  
Acc. window=1 for ESA and 10 for ISA

Sat Dec 08 00:28:38 2007

**Figure 5.5** E-T diagrams focused on a period when black arcs appeared. A magnetic footprint of the satellite passed over black arcs at 08:15:22.5, 08:15:22.8, 08:15:23.2, 08:15:23.5, and 08:15:23.7 UT. It is seen that the flux of downward electrons with energies greater than 3 keV is locally deficient at those times (topmost panel).

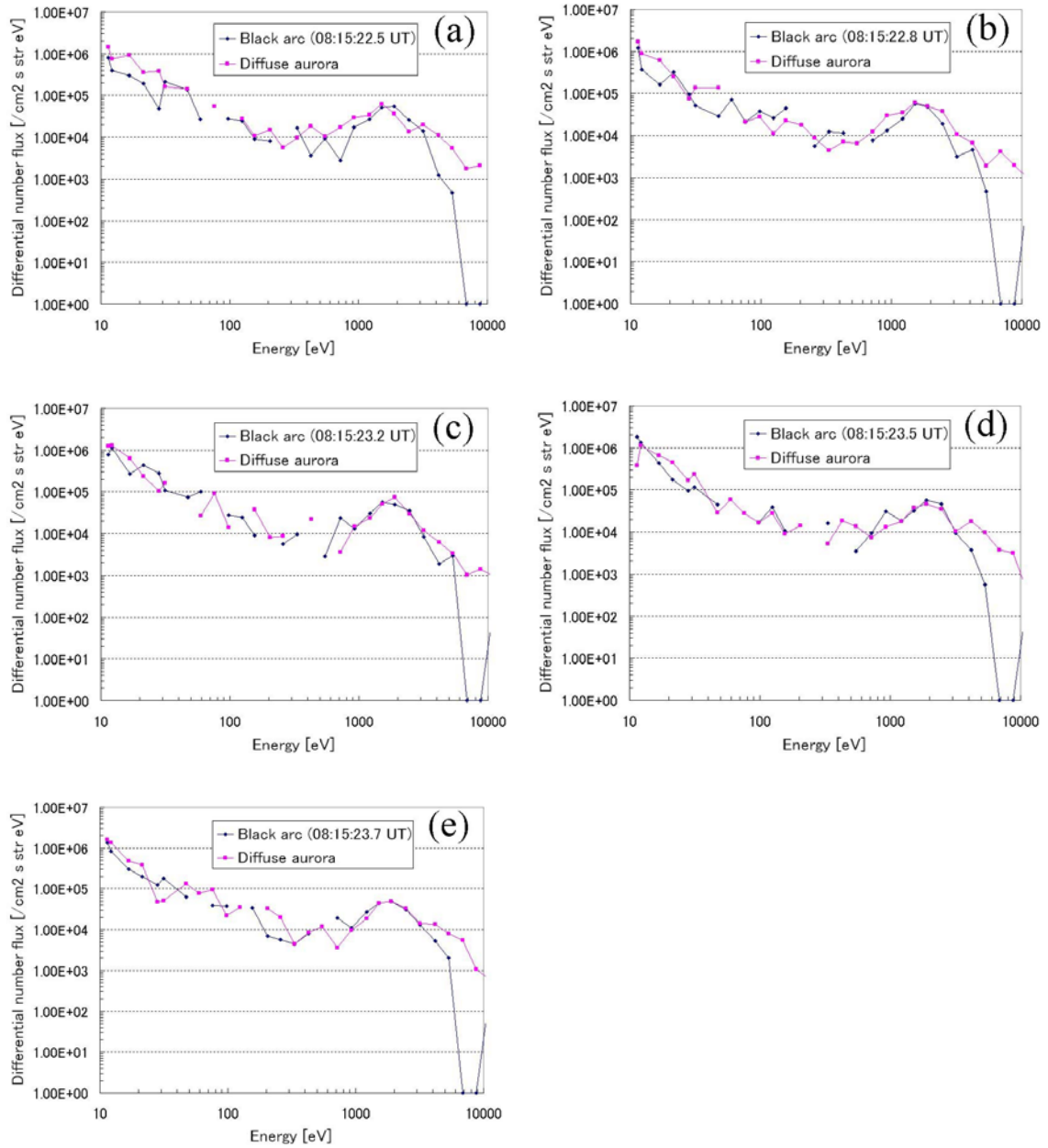


**Figure 5.6** Electron differential number flux versus energy for the times when a magnetic footprint of the satellite passed over black arcs. Panel (a) shows a differential number flux for first black arc (08:15:22.5 UT), panel (b) shows that for second one (08:15:22.8 UT), panel (c) shows that for third one (08:15:23.2 UT), panel (d) shows that for fourth one (08:15:23.5 UT), and panel (e) shows that for fifth one (08:15:23.7 UT). In each panel, differential number flux for surrounding diffuse aurora is also shown to compare with that for black arc.



### 5.2.2 Statistical characteristics of black arc and black patch obtained by Reimei

Statistical characteristics of black arc and black patch obtained by Reimei are summarized as follows. Firstly, characteristics based on image data obtained by MAC are given. The characteristics include not only the analysis results of simultaneous observation events (13 events), but also those obtained by imaging observation only (10 events). Nineteen events out of all events were observed in the northern hemisphere, and the others were observed in the southern hemisphere. Statistics were made separately for the northern hemisphere and for the southern hemisphere.

Emission intensities of black arc and black patch are rather faint in the order of 2 ~ 4 kR. The intensities are not different between the northern hemisphere and the southern hemisphere. The width of black arc is from 3 ~ 10 km. The scale of black patch is about 3 ~ 5 km. The width is not different between the northern and the southern hemisphere, too. As for the invariant latitudes in which black arc and black patch appear, the distribution in the northern hemisphere is shown in **Figure 5.7**. From this figure, it is seen that black arc and black patch appear favorably in the invariant latitude range of 66 ~ 68 degrees. In the past studies of black aurora [e.g. *Trondsen and Cogger*, 1997; *Kimball and Hallinan*, 1998; *Peticolas et al.*, 2002], it is reported that they appear in the invariant latitude of 65 ~ 68 degrees, and this is consistent with our result. On the other hand, **Figure 5.7** shows that black arc and black patch appear also in the invariant latitudes greater than 70 degrees. Observations in the past studies are based on ground-based optics or airborne ones, in contrast to our observation from a polar orbiting satellite. Because coverage area of our observation is quite large compared to the past observations, our results on latitudinal distribution of black arcs and black patches seem to be reliable. Regarding a relation between the magnetic activity and the appearance of black arc and black patch, 11 events out of 19 events (the northern hemisphere events) were observed in magnetic quiet periods. Other events were observed in a variety of conditions. In the southern hemisphere, black arcs and black patches were observed in magnetic quiet periods or in the recovery phase of an auroral substorm. *Trondsen and Cogger* [1997] reported that black auroras appear to be a common feature of the late recovery phase of an auroral substorm. In Reimei observations, any strong relation between the magnetic activity and the appearance of black arc and black patch was not clearly seen. In addition, relation between the magnetic activity and the invariant latitude where black arc and black patch appear was not seen, too. It can be said that black arc

and black patch tend to appear in the invariant latitude range of around 68 degrees regardless of the magnetic activity. However, it should be noted that the result in this study is based on AE index for the magnetic activity, and that the result in the past study is based on the data of all-sky imager for a long time period. A period of Reimei observation for one event is only several minutes, therefore, exact condition of aurora around the time when black arc or black patch appears is difficult to define. Past observations reported that black arc and black patch were sometimes associated with pulsating aurora [Trondsen and Cogger, 1997; Kimball and Hallinan, 1998]. In Reimei observation, pulsating aurora has been sometimes observed simultaneously with black arc or black patch. Eight events out of 23 events, which include events obtained only by optics, are associated with pulsating aurora, and 3 events among those 8 events are also observed by ESA/ISA simultaneously. **Table 5.3** is an event list of black arc and black patch associated with pulsating aurora. When pulsating aurora appears with black arc or black patch, pulsating aurora is always located in the equatorward of black arc or black patch.

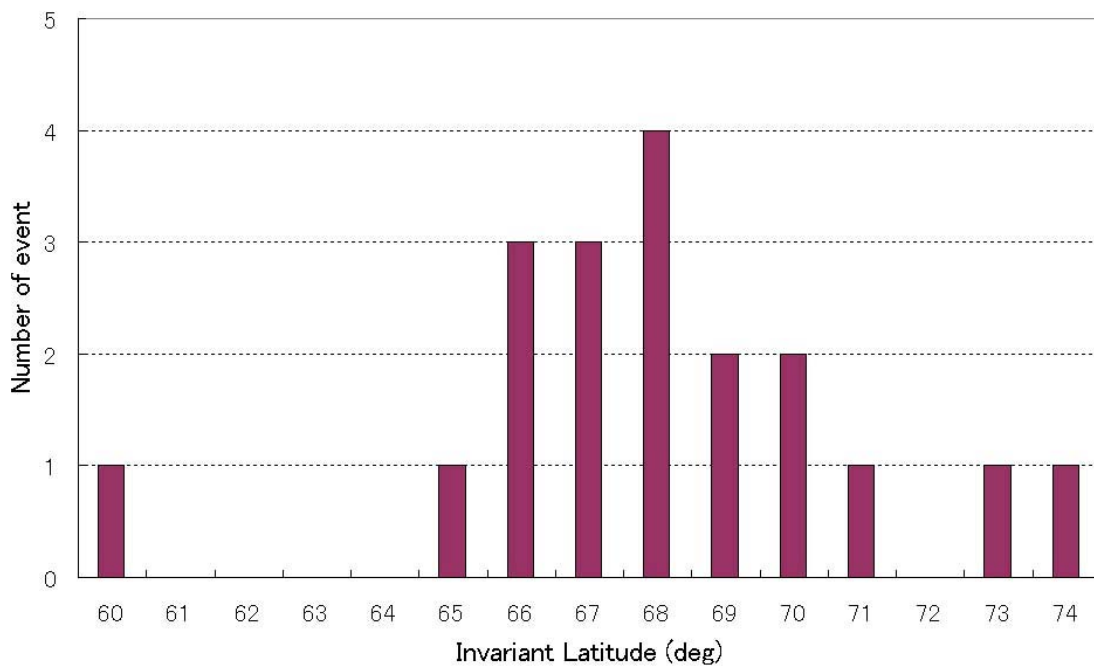


**Figure 5.7** Distribution of black arc and black patch appearance in the invariant latitude.

**Table 5.3 Event list of black arc and black patch associated with pulsating aurora. The list includes events obtained only by MAC.**

Date	Particle data for pulsating aurora
2005/11/13 01:56:17 UT	Yes
2005/11/13 22:59:53 – 23:00:08 UT	No
2005/12/03 00:12:27 – 00:12:40 UT	No
2005/12/03 01:49:58 – 01:50:23 UT	No
2005/12/10 21:54:03 – 21:54:18 UT	No
2006/01/27 01:30:32 UT	Yes
2006/02/27 04:55:52 UT	Yes
2006/10/01 13:51:37 UT	For only black patches

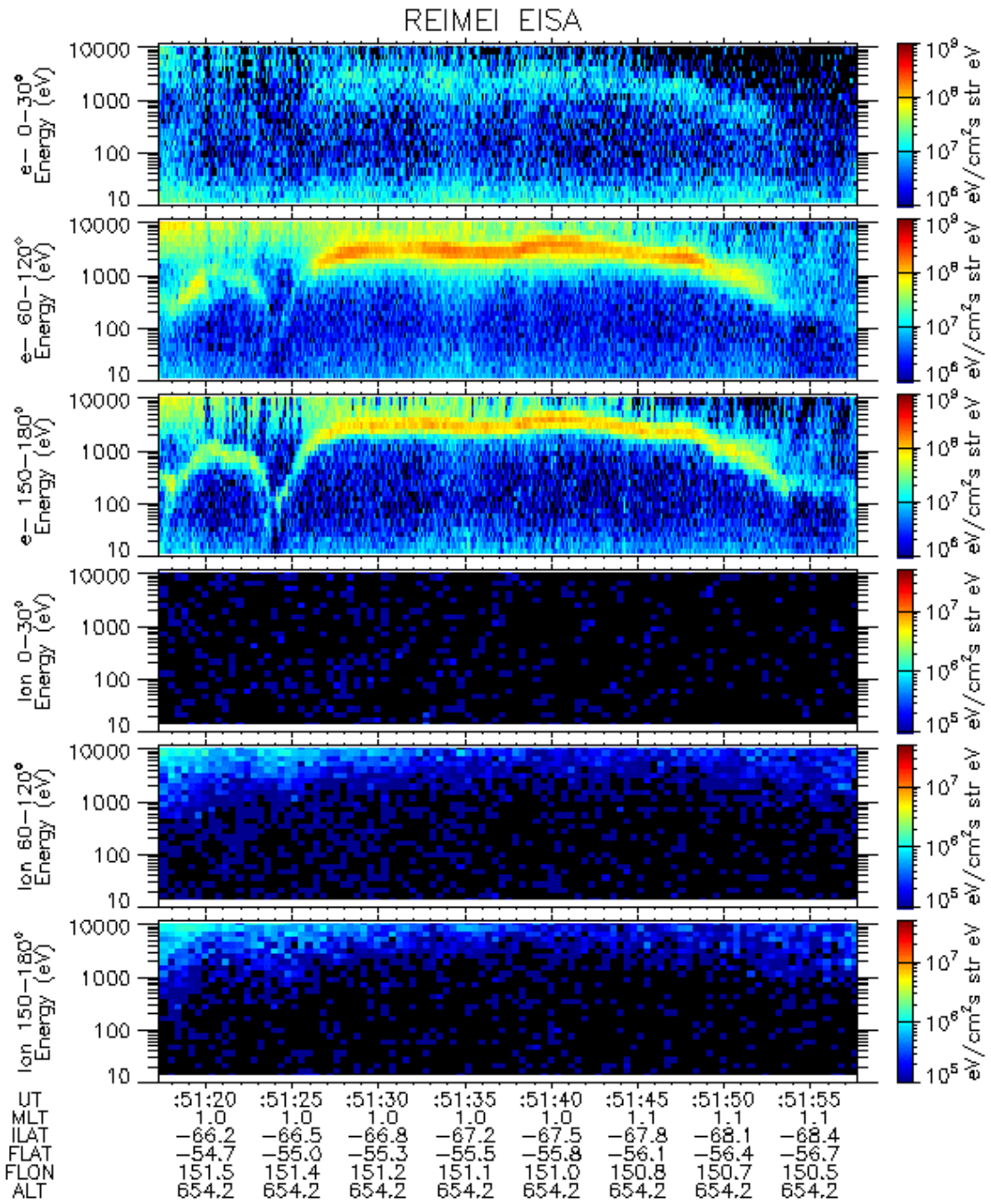
Next, the characteristics of black arc or black patch based on particle data obtained by ESA/ISA are given. They are based on 10 events obtained by simultaneous image and particle observation.

As stated in the preceding section, behaviors of precipitating electrons and ions that correspond to all black arc or black patch events obtained by Reimei showed characteristics of particles coming from the central plasma sheet. Accordingly, black arc or black patch appears in the region connected the central plasma sheet. Precipitating electron flux with energies greater than 2 ~ 7 keV has a local deficiency at the time when a magnetic footprint of the satellite passed over a black arc or black patch (for example; see **Figure 5.5**). In addition, an inverted-V structure with a peak energy of 2 ~ 5 keV is often seen in the downward electron E-T diagram. Six events out of 13 black arc or black patch events are associated with such inverted-V structures. They overlap electron precipitations contributing for diffuse aurora. Because of their

weak peak energy, precipitations accelerated by inverted-V structure do not seem to contribute strongly to aurora emissions in the image data obtained by MAC. **Table 5.4** is an event list of black arc or black patch with which inverted-V structure is associated. In case of an event on October 1, 2006, the inverted-V structure has three peaks. E-T diagram for this event is shown in **Figure 5.8**. Three peaks are seen at around 13:51:33 UT, 13:51:40 UT, and 13:51:47 UT. It is noted that this event was observed in the southern hemisphere. Therefore, diagrams for pitch angles of 150 – 180 degrees correspond to downward flux. Details of this event will be described in Section 5.3.1. In terms of relation between black arc or black patch and pulsating aurora, which is collocated in the equatorward of the black aurora, an E-T diagram is shown in **Figure 5.9**. This event was observed on November 13, 2005. A magnetic footprint of the satellite passed over black arcs at 01:56:17 UT and 01:56:34 UT, and pulsating aurora starting at 01:56:40 UT to the end of this figure was confirmed in the corresponding image data (not shown). At 01:56:44 UT and 01:56:58 UT, a magnetic footprint passed over right outside of pulsating patch. In pulsating aurora, apparent energy-dispersions are seen in precipitating electron flux at 01:56:44 UT and 01:56:58 UT. On the other hand, electron flux for black arc does not show any energy-dispersion.

**Table 5.4 Event list of black arc or black patch with which inverted-V structure was associated.**

Date	Peak energy of inverted-V
2006/01/27 01:30:32 UT	2 keV
2006/02/22 11:23:18 UT	3 keV
2006/02/24 05:35:42-49 UT	4 keV
2006/10/01 13:51:37 UT	3, 4, 5 keV
2006/10/18 04:05:39-46 UT	3 keV
2006/10/26 08:15:21-23 UT	3 keV

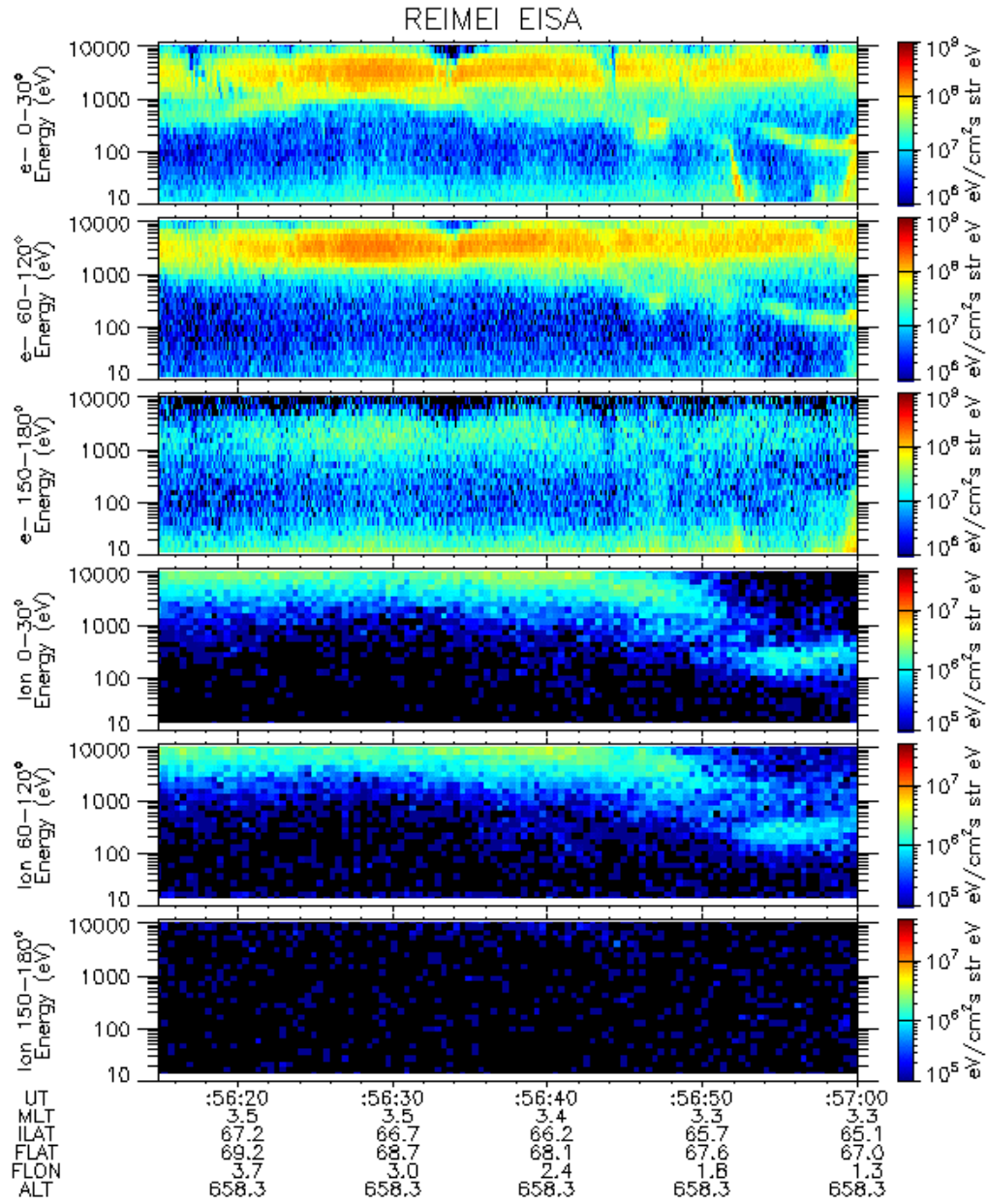


UT from OCT 1, 2006 13:51:17 UT

Acc. window=1 for ESA and 10 for ISA

Mon May 07 17:46:37 2007

**Figure 5.8** E-T diagrams for the black patch event on October 1, 2006. This event was observed in the southern hemisphere. Therefore, diagrams for pitch angles of 150 – 180 degrees correspond to downward flux.



UT from NOV 13, 2005 1:56:14 UT  
Acc. window=1 for ESA and 10 for ISA

Mon Dec 10 16:01:45 2007

**Figure 5.9** E-T diagram for the black arc event associated with pulsating aurora. This event was observed on November 13, 2005. Black arc events are at 01:56:17 UT and 01:56:34 UT, and pulsating aurora events are from 01:56:40 UT to the end of the figure. At 01:56:44 UT and 01:56:58 UT, a magnetic footprint of the satellite passed over right outside of a pulsating patch.

### 5.3 Drifting black patch event

Among black aurora events described earlier, two events of drifting black patch were identified. In this section, characteristics of these drifting black patch events are given.

#### 5.3.1 Image and particle data

Drifting black patches were observed on January 27, 2006 and October 1, 2006. Their image data are shown in **Figure 5.10** and **Figure 5.11**. The format of figure is same to that of **Figure 5.2**. In **Figure 5.10**, diffuse aurora with intensity of about 6 kR is seen (OI 557.7 nm emission). In the N<sub>2</sub> 1PG 670.0 nm images, intensity is as low as about 3 kR or less. In the N<sub>2</sub><sup>+</sup> 1NG 427.8 nm images, nothing is seen because of weak intensity of less than 1 kR. A segment of black arc and black patch are seen at the bottom left and the center in the OI 557.7 nm images. The black arc segment is also faintly seen in the N<sub>2</sub> 1PG 670.0 nm images. At around 01:30:31.9 UT, a magnetic footprint of the satellite passed over a black patch. The event was observed in the northern hemisphere, therefore, the FOV of MAC moved from north to south as time goes by. In other words, a structure fixed relative to the earth should move from bottom to top in the images. However, the black patch moves in a direction different from that expected from orbital motion of the satellite (from bottom to top in the images). The apparent moving direction is to the left-upward, and taking movement of the satellite into consideration, it was found that the black patch is drifting westward (see **Figure 5.12**). **Figure 5.12** shows an image of the event mapped on the geographic coordinate. From **Figure 5.12**, it is seen that the black patch drifted westward. In **Figure 5.11**, diffuse aurora with an intensity of about 8 kR is seen (557.7 nm emission). A lot of black patches are seen in this event (557.7 nm emission). The black patches have two directions of drift, which are from bottom right to top left (nearly eastward, see **Figure 5.12**) and from top left to bottom right (nearly westward, see **Figure 5.12**). Black patches drifting nearly eastward are located in the upper half of the images, and those drifting nearly westward are located in the lower half of the images. It may be difficult to see the drift movements stated above. However, though it cannot be shown here, a moving picture of these events would show these drifting movements more clearly. At around 13:51:37 UT, a magnetic footprint of the satellite passed over a black patch. *Trondsen and Cogger [1997]* reported that black patch and black arc segment drifted only eastward around midnight. Reimei's observation has been carried



out also around midnight, therefore, drifting direction of black patch described in this section seems to be different from the past work. The detail will be further discussed in Chapter 6.

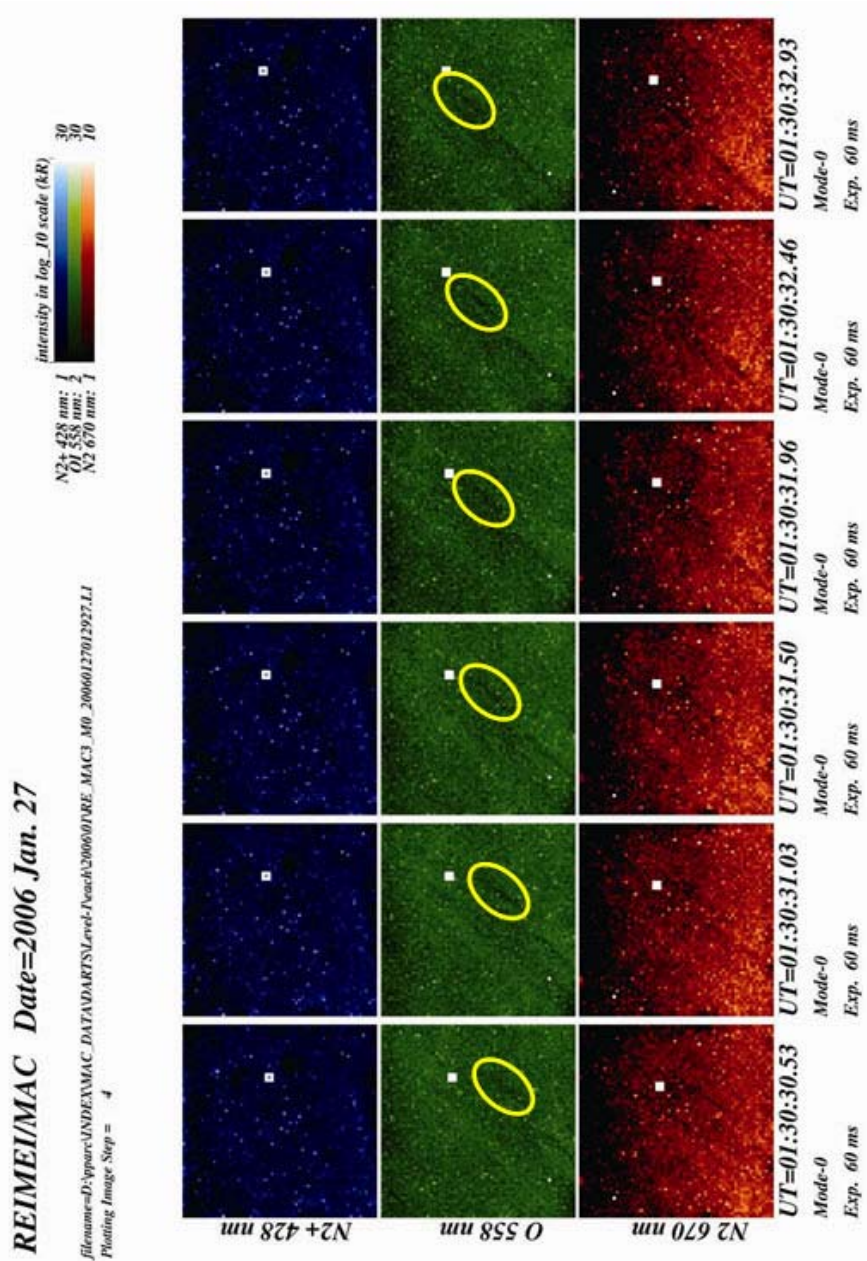


Figure 5.10 Image data of drifting black patch event. The event was observed on January 27, 2006. Format of the figure is same to Figure 5.2. A magnetic footprint of the satellite passed over a black patch (yellow circle) at around 01:30:31.9 UT. Apparent direction of drifting black patch is left-upward in images (westward, see Figure 5.12).



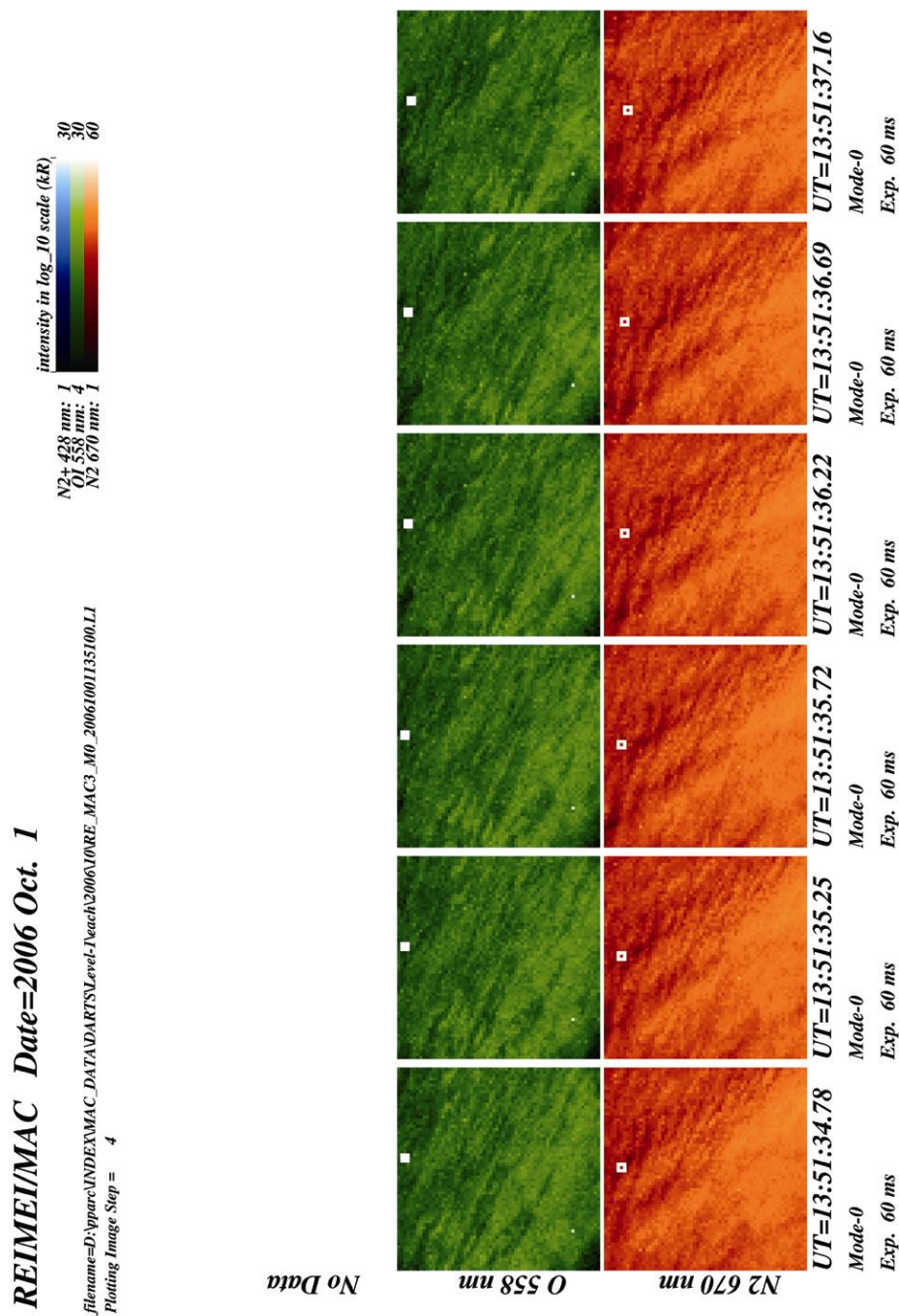
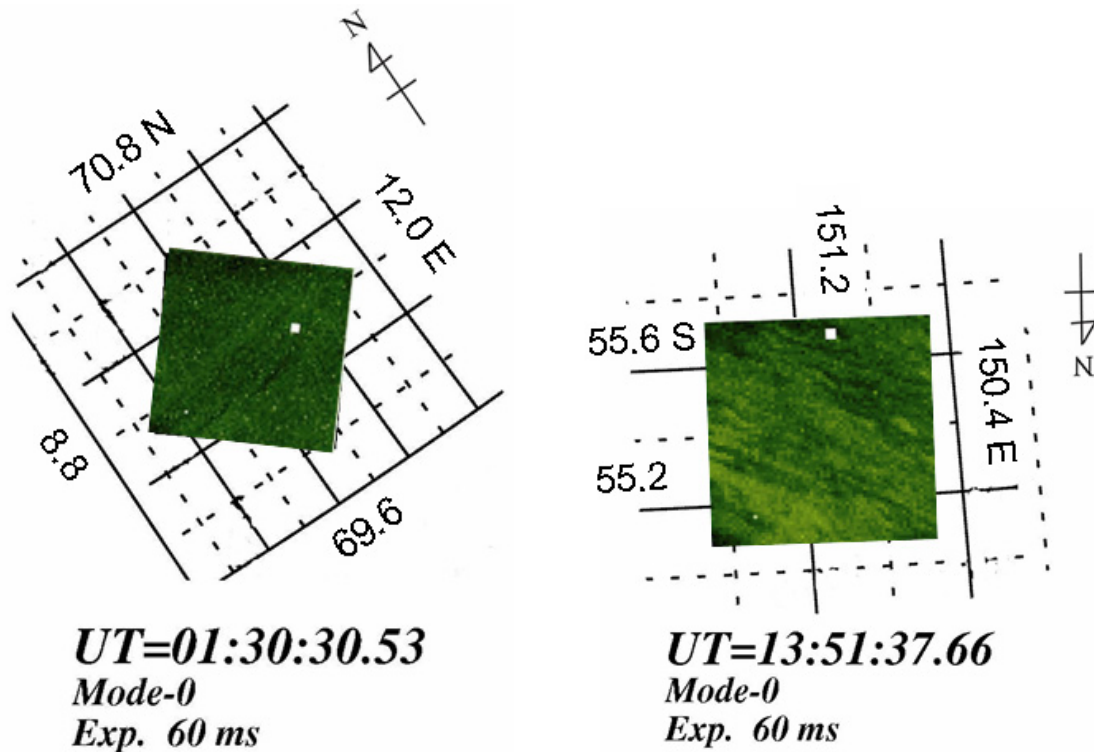


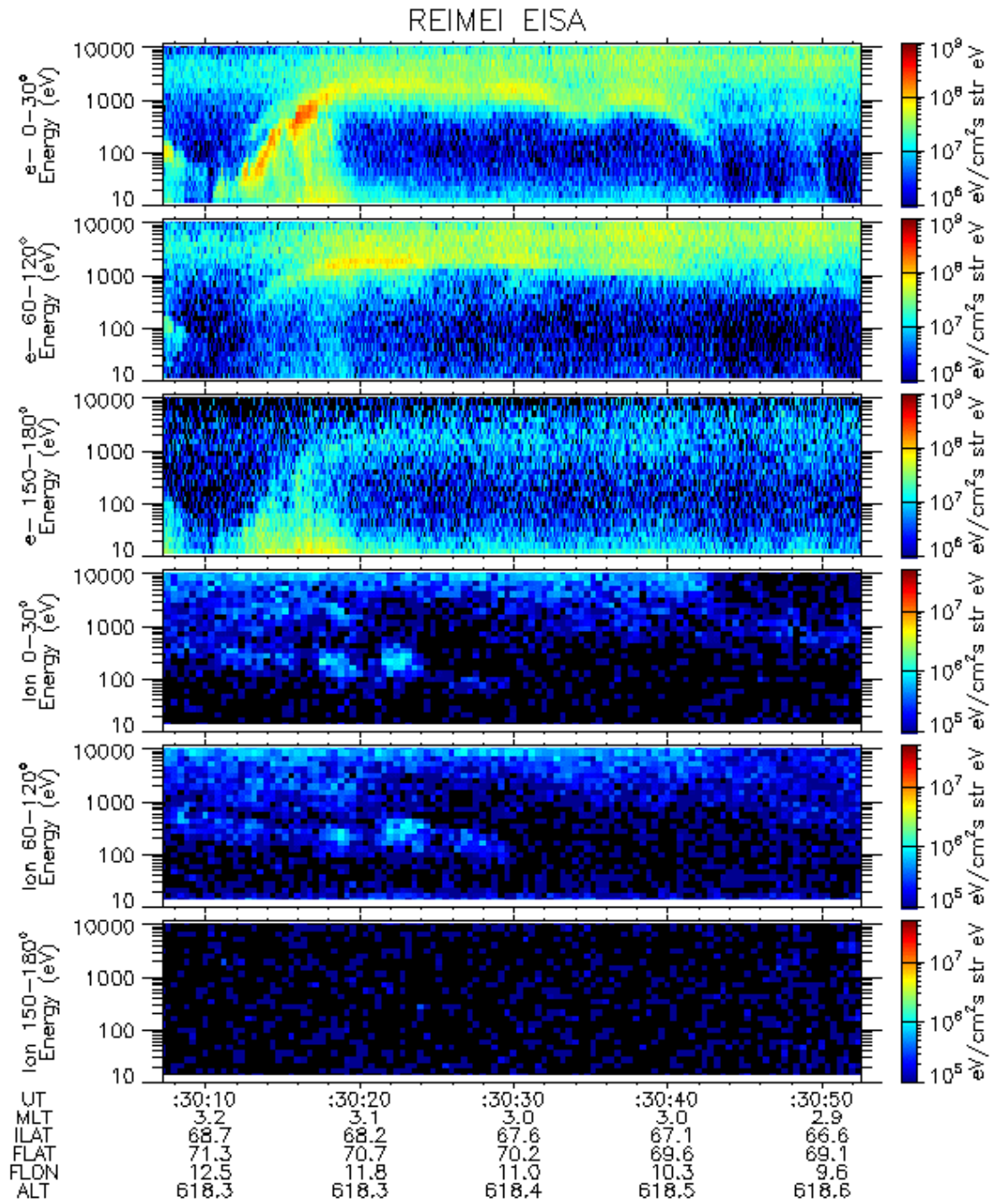
Figure 5.11 Image data of drifting black patch event on October 1, 2006. A magnetic footprint of the satellite passed over a black patch at around 13:51:37 UT. Black patches in the upper half of images are drifting from bottom right to top left (nearly eastward, see Figure 5.12), and those in the lower half of images are drifting from top left to bottom right (nearly westward, see Figure 5.12) in successive images.



**Figure 5.12** Image data mapped on the geographic coordinate. The left image is for the event on January 27, 2006, and the right one is for the event on October 1, 2006. A direction from top right to bottom left in the left image corresponds to westward, and a direction from bottom right to top left in the right image corresponds to nearly eastward direction.

Next, E-T diagrams for these events of drifting black patches are shown in **Figure 5.13** (for the event on January 27, 2006) and **Figure 5.14** (for the event of October 1, 2006). Format of these figures is same to that of **Figure 5.4**. In the top panel of **Figure 5.13**, which is an E-T diagram for precipitating electrons, inverted-V structures with peak energies less than 2 keV are seen between 01:30:10 UT and 01:30:44 UT. A magnetic footprint passed over a black patch at around 01:30:31.96 UT, and the inverted-V structures overlap the precipitations of higher energies corresponding to surrounding diffuse aurora. **Figure 5.15** shows E-T diagram focused

on the time of the black patch event. In the topmost panel, it is seen that precipitation flux with energies greater than 5 keV is deficient at the time of black patch event (01:30:31.9 UT), in a similar way to other black arc and black patch events. Electron differential number fluxes for this black patch event and surrounding diffuse aurora are shown in **Figure 5.17**. Similar to other black arc and black patch events, the flux with the energies greater than 5 keV decreases rapidly, and that with energies less than 5 keV shows no change from that surrounding diffuse aurora. Again, it is also suggested that deficiency of the electron flux for black patch in higher energies is not caused by potential structure such as the divergent electric field. In third panel from the top in **Figure 5.14**, which shows an E-T diagram for precipitating electrons, inverted-V structures with peak energies less than 4 keV are seen between 13:51:24 UT and 13:51:54 UT. A magnetic footprint of the satellite passed over a black patch at around 13:51:36.9 UT, and the inverted-V structures overlap with precipitations corresponding to surrounding diffuse aurora. **Figure 5.16** shows E-T diagrams focused on the time of black patch event. In third panel from the top, which shows an E-T diagram for precipitating electrons, it is seen that precipitation flux with the energies greater than 4 keV is deficient at the time when a magnetic footprint of the satellite passed over a black patch (13:51:36.9 UT), similar to other black arc and black patch events. Electron differential number fluxes for this black patch event and surrounding diffuse aurora are almost similar to the event on January 27, 2006 (see **Figure 5.17**).

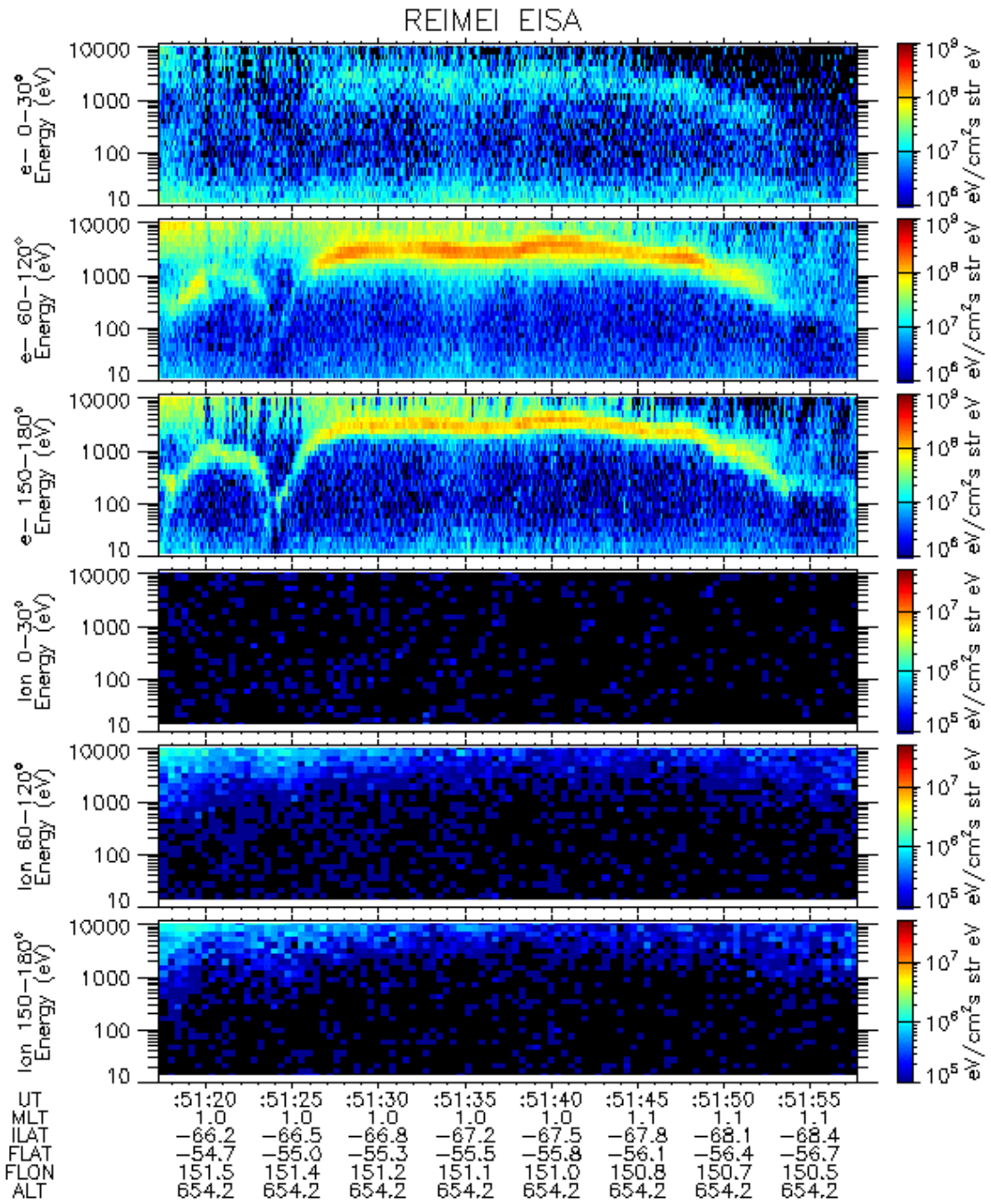


UT from JAN 27,2006 1:30:07 UT

Acc. window=1 for ESA and 10 for ISA

Wed Dec 12 16:18:13 2007

**Figure 5.13** E-T diagrams observed on January 27, 2006. Top panel shows that for precipitating electrons. In this panel, inverted-V structures with peak energy less than 2 keV are seen.



UT from OCT 1, 2006 13:51:17 UT

Acc. window=1 for ESA and 10 for ISA

Mon May 07 17:46:37 2007

**Figure 5.14** E-T diagrams observed on October 1, 2006. Third panel from the top shows that for precipitating electrons. In this panel, inverted-V structures with three peaks with energies less than 4 keV are seen.



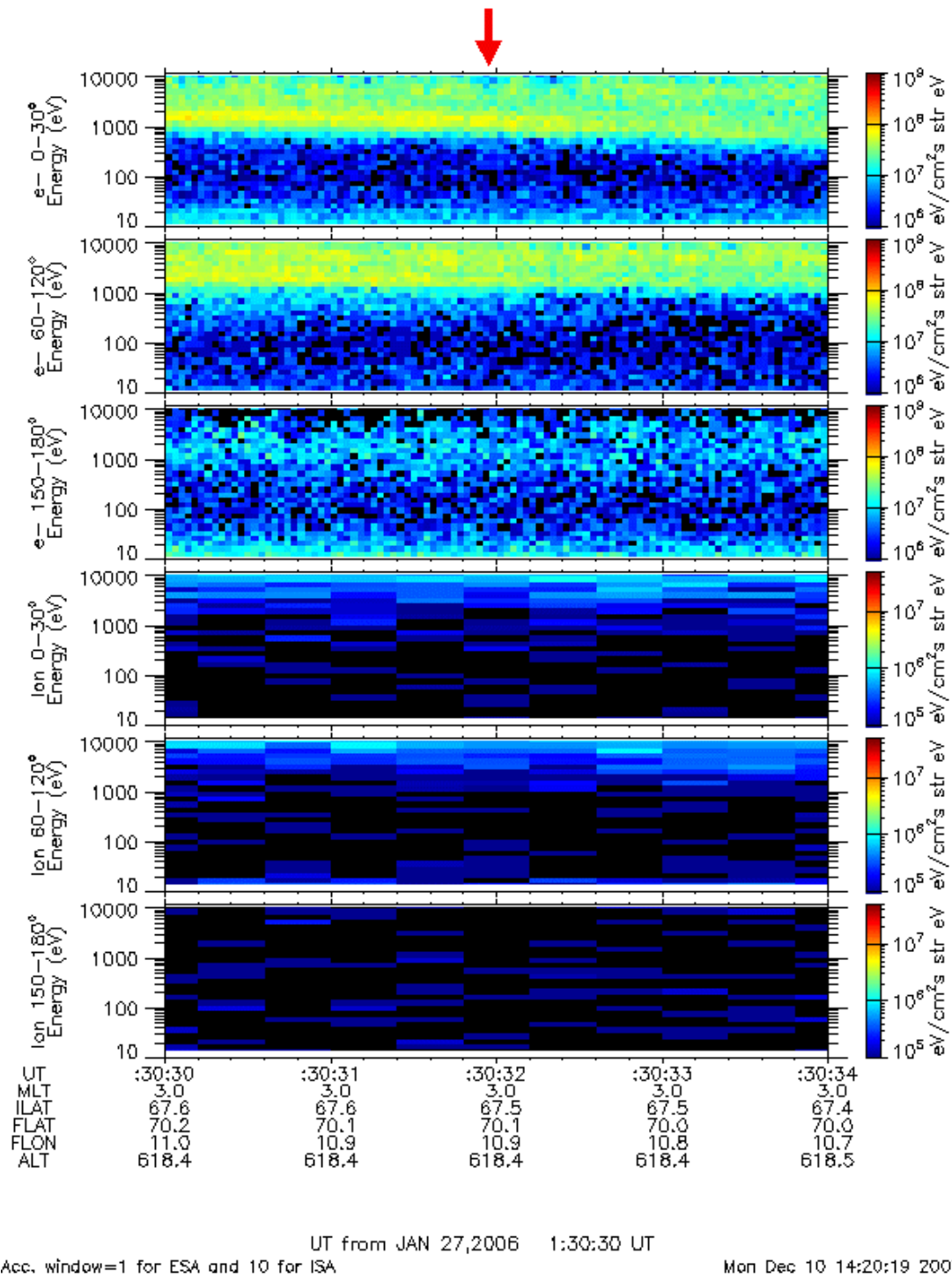
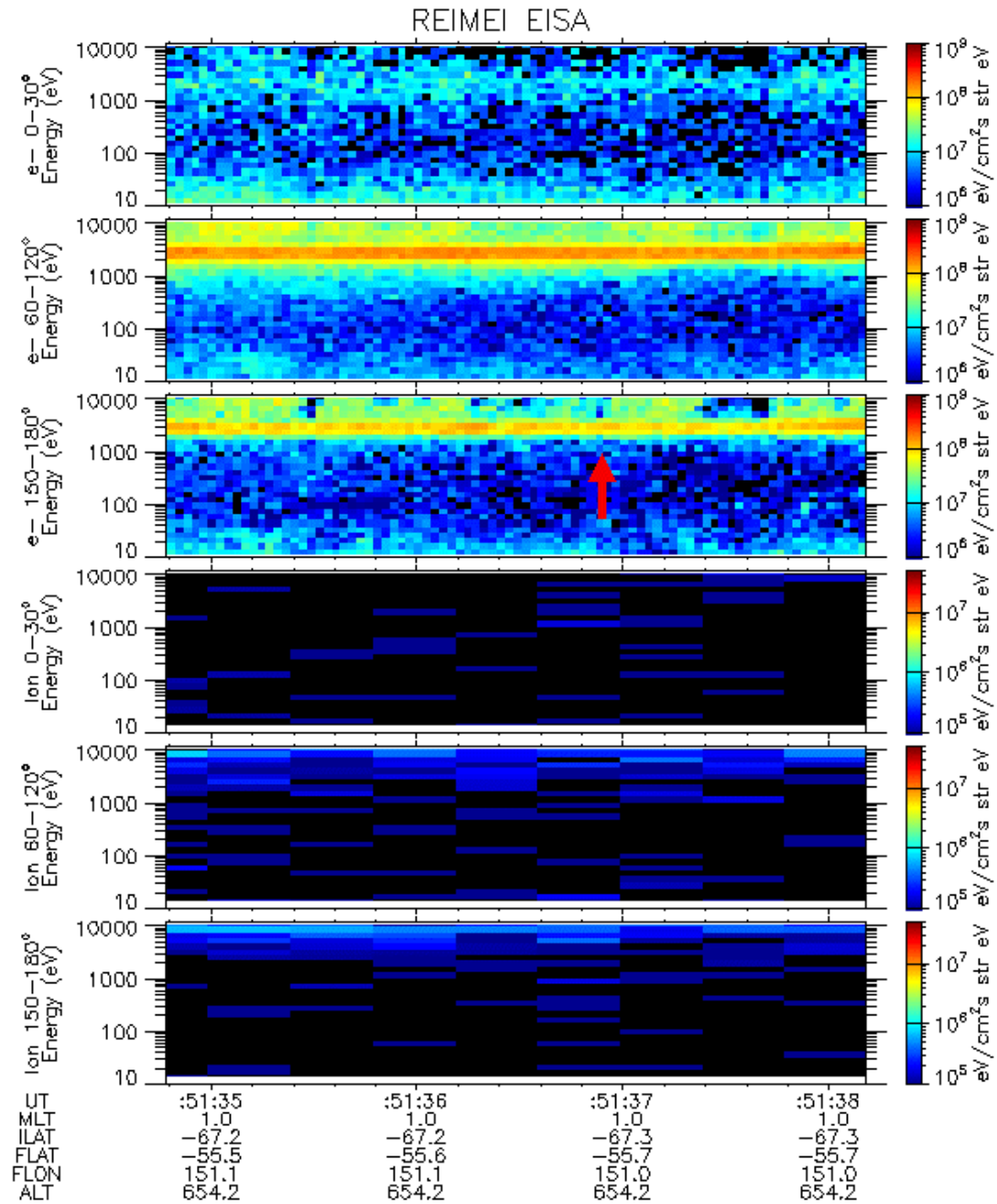


**Figure 5.15** E-T diagrams focused on a period when drifting black patch was seen on January 27, 2006. At around 01:30:31.96 UT, a magnetic footprint of the satellite passed over a black patch. It is seen that precipitation flux with energies greater than 6 keV is deficient at that time (top panel, red arrow).



UT from OCT 1, 2006 13:51:34 UT

Acc. window=1 for ESA and 10 for ISA

Mon May 07 17:49:55 2007

**Figure 5.16** E-T diagrams focused on the time of drifting black patch event (October 1, 2006). At around 13:51:37 UT, a magnetic footprint of the satellite passed over a black patch. It is seen that precipitation flux with energies greater than 4 keV is deficient at that time (third panel, red arrow).

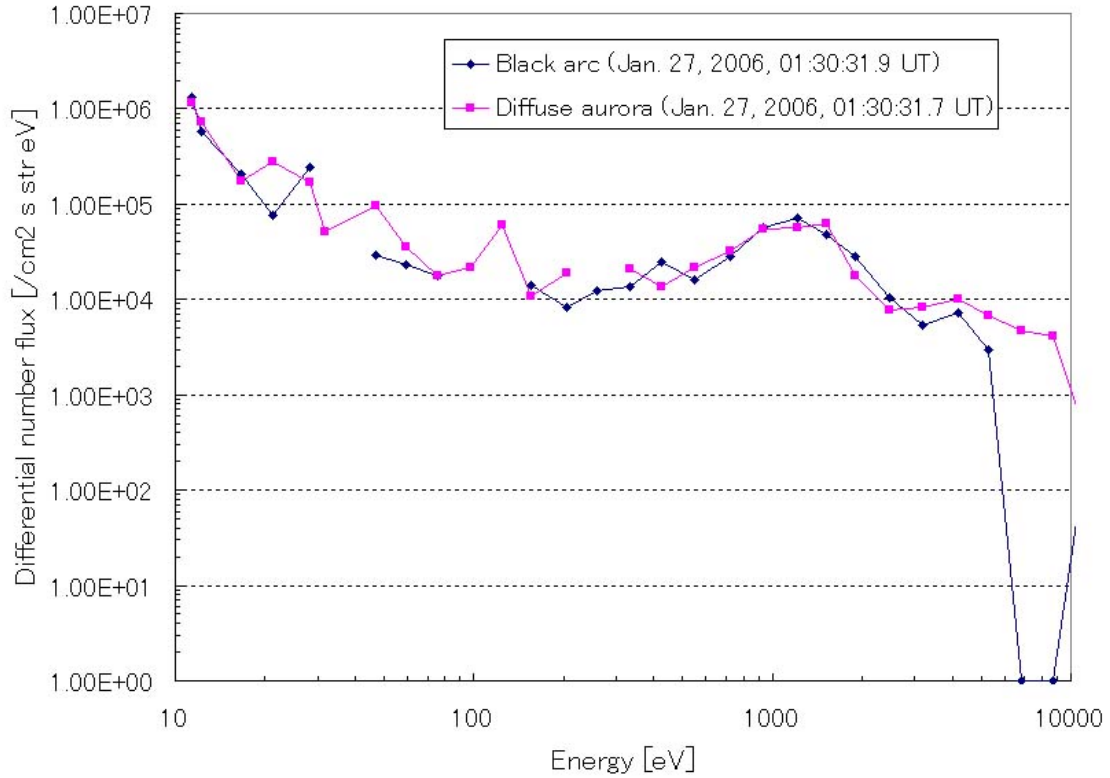


**Figure 5.17** Electron differential number flux versus energy at the time of black patch event and of surrounding diffuse aurora. As in Figure 5.6, differential number flux for surrounding diffuse aurora is also shown. Similar to other black arc and black patch events, differential number flux for the energies greater than 5 keV is clearly deficient, and that for energies less than 5 keV shows no change from that for surrounding diffuse aurora.

### 5.3.2 2D correlation analysis

In order to derive precise drift velocity and direction, two drifting black patch events were analyzed by using 2D correlation analysis, which was described in Chapter 4. The results are shown in **Figure 5.18** and **Figure 5.19**. In **Figure 5.18**, a black patch is seen around the center of the image. White lines indicate the drifting direction of a region denoted by diamond shape, and the length of white lines shows the drifting velocity. In case of drifting black patch event



shown in **Figure 5.18**, the “region of interest” (see Section 4.3) was defined as  $8 \times 8$  pixels considering a spatial scale of the black patch. As a result, direction to which the black patch drifted was just westward, and the drift velocity was about 5.7 km/s. In addition, it is also shown that surrounding diffuse aurora also drifts with similar velocity. In case of drifting black patch event shown in **Figure 5.19**, the “region of interest” was defined as  $6 \times 6$  pixels considering a spatial scale of the black patch. In **Figure 5.19**, black patches in the upper-right half of the image drifted nearly eastward, and those in the bottom-left half of the image drifted nearly westward. Those two groups of black patches drifted in opposite directions each other. The drift speed was from about 3.03 km/sec to about 3.44 km/sec, and the average speed was about 3.3 km/sec. In the past study [Trondsen and Cogger, 1997], drifting black patches were reported to have eastward speed ranging from several hundreds m/s to 2.7 km/s. As stated in the previous section, our results on drifting black patch events obtained by Reimei observation are different from their result.

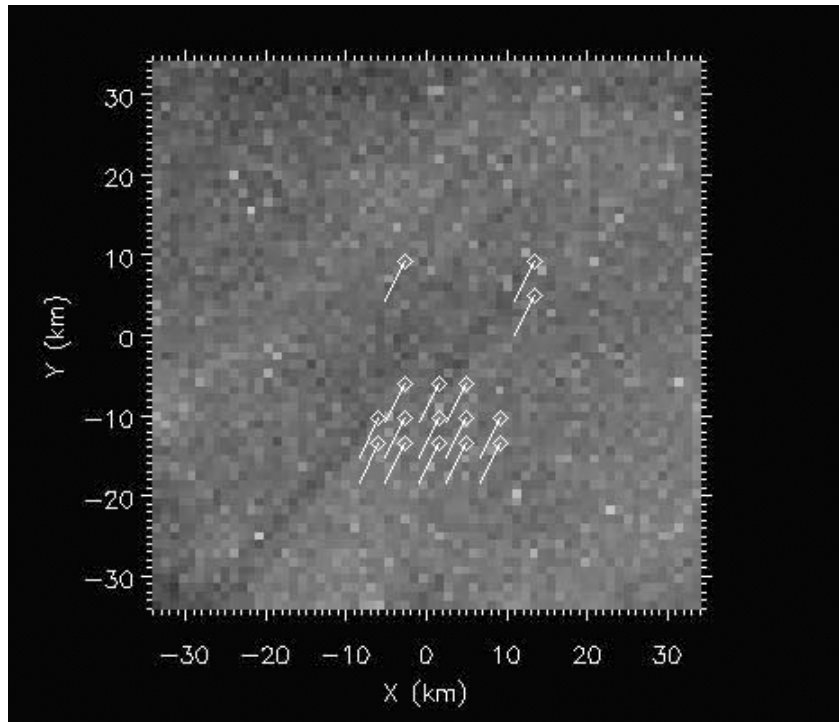


**Figure 5.18** A result of 2D correlation analysis for drifting black patch event on January 27, 2006. White lines indicate the direction and the velocity of a region of diamond shape. In this event, a black patch in the center of image drifted westward with a speed of about 5.7 km/s.

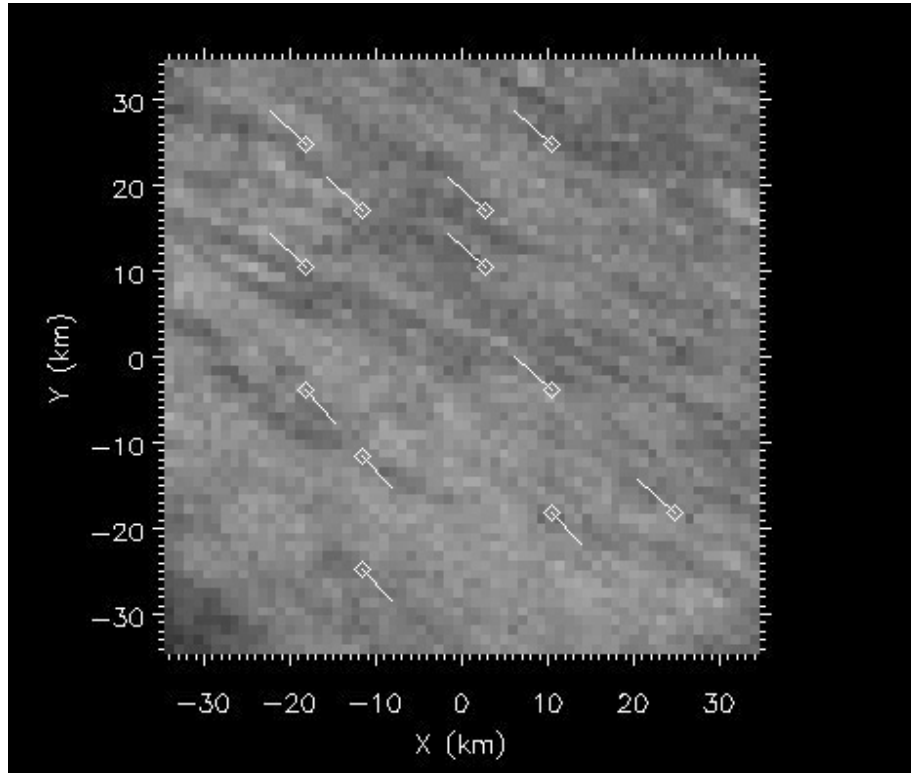


**Figure 5.19** A result of 2D correlation analysis for drifting black patch event on October 1, 2006. White lines indicate the direction and the velocity of a region of diamond shape. In this event, black patches in the upper-right half of the image drifted nearly eastward, and those in the bottom-left half of the image drifted nearly westward. Drift speed ranges from 3.03 to 3.44 km/sec, and the average speed is about 3.3 km/sec.

# Chapter 6

## Discussion

In this chapter, possible mechanism for producing black arc and black patch, and that for the drift of black patches are discussed. In Section 6.1, the possible mechanism for producing black arc and black patch based on the results of analysis for black aurora observation data obtained by Reimei, which were given in Section 5.2, is discussed. In Section 6.2, the possible mechanism for the drift of black patches based on the results of data analysis that was given in Section 5.3 is discussed.

### 6.1 Possible mechanism for producing black arc and black patch

As described in Section 5.2, it was revealed that the flux of precipitating electrons is locally deficient at the time when a magnetic footprint of the satellite passed over black arc or black patch. Particularly, only electrons with energies greater than 2 ~ 7 keV is deficient, and those with energies less than that show no change from electrons producing diffuse aurora that surrounds the black aurora, as shown in **Figure 6.1**.

*Marklund et al.* [1997] reported that a divergent electric field with spatial scale of 1 km was observed by Freja satellite (not necessarily associated with black aurora), and suggested that such electric field is possible to be associated with black aurora structure. However, actual correspondence between such electric field and optical black aurora was not identified because they did not made optical observation. Since this work, it has been believed that such small scale divergent electric field can cause black aurora. However, simultaneous optical imaging observation of black aurora and in-situ observation of precipitating particles, electric field, and wave has never been realized. Since its successful launch, Reimei has been continuing simultaneous image and particle observations for aurora, and we succeeded in simultaneous conjugate observations of black aurora. Therefore, it becomes possible to discuss whether black aurora is produced by such divergent electric field. **Figure 6.2** shows the distribution of

differential number flux versus energy at a time when a magnetic footprint passed over a black patch and surrounding diffuse aurora. The date on which this data was obtained is same as that shown in **Figure 6.1**. As discussed in the preceding Chapter, the flux of precipitating electrons with energies greater than 3 keV for black patch (dark blue points and line) is deficient compared to that for surrounding diffuse aurora (pink points and line). On the other hand, the electron flux with energies less than that for black patch is almost same to that for surrounding diffuse aurora. This fact suggests that the deficiency of electron flux with energies higher than 3 keV is not caused by any electric field such as the divergent electric field. In all black aurora events observed by Reimei, the differential number flux of electrons for black arc and black patch shows similar distribution as shown in **Figure 6.2**. In addition, electron precipitation caused by inverted-V potential structure with peak energy of lower than  $\sim 3$  keV often appears simultaneously and overlaps with electron precipitation that causes diffuse aurora (6 events out of 13 events). It is not plausible that a divergent electric field overlaps with a convergent electric field. In the work by *Marklund et al.* [1997], they show a divergent electric field located in between two convergent electric fields which are likely to carry downward field-aligned currents. Our results strongly suggest that black aurora is not generated by divergent electric field. Therefore, another possible mechanism for producing black aurora has to be considered.

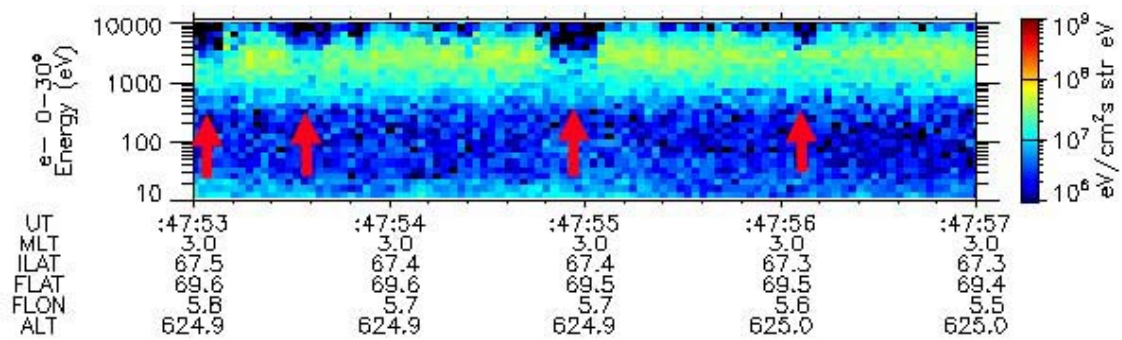


**Figure 6.1** E-T diagram of downward electrons at times when a magnetic footprint of the satellite passed over black patches. The data was obtained on February 2, 2006. Red arrows denote the times of four black patch events.

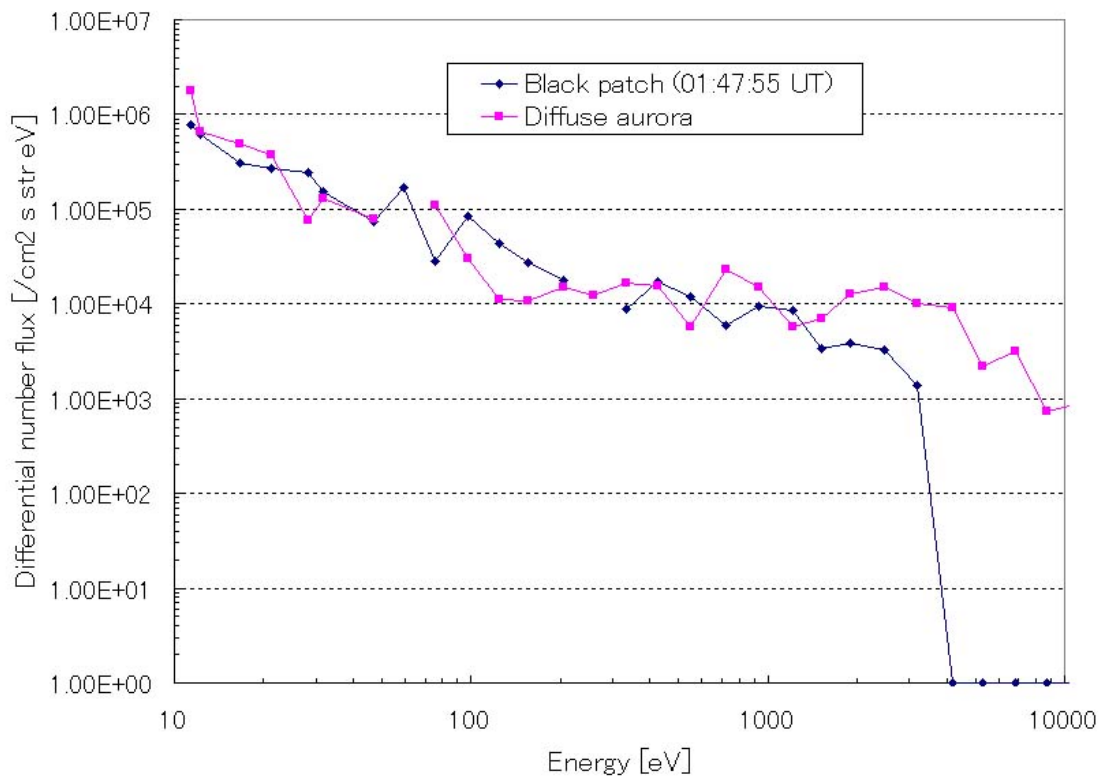


**Figure 6.2** Differential number flux of downward electrons at the time when a magnetic footprint of the satellite passed over a black patch and surrounding diffuse aurora. The date on which this data was obtained is same to that shown in Figure 6.1.

Now, a possible mechanism for black aurora other than divergent electric field is discussed in the following. Strong electrostatic Electron Cyclotron Harmonic (ECH) waves were measured in the plasma sheet and they are able to scatter electrons in a range of energies from a few hundreds eV to a few keV into the loss cone. In-situ observations of such waves and model simulations have been made [e.g. *Kennel et al.*, 1970; *Horne et al.*, 2003]. On the other hand, *Inan et al.* [1992] reported that the upper band (UB) whistler mode waves could scatter electrons in a range of energies between 1 keV and 10 keV into the loss cone based on modeling. In addition, *Villalón and Burke* [1995] suggested that plasma sheet electrons scattered into the loss cone by whistler mode waves would produce diffuse aurora. Based on our observation results, in which electron flux with energies greater than 3 keV is deficient at a region

corresponding to black aurora, while electron flux corresponding to surrounding diffuse aurora with energies below that shows no change, it is strongly suggested that the pitch angle diffusion by UB whistler mode waves is suppressed at a source region of black aurora while diffuse aurora surrounding the black aurora is produced by precipitating electrons that was caused by UB whistler mode waves and/or ECH waves in the plasma sheet. Whistler mode waves are generally thought to resonate with keV electrons if the electron density is sufficiently high [Johnstone *et al.*, 1993]. Accordingly, our results of Reimei observations for black aurora suggest that hot electron (few keV) density is low in the source region of black aurora. *Peticolas et al.* [2002] reported results of quasi-simultaneous image and particle observations for black aurora by using an imager on board an airplane and a particle analyzer on board the FAST satellite. In their observations, black aurora was observed forty seconds before and one minute after the magnetic footprint of the FAST satellite passed the magnetic zenith of the imager. They suggested that pitch angle diffusion for electrons with energies above 2 keV was suppressed in a region connected to the black aurora (see Chapter 1).

In the data of Reimei observations, pulsating aurora often appeared in the equatorward of black arcs and black patches. This fact is consistent with past works [e.g. *Trondsen and Cogger*, 1997]. In addition, source region of pulsating aurora appears to be the central plasma sheet (CPS) [e.g. *Hirahara et al.*, 1997] from spectrum of ions. Therefore, black arcs and black patches are expected to appear equatorward of the boundary plasma sheet (BPS) or poleward of the CPS.

By using data of the CRRES satellite, *Meredith et al.* [2001] reported that UB whistler mode waves are distributed in the region of magnetic equator. Combining our observation results from Reimei and reported observation results in the past as mentioned above, a schematic picture can be made as shown in **Figure 6.3**. Further understanding of generation mechanism for black aurora from the observation data obtained by Reimei would be difficult because Reimei is in a low (~650 km) orbit and instruments for wave and/or plasma density are not equipped. Therefore, in the future, further simultaneous imaging observation, and wave and/or plasma density measurement with high spatial and temporal resolutions in a region shown in **Figure 6.3** will provide more conclusive understanding of generation mechanism for black aurora.

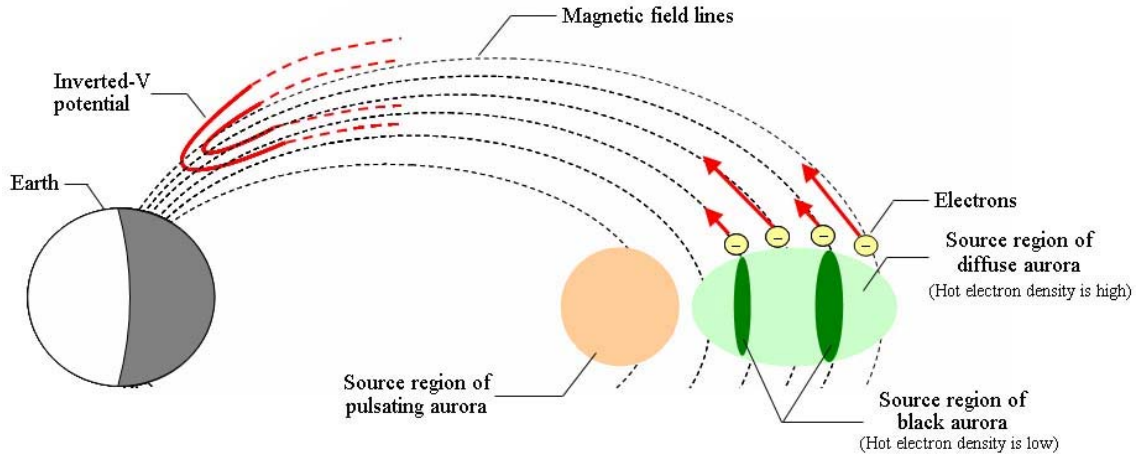


**Figure 6.3** A schematic drawing indicating a region where black aurora is produced. Red arrows denote precipitating electron flux.

## 6.2 Possible mechanism for the origin of drifting black patch

As described in Section 5.3, drifting black patches were observed in midnight sector by Reimei. Drift speeds were determined to be about 5.7 km/sec and 3.3 km/sec, and directions of drift were westward, nearly eastward, and nearly westward. *Trondsen and Cogger [1997]* reported that black patches and black arc segments drifted only eastward with a speed ranging from several hundreds m/sec to 2 km/sec around midnight. The drift speed of black patches derived from Reimei observation is higher than that reported in the previous study, and direction of the drift is also different. Accordingly, drift of black patches observed by Reimei may be a different phenomenon from the one observed in the past.

Now, a mechanism for producing the drift of black patches observed by Reimei should be discussed. **Figure 6.4** shows an E-T diagram of downward electrons observed on January 27, 2006 (westward drifting black patches event). This event is the same to that shown in the preceding Chapter. A magnetic footprint of the satellite passed over a black patch at 01:30:32 UT. Diffuse aurora surrounding the black patch seems to be associated with precipitating

electrons with energies greater than 6 keV. In the energy range below 6 keV, downward electron flux, with an inverted-V potential structure with a peak energy of about 2 keV, overlaps with electron flux associated with diffuse aurora. The peak energy of this inverted-V potential structure is low, therefore, its contribution to aurora emission is expected to be small and any aurora structure is not seen in the image data obtained by MAC. Another E-T diagram of downward electrons observed on October 1, 2006 (drifting black patches event) is shown in **Figure 6.5**. As in **Figure 6.4**, inverted-V potential structure is also seen in this event. Black patches in this event drifted with two opposite directions, nearly eastward and nearly westward (see Section 5.3). At 13:51:37 UT (black arrow), a magnetic footprint of the satellite passed over a black patch drifting nearly eastward. Though a magnetic footprint did not pass over a black patch drifting nearly westward, it is possible to estimate a time at which a magnetic footprint would pass over the black patch by considering the velocity of the satellite and the distance between black patches drifting nearly eastward. A red dotted arrow in **Figure 6.5** denotes such estimated time when a magnetic footprint of the satellite passed over a black patch drifting nearly westward. Because of the concurrent inverted-V potential structure,  $E \times B$  force is expected to drift precipitating electrons in a region where these black patches were observed. In the event on January 27, 2006 (**Figure 6.4**), direction of  $E \times B$  drift is westward by considering the direction of electric field due to the inverted-V potential structure and magnetic field (in the northern hemisphere). At a time indicated by the black arrow in **Figure 6.4**, the westward drifting black patch is located in south of a peak location of the inverted-V potential structure. Expected direction of  $E \times B$  drift is consistent with direction of the drift of the black patch. In the event observed in the southern hemisphere on October 1, 2006 (**Figure 6.5**), the directions of  $E \times B$  drift, which is expected to both eastward and westward, is also consistent with directions of oppositely drifting black patches. A schematic drawing for configuration of an inverted-V potential structure,  $E \times B$  drift, and drifting black patches is shown in **Figure 6.6**. The drawing corresponds to the event on October 1, 2006 (shown in **Figure 6.5**).



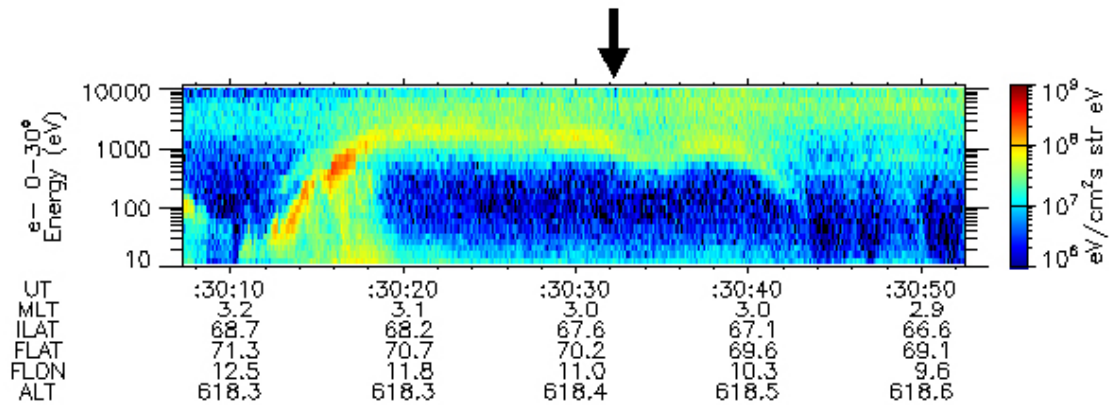


Figure 6.4 E-T diagram of downward electrons observed between 01:30:07 UT and 01:30:52 UT on January 27, 2006. A magnetic footprint passed over a black patch at 01:30:32 UT (black arrow).

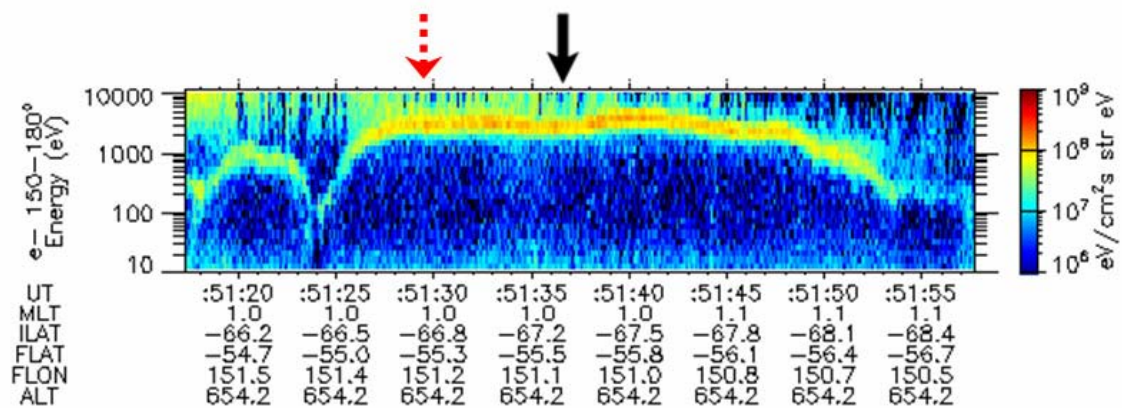
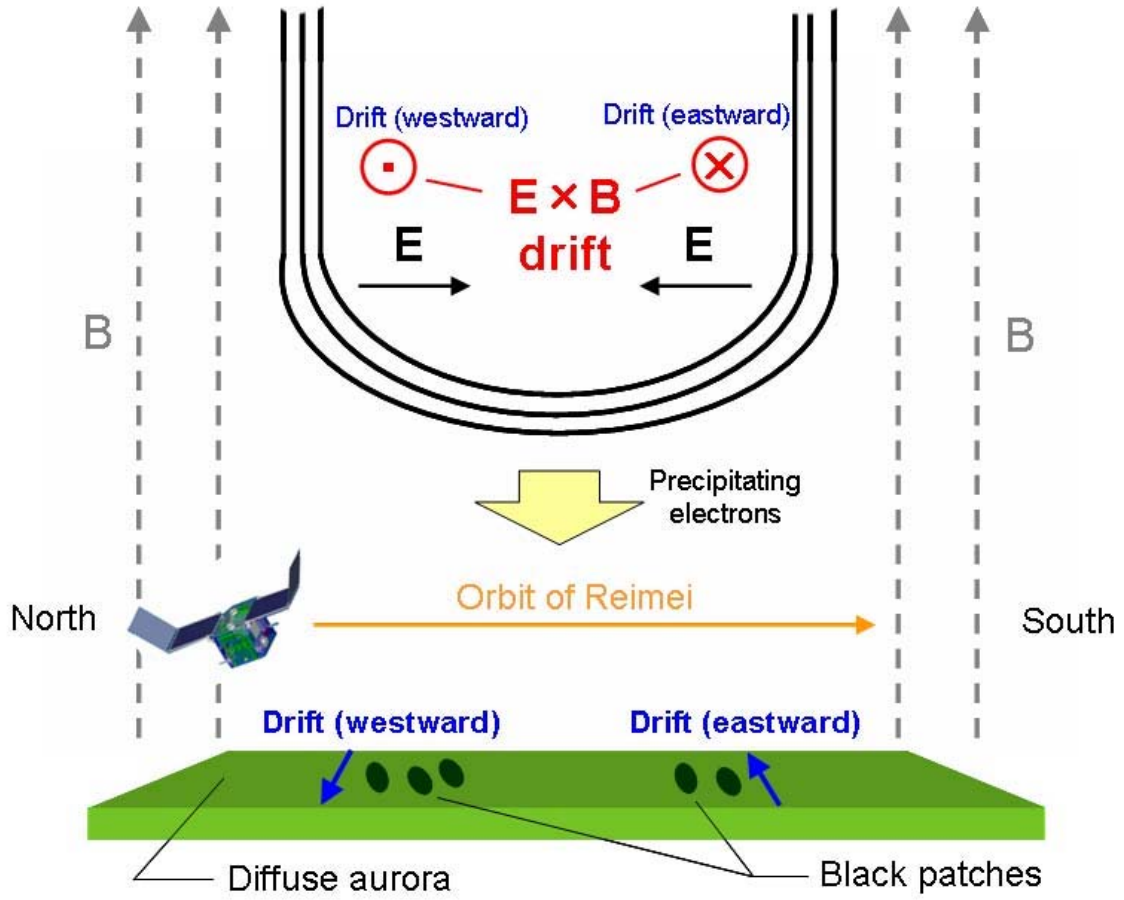


Figure 6.5 E-T diagram of downward electrons observed between 13:51:17 UT and 13:51:58 UT on October 1, 2006. A magnetic footprint passed over a black patch, which was drifting nearly eastward, at 13:51:32 UT (black arrow). A red dotted arrow denotes an estimated time at which a magnetic footprint of the satellite would pass over a black patch drifting nearly westward (At that time, the magnetic footprint was out of FOV of MAC).



**Figure 6.6** A schematic drawing for configuration of inverted-V structure,  $E \times B$  drift and oppositely drifting black patches. Reimei passed from north to south.

As stated in Section 5.3, drifting speed for these two events of drifting black patches were derived using 2D correlation analysis. The drift speed of a black patch on January 27, 2006 was about 5.7 km/sec, and that of on October 1, 2006 was about 3.3 km/sec, which is an average for all black patches in that event. If the drift is caused by  $E \times B$  drift originating from inverted-V potential structure with low peak energy, the electric field can be calculated from the drift speed. Electric field causing  $E \times B$  drift is calculated by following equations;

$$\frac{v_1}{v_0} = \sqrt{\frac{B_0}{B_1}} \quad (6.1)$$

$$v_1 = \frac{\vec{E}_\perp \times \vec{B}_1}{B_1^2} = \frac{E_\perp}{B_1} \quad (6.2)$$

where  $v_0$  is a velocity of black patch drift at 110 km altitude,  $v_1$  is a velocity of the electron drift in a region where pitch angle diffusion by waves occurs (the source region of electron precipitation for diffuse aurora and black patches),  $B_0$  is a magnetic flux density at 110 km altitude,  $B_1$  is a magnetic flux density at the source region, and  $E_\perp$  is the electric field that causes  $E \times B$  drift. In the present study, the region where pitch angle diffusion takes place is assumed to be the magnetic equator referring the past studies [e.g., Meredith *et al.*, 2001]. Here, we assume that the inverted-V structure is extended even to the magnetic equator. Equation (6.1) is derived from the law of conservation of magnetic moment, and equation (6.2) is obtained from the equation of charged particle motion. In case of the event on January 27, 2006,  $v_0$  is 5.7 km/sec,  $B_0$  is 50716.4 nT, and  $B_1$  is 170.5 nT. These values give an electric field,  $E_\perp$ , of 16.64 mV/m. In case of the event on October 1, 2006,  $v_0$  is 3.3 km/sec,  $B_0$  is 62180.7 nT, and  $B_1$  is 222.8 nT. These values give an electric field,  $E_\perp$ , of 12.28 mV/m. In this way, by analyzing particle data obtained by Reimei, the electric field could actually be derived. Now, we can compare these electric fields to those calculated from the peak energy and the spatial scale of inverted-V potential structures seen in the two events. In case of the event on January 27, 2006, the peak energy of the inverted-V potential structure is about 1.5 keV, and the spatial scale of this inverted-V potential structure is estimated to be 144 km by taking velocity of the satellite, about 8 km/sec, into account. Electric field,  $E_\perp$ , is calculated to be about 20.8 mV/m. In case of the event on October 1, 2006, the peak energy of the inverted-V potential structure is about 3.2 keV, and the spatial scale of this inverted-V potential structure is estimated to be 112 km. Electric field,  $E_\perp$ , calculated from these values becomes to be about 57.1 mV/m. As a result of above estimations, electric field derived from a drift velocity of black patch using 2D correlation analysis gives close agreement with electric field calculated from Reimei particle data for the event on January 27, 2006. For case of the event on October 1, 2006, electric field derived from drift velocity of black patch does not agree with electric field calculated from Reimei particle data so well as the event on January 27, 2006. However, the order of electric field calculated from drift velocity agrees with the order of electric field calculated from Reimei

particle data.

Based on above discussion, it is proved that black patch drift at auroral altitude is caused by  $E \times B$  drift taking place in the magnetic equatorial region.

## Chapter 7

# Conclusions

In the present thesis, Multi-spectral Auroral Camera (MAC), to be on board the Reimei satellite, has been developed in order to investigate fine-scale auroral structures which include black auroras. After successful insertion into a polar orbit, Reimei provided us with a lot of valuable data of simultaneous observation of both optical imaging and precipitating particles of aurora. Data of black aurora were analyzed, and the possible mechanism for generation of black aurora was identified by using results of the data analysis. Further, the drift motion of black patches could be explained based on Reimei observation.

Firstly, conclusions on development of Reimei satellite and MAC are given below. Reimei is the first of a series of Japanese scientific small satellite project of JAXA/ISAS. Reimei is a three-axis stabilized satellite and its size and weight are 724 mm × 626 mm × 609 mm and about 70 kg, respectively. Reimei was launched from Baikonur Space Center in Kazakhstan as a piggyback satellite into a sun-synchronous polar orbit with an inclination of 98.6 degree at an altitude of approximately 630 km on August 23, 2005 in order to investigate fine-scale auroral structures by using MAC and a top-hat type electron and ion energy spectrum analyzer (ESA/ISA) that has been developed at JAXA/ISAS. MAC is a three-channel monochromatic CCD imager, and its specifications are summarized below; (i) the optical system consists of refracting optics; (ii) the three wavelengths of MAC was chosen so that it can observe  $N_2^+$  1NG (427.8 nm), O green line (557.7 nm), and  $N_2$  1PG (670 nm); (iii) field-of-view of MAC is 7.6 degrees; (iv) spatial and temporal resolutions are about 1.2 km, 120 msec, respectively, in typical observation mode pointing its field of view to a magnetic footprint. During the development stage of MAC, a variety of special measures were necessary to achieve satisfactory operation of MAC. Such special measures in MAC development are summarized below.

- (1) A thermal path that was composed of a bundle of 20 stacked graphite sheets (0.1mm thickness for each sheet), an oxygen-free copper block and aluminum parts were fabricated for reducing CCD thermal noise. Also, a thermal path for cooling some elements, which would reach to a temperature higher than guaranteed temperature of each component in space environment, on CCD boards and power control board, was developed. Due to these measures, it was confirmed that each CCD was sufficiently cooled (down to lower than 0 degrees Celsius), and dark noise on CCD image could be reduced satisfactory (about 3 counts) for observation of weak auroral emission, and temperature of elements on CCD board and power control unit was maintained lower than the guaranteed temperature at least for 11 minutes duration in the thermal vacuum test.
- (2) From the analysis of spot diagrams of optics, it was found that the focus of MAC had to be adjusted with an accuracy better than 10  $\mu\text{m}$  in order that MAC would be able to observe aurora with spatial resolution of 1.2 km. For adjustment of focus, a system with a collimator using a refracting telescope has been developed. By using this system, the focus was successfully adjusted with an accuracy better than 10  $\mu\text{m}$ .
- (3) In order to check if MAC is durable enough for vibration and shock in launch condition, vibration and shock tests for MAC were carried out. As a result of these tests, it was confirmed that MAC has sufficient durability against launch environments. In addition, by using a system that was used for the adjustment of focus, it was checked whether there was any change in the optical system of MAC by vibration and shock. A small amount of CCD displacement relative to the lens was resulted due to vibration and shock test. However, the displacement was within 10  $\mu\text{m}$  for all three channels of MAC and it was negligible. Further, radiation effect on CCDs and interference filters of MAC was checked by applying proton beam of 100 MeV. Result of the test showed that MAC is sufficiently tolerate for radiation expected for Reimei's nominal lifetime of three months.
- (4) Sensitivity calibration of MAC using an integrating sphere has been carried out at National Institute of Polar Research. The sensitivity calibration showed that MAC has sufficient sensitivity, and noise equivalent intensity of aurora was estimated to be about 200 R.

Secondary, conclusions on characteristics and possible generation mechanism of black aurora based on Reimei observation are given below. Since its successful launch, Reimei has been carrying out observation of fine scale structures of aurora. Optical observations of black arc and black patch were successfully made with MAC for 23 events in a period from November 1st, 2005 through October 30th, 2006. Among them, simultaneous optical imaging and precipitation particle observations were made for 13 events, of which nine events are black arc events, and other four events are black patch events. Nineteen events out of all 23 events were observed in the northern hemisphere, and the others were observed in the southern hemisphere. Based on the analysis of these black aurora events, characteristics and possible generation mechanism of black aurora are summarized as follows.

- (1) Emission intensities of black arc and black patch are rather faint in the order of  $2 \sim 4$  kR. The intensities are not different between the northern hemisphere and the southern hemisphere. The width of black arc is in a range of  $3 \sim 10$  km. The scale of black patch is about  $3 \sim 5$  km. The width is not different between the northern and the southern hemisphere, too.
- (2) Black arc and black patch appear favorably in the invariant latitude range of  $66 - 68$  degrees. On the other hand, black arc and black patch appear also in the invariant latitudes greater than  $70$  degrees. This fact has not been reported in past studies. This may be because coverage area of our observation is quite large compared to the past observations.
- (3) Regarding a relation between magnetic activity and the appearance of black arc and black patch, 11 events out of 19 events (the northern hemisphere events) were observed in magnetic quiet periods. Other events were observed in a variety of conditions.
- (4) Behaviors of precipitating electrons and ions that correspond to all black arc or black patch events obtained by Reimei showed that their characteristics are those coming from the central plasma sheet. Precipitating electron flux with energies greater than  $2 \sim 7$  keV is deficient at the time when a magnetic footprint of the satellite passed over a black arc or black patch.

- (5) An inverted-V structure with a peak energy of 2 ~ 5 keV associated with black aurora is often seen in the downward electron E-T diagram. Such inverted-V structures overlap electron precipitations contributing to diffuse aurora. Six events out of 13 black arc or black patch events are associated with such inverted-V structures. Because of their weak peak energy, precipitations accelerated by inverted-V structure do not seem to contribute strongly to aurora emissions in the image data obtained by MAC.
- (6) Pulsating aurora was often associated with black arc and black patch, and it appears in the equatorward of black aurora. In pulsating aurora, apparent energy-dispersions are seen in precipitating electron flux. On the other hand, electron flux for black arc does not show any energy-dispersion.
- (7) Precipitating electron flux with energies greater than 2 ~ 7 keV for black arc and black patch is deficient compared to that for surrounding diffuse aurora. On the other hand, the electron flux with energies less than that for black patch is almost same to that for surrounding diffuse aurora. This fact suggests that the decay of electron flux with energies greater than 2 ~ 7 keV is not caused by any electric field such as the divergent electric field. Based on our observation results described above, it is strongly suggested that the pitch angle diffusion by upper band whistler mode waves is suppressed at a source region of black aurora while diffuse aurora surrounding the black aurora is produced by precipitating electrons that was caused by pitch angle scattering due to upper band whistler mode waves and/or electrostatic Electron Cyclotron Harmonic waves in the plasma sheet. Accordingly, our results of Reimei observations for black aurora suggest that hot electron (few keV) density is low in the source region of black aurora.
- (8) Drifting speed for two events of drifting black patches were derived using 2D correlation analysis. The drift speed of a black patch on January 27, 2006 was about 5.7 km/sec, and that on October 1, 2006 was about 3.3 km/sec. Because of existence of concurrent inverted-V structure,  $E \times B$  force is expected for drifting electrons in a source region where these black patches were produced. Electric fields, which cause such  $E \times B$  drift, were estimated from drift speeds derived by using 2D correlation analysis of image data. Estimated electric field is in close agreement with an electric field calculated from inverted-V structure for the event on January 27, 2006. For the case of the event on October



1, 2006, electric field estimated from drift velocity of black patch does not agree so well with an electric field calculated from inverted-V structure as the event on January 27, 2006. However, the order of the electric field calculated from drift velocity agrees with the order of an electric field calculated from Reimei particle data.

As stated above, a variety of characteristics of black aurora, which has not been reported in past works, were obtained by Reimei observation. However, further understanding of generation mechanism for black aurora from the observation data obtained by Reimei would be difficult because Reimei is in a low (~650 km) orbit and instruments for wave and/or plasma density are not equipped. Therefore, in the future, further simultaneous imaging observation of black aurora with high spatial and temporal resolutions, and wave and/or plasma density measurement in its source region, which is expected to be the magnetic equator, will provide more conclusive understanding of generation mechanism for black aurora.



# References

- Akasofu, S.-I., and J. R. Kan, Dayside and nightside auroral arc system, *Geophys. Res. Lett.*, *10*, 753, 1980.
- Asamura, K., D. Tsujita, H. Tanaka, Y. Saito, T. Mukai, and M. Hirahara, Auroral particle instrument onboard the INDEX satellite, *Adv. Space Res.*, *32*, 375, 2003.
- Banks, P. M., C. R. Chappel, and A. F. Nagy, A new model for the interaction of auroral electrons with the atmosphere: Spectral degradation, backscatter, optical emission, and ionization, *J. Geophys. Res.*, *79*, 1459, 1974.
- Beach, R., G. R. Cresswell, T. N. Davis, T. J. Hallinan, and L. R. Sweet, Flickering, A 10-cps fluctuation within bright auroras, *Planet. Space Sci.*, *16*, 1525, 1968.
- Belmont, G., D. Fontaine, and P. Canu, Are electron cyclotron waves responsible for diffuse auroral electron precipitation?, *J. Geophys. Res.*, *88*, 9163, 1983.
- Blixt, E. M., and M. J. Kosch, Coordinated optical and EISCAT observations of black aurora, *Geophys. Res. Lett.*, *31*, 06813, doi:10.1029/2003GL019244, 2004.
- Borovsky, J. E., Auroral Arc Thicknesses as Predicted by Various Theories, *J. Geophys. Res.*, *98*, 6101, 1993.
- Borovsky, J. E., and D. M. Suszcynsky, Optical measurements of the fine structure of auroral arcs, in *Auroral Plasma Dynamics*, Geophys. Monog. 80, edited by R. Lysak, p. 25, American Geophysical Union, Washington, DC, 1993.
- Carlson, C. W., R. F. Pfaff, and J. G. Watzin, The fast auroral snapshot (FAST) mission, *Geophys. Res. Lett.*, *25*, 2013, 1998.
- Cattell, C., S3-3 Satellite instrumentation and data, in *The IMS Source Book*, edited by C. Russell and D. Southwood, p. 91, American Geophysical Union, Washington, DC, 1982.
- Chen, M. W., and M. Schulz, Simulations of stormtime diffuse aurora with plasma sheet electrons in strong pitch angle diffusion, *J. Geophys. Res.*, *106*, 28949, 2001.

- Davidson, G. T., Pitch angle diffusion and the origin of temporal and spatial structures in pulsating aurorae, *Space Sci. Rev.*, 53, 45, 1990.
- Davis, T. N., Observed characteristics of auroral forms, *Space Sci. Rev.*, 22, 77, 1978.
- Davis, T. N., Observed microstructure of auroral forms, *J. Geomagn. Geoelectr.*, 30, 371, 1978.
- Demekhov, A. G., and V. Y. Trakhtengerts, A mechanism of formation of pulsating aurora, *J. Geophys. Res.*, 99, 5831, 1994.
- Frey, H. U., G. Haerendel, J. H. Clemmons, M. H. Boehm, J. Vogt, O. H. Bauer, D. D. Wallis, L. Blomberg, and H. Lühr, Freja and ground-based analysis of inverted-V events, *J. Geophys. Res.*, 103, 4303, 1998.
- Gerdjikova, M. G., and G. G. Shepherd, Evaluation of auroral 5577-A excitation processes using Intercosmos Bulgaria 1300 satellite measurements, *J. Geophys. Res.*, 92, 3367, 1987.
- Gough, M. P., P. J. Christiansen, G. Martelli, and E. J. Gershuny, Interaction of electrostatic waves with warm electrons at the geomagnetic equator, *Nature*, 279, 515, 1979.
- Hallinan, T. J., and T. N. Davis, Small-scale auroral arc distortions, *Planet. Space Sci.*, 18, 1735, 1970.
- Hallinan, T. J., J. Kimball, H. C. Stenbaek-Nielsen, K. Lynch, R. Arnoldy, J. Bonnell, and P. Kintner, Relation between optical emissions, particles, electric fields, and Alfvén waves in a multiple rayed arc, *J. Geophys. Res.*, 106, 15445, 2001.
- Hirahara, M., A. Yamazaki, K. Seki, T. Mukai, E. Sagawa, N. Kaya, and H. Hayakawa, Characteristics of downward flowing ion energy dispersions observed in the low-altitude central plasma sheet by Akebono and DMSP, *J. Geophys. Res.*, 102, 4821, 1997.
- Hoffman, R. A., and E. R. Schmerling, Dynamic Explorer program: An overview, *Space Sci. Instrum.*, 5, 345, 1981.
- Horne, R. B., P. J. Christiansen, and M. P. Gough, Weak electrostatic waves near the upper hybrid frequency: A comparison between theory and experiment, *J. Geophys. Res.*, 92, 3243, 1987.
- Horne, R. B., and R. M. Thorne, Electron pitch angle diffusion by electrostatic electron harmonic waves: The origin of pancake distributions, *J. Geophys. Res.*, 105, 5391, 2000.
- Horne, R. B., R. M. Thorne, N. P. Meredith, and R. R. Anderson, Diffuse auroral electron scattering by electron cyclotron harmonic and whistler mode waves during an isolated substorm, *J. Geophys. Res.*, 108, 1290, doi:10.1029/2002JA009736, 2003.

- Inan, U. S., Y. T. Chiu, and G. T. Davidson, Whistler-mode chorus and morningside aurorae, *Geophys. Res. Lett.*, *19*, 653, 1992.
- Johnson, C. Y., “Ionosphere composition and density from 90 to 1200 kilometers at solar minimum”, *J. Geophys. Res.*, *71*, 330, 1966.
- Johnstone, A. D., The mechanism of pulsating aurora, *Ann. Geophys.*, *1*, 397, 1983.
- Johnstone, A. D., D. M. Walton, R. Liu, and D. A. Hardy, Pitch Angle Diffusion of Low-Energy Electrons by Whistler Mode Waves, *J. Geophys. Res.*, *98*, 5959, 1993.
- Kamide, Y., and S.-I. Akasofu, The location of the field-aligned currents with respect to discrete auroral arcs, *J. Geophys. Res.*, *81*, 3999, 1976.
- Kennel, C. F., F. L. Scarf, R. W. Fredricks, J. H. Mcghee, and F. V. Coroniti, VLF electric field observations in the inner magnetosphere, *J. Geophys. Res.*, *75*, 6136, 1970.
- Kimball, J., and T. J. Hallinan, Observations of black auroral patches and of their relationship to other types of aurora, *J. Geophys. Res.*, *103*, 14671, 1998a.
- Kimball, J., and T. J. Hallinan, A morphological study of black vortex streets, *J. Geophys. Res.*, *103*, 14683, 1998b.
- Kunitake, M., and T. Oguti, Spatial-temporal characteristics of flickering spots in flickering auroras, *J. Geomagn. Geoelectr.*, *36*, 121, 1984.
- Lundin, R., G. Haerendel, and S. Grahn, The Freja project, *Geophys. Res. Lett.*, *21*, 1823, 1994.
- Lundin, R., and G. Haerendel, Micro and meso scale measurements by the Freja satellite, in *Space Plasmas: Coupling Between Small and Medium Scale Processes*, Geophys. Monog. 86, edited by Ashour-Abdalla, M. et al., p. 295, American Geophysical Union, Washington, DC, 1995.
- Lyons, L. R., Electron diffusion driven by magnetospheric electrostatic waves, *J. Geophys. Res.*, *79*, 575, 1974.
- Maggs, J. E., and T. N. Davis, Measurements of the thicknesses of auroral structures, *Planet. Space Sci.*, *16*, 205, 1968.
- Marklund, G., L. Blomberg, C. G. Falthammar, and P. A. Lindqvist, On intense diverging electric fields associated with black aurora, *Geophys. Res. Lett.*, *21*, 1859, 1994.
- Marklund, G., T. Karlsson, and J. Clemmons, On low-altitude particle acceleration and intense electric fields and their relationship to black aurora, *J. Geophys. Res.*, *102*, 17509, 1997.

- McFadden, J. P., C. W. Carlson, M. H. Boehm, and T. J. Hallinan, Field-aligned electron flux oscillations that produce flickering aurora, *J. Geophys. Res.*, **92**, 11133, 1987.
- McFadden, J. P., C. W. Carlson, and M. H. Boehm, Structure of an energetic narrow discrete arc, *J. Geophys. Res.*, **95**, 6533, 1990.
- McFadden, J. P., C. W. Carlson, and R. E. Ergun, Microstructure of the auroral acceleration region as observed by FAST, *J. Geophys. Res.*, **104**, 14453, 1999.
- Meredith, N. P., R. B. Horne, A. D. Johnstone, and R. R. Anderson, The temporal evolution of electron distributions and associated wave activity following substorm injections in the inner magnetosphere, *J. Geophys. Res.*, **105**, 12907, 2000.
- Meredith, N. P., R. B. Horne, and R. R. Anderson, Substorm dependence of chorus amplitudes: Implications for the acceleration of electrons to relativistic energies, *J. Geophys. Res.*, **106**, 13, 165, 2001.
- Mozer, F. S., C. A. Cattell, M. A. Temerin, R. B. Torbert, S. von Glinski, M. Woldorff, and J. Wygant, The dc and ac electric field, plasma density, plasma temperature, and field-aligned current experiments on the S3-3 satellite, *J. Geophys. Res.*, **84**, 5875, 1979.
- Nakamura, R., and T. Oguti, Drifts of auroral structures and magnetospheric electric fields, *J. Geophys. Res.*, **92**, 11241, 1987.
- Oguti, T., Metamorphoses of aurora, *Mem. Natl. Inst. Polar Res. Spec. Issue Jpn.*, **12**, 101, 1975.
- Oguti, T., Observations of rapid auroral fluctuations, *J. Geomag. Geoelectr.*, **30**, 299, 1978.
- Oya, H., and K. Tsuruda, Introduction to the Akebono (EXOS-D) satellite observations, *J. Geomag. Geoelectr.*, **42**, 367, 1990.
- Peticolas, L. M., T. J. Hallinan, H. C. Stenbaek-Nielsen, J. W. Bonnell, and C. W. Carlson, A study of black aurora from aircraft-based optical observations and plasma measurements on FAST, *J. Geophys. Res.*, **107**, 1217, 2002.
- Richmond, A., "Thermospheric dynamics and electrodynamics", in *Solar Terrestrial Physics*, edited by R. L. Caravilano and J. M. Forves, p. 523, D. Reidel, The Netherlands, 1983.
- Royrvik, O., Pulsating aurora: Local and global morphology, Ph.D. thesis, Univ. of Alaska, Fairbanks, 1976.

- Saito, H., T. Mizuno, K. Tanaka, Y. Sone, S. Fukuda, S. Sakai, N. Okuizumi, M. Mita, Y. Fukushima, M. Hirahara, K. Asamura, T. Sakanoi, A. Miura, T. Ikenaga, and Y. Masumoto, AN-OVERVIEW AND INITIAL IN-ORBIT STATUS OF "INDEX" SATELLITE, *56th International Astronautical Conference*, IAC-05-B5.6.B.05, 2005.
- Sakanoui, K., and H. Fukunishi, Temporal and spatial structures of flickering aurora derived from high-speed imaging photometer observations at Syowa Station in the Antarctic, *J. Geophys. Res.*, *109*, 1221, doi:10.1029/2003JA010081, 2004.
- Sakanoui, K., H. Fukunishi, and Y. Kasahara, A possible generation mechanism of temporal and spatial structures of flickering aurora, *J. Geophys. Res.*, *110*, 3206, doi:10.1029/2004JA010549, 2005.
- Sakanoui, T., H. Fukunishi, and T. Mukai, Relationship between field-aligned currents and inverted-V parallel potential drops observed at midaltitudes, *J. Geophys. Res.*, *100*, 19343, doi:10.1029/95JA01285, 1995.
- Sakanoui, T., S. Okano, Y. Obuchi, T. Kobayashi, M. Ejiri, K. Asamura, and M. Hirahara, Development of the multi-spectral auroral camera onboard the INDEX satellite, *Adv. Space Res.* *32*, 379, 2003.
- Sandahl, L., L. Eliasson, and R. Lundin, Rocket observations of precipitating electrons over a pulsating aurora, *Geophys. Res. Lett.*, *7*, 309, 1980.
- Sato, N., D. M. Wright, C. W. Carlson, Y. Ebihara, M. Sato, T. Saemundsson, S. E. Milan, and M. Lester, Generation region of pulsating aurora obtained simultaneously by the FAST satellite and a Syowa-Iceland conjugate pair of observatories, *J. Geophys. Res.*, *109*, 10201, doi:10.1029/2004JA010419, 2004.
- Schrifer, D., M. Ashour-Abdalla, R. J. Strangeway, R. L. Richard, C. Kletzing, Y. Dotan, and J. Wygant, FAST/Polar conjunction study of field-aligned auroral acceleration and corresponding magnetotail drivers, *J. Geophys. Res.*, *108*, COA 21-1 8020, doi:10.1029/2002JA009426, 2003.
- Stasiewicz, K., P. Bellan, C. Chaston, C. Kletzing, R. Lysak, J. Maggs, O. Pokhotelov, C. Seyler, P. Shukla, L. Stenflo, A. Streltsov, and J.-E. Wahlund, Small scale Alfvénic structure in the aurora, *Space Science Rev.*, *92*, 423, 2000.
- Stenbaek-Nielsen, H. C., T. J. Hallinan, D. L. Osborne, J. Kimball, C. Chaston, J. McFadden, G. Delory, M. Temerin, and C. W. Carlson, Aircraft observations conjugate to FAST: Auroral arc thicknesses, *Geophys. Res. Lett.*, *25*, 2073, 1998.

- Temerin, M., What we really know about auroral acceleration?, *Adv. Space Res.*, 20, 1025, 1997.
- Torr, M. R., D. G. Torr, and P. G. Richards, The N<sub>2</sub><sup>+</sup> first negative system in the dayglow from Spacelab 1, *J. Geophys. Res.*, 197, 17075, 1992.
- Trondsen, T. S., and L. L. Cogger, High-resolution television observations of black aurora, *J. Geophys. Res.*, 102, 363, 1997.
- Trondsen, T. S., L. L. Cogger, and J. C. Samson, Asymmetric multiple auroral arcs and inertial Alfvén waves, *Geophys. Res. Lett.*, 24, 2945, 1997.
- Trondsen, T. S., and L. L. Cogger, A survey of small-scale spatially periodic distortions of auroral forms, *J. Geophys. Res.*, 103, 9405, 1998.
- Villalón, E., and W. J. Burke, Pitch angle scattering of diffuse auroral electrons by whistler mode waves, *J. Geophys. Res.*, 100, 19361, 1995.
- Vogt, J., H. U. Frey, G. Haerendel, H. Höfner, and J. L. Semeter, Shear velocity profiles associated with auroral curls, *J. Geophys. Res.*, 104, 17277, 1999.
- Wagner, J. S., R. D. Sydora, T. Tajima, T. Hallinan, L. C. Lee, and S.-I. Akasofu, Small-scale auroral arc deformations, *J. Geophys. Res.*, 88, 8013, 1983.
- Wrenn, G. L., J. F. E. Johnson, and J. J. Sojka, Stable “pancake” distributions of flow energy electrons in the plasma trough, *Nature*, 279, 512, 1979.